

**Magnetometry with Microwave-Assisted Optical Pumping in Warm Rb
Vapor
and Microfabricated Rb Vapor Cells**

by

Ying-Ying Lu

A thesis submitted in partial fulfillment of the requirements for the degree of

Master of Science

Department of Physics
University of Alberta

© Ying-Ying Lu, 2021

Abstract

Quantum optical sensing is a maturing field that offers the capability to achieve extraordinary sensitivity. Atomic magnetometers, for example, now have the capability to detect brain signals and to precisely measure Earth’s gravity field. In optical atomic magnetometers, the electronic spins of the atoms in vapor form are aligned in the same direction by “pumping” the ensemble using laser light at a select frequency. Any magnetic field alters the spin states, which changes the optical properties of the vapor, such as the transmission of the laser light, providing a way to measure magnetic fields.

After reviewing the theory of atomic structure and atom-light interactions relevant to the research presented here, I describe in the first part of this thesis a vector magnetometry method using microwave-assisted optical pumping, in which a microwave field resonant to the ground state hyperfine splitting of ^{87}Rb pumps an ensemble of warm rubidium vapor, in addition to a strong optical pump beam, and a weaker optical probe beam. I present theoretical details as well as preliminary data demonstrating magnetic field measurements of a DC magnetic field. The measurements were taken when the DC field was aligned at various angles relative to the microwave magnetic field alignment. I compare theoretical and experimental differences in the measurements.

With new methods for quantum devices comes the need for portability. In the second part of this thesis, we demonstrate the fabrication of millimeter-sized rubidium vapor cells using silicon micro-machining techniques. This method is relatively inexpensive compared to glass-blowing methods and allows rapid, large-scale produc-

tion. I describe our process flow and demonstrate the presence of rubidium atoms inside our vapor cells. To conclude, suggestions for improvement are discussed.

Preface

The vector magnetometry idea and the terminology “microwave-assisted optical pumping” was proposed by Andrei Tretiakov. The data were taken together by both Andrei and myself. The exact theoretical equations presented here were researched by myself, with input from Andrei. The optical setup was borrowed from the Hybrid Quantum Systems experiment that was built by Taras Hrushevskiy and Michelle Sullivan. Taras assisted us with laser troubleshooting. This project was a part of several other microwave-related experiments. Here, only the magnetometry experiment is presented, but aspects of the other experiments will be included in our manuscript [in preparation], “*Engineering atomic polarization with microwave-assisted optical pumping*” by A. Tretiakov, Y. Y. Lu, C. Potts, J. Davis, and L. J. Leblanc.

The vapor cell fabrication design and process flow were researched by myself and modified in consultation with the nanoFAB staff here at the University of Alberta, to accommodate our purposes and their equipment capabilities. The fabrication was done by myself, except the silicon nitride deposition, which was done as a fee-for-service at the nanoFAB. The optical setup and activation of the rubidium dispensers were done by myself, with input from my supervisor Lindsay Leblanc, and with help from Benjamin Smith and Logan Cooke, who showed me how to set up the Faraday isolator and how to operate the 1064 laser. The rubidium absorption measurements were done with assistance from Andrei Tretiakov.

Acknowledgements

First of all, I would like to thank my supervisor Lindsay Leblanc for providing me with the opportunity to work in her lab. Thank you for your guidance and for being responsive to all of my concerns and inquiries, whether or not they be research-related. :)

And everyone else in the group, thank you: Logan Cooke for inviting me to help out in the lab, Anindya Rastogi for answering all my questions, Erhan Saglamyurek for his enthusiasm, Benjamin Smith for your insights, and Michelle Sullivan (who has since graduated) for being there to talk to in and outside the lab. Special thanks to Taras Hrushevsky for teaching me about optics and for being readily available to debug our optics setup and Andrei Tretiakov for letting me join him in his research and for sharing his knowledge. Thank you also to the members of the Davis Lab and to all my other friends in the department (there are too many of you to name) for their friendliness.

When I first started, I did not have travel plans. For that reason, I am grateful to Arina Tashchilina for inviting me on my first hiking trip to the Rockies. I'd like to give a big shout-out to her, Andrei, Taras, and his family for letting me join them on their outdoor excursions. I enjoyed learning how to rock climb, how to scramble up a mountain (I won't forget Big Sister!), cross-country skiing, biking on terrain and camping in a tent for the first time in my life. Additionally, I'd like to thank Tian Ooi for her cheeriness, for always being helpful, for cutting my hair, and for our baking hangouts. Our trip to Slave Lake with Arina and Sally was fun! Thank you all for making my time in Alberta more than memorable.

I want to also thank Patrick O'Brien for being the first friend I made here in Edmonton (when we had our recruitment visit back in March 2019). I hope we keep in touch and good luck with your next research endeavor. :)

To Mathilda Tian: thank you for being such a good friend. When I first came to Edmonton, you made me feel more than welcome, even though we did not know each other. All the best to you and Zach!

To the friends I made back home, Shahira Afrin, Ellen Chen, Shannon Chau, Matthew Garayt, Symphony Huang, Eric Ling, Jessie Lu, Joseph Lucero, Elizabeth Pieters, Rachel Van, and many others, thank you for not making me feel homesick, and for always making time for catching up!

And to my previous supervisors, Teresa Cheung and David Sivak, thank you for your guidance, words of encouragement. My experience in your labs has helped me enormously.

Second to last, to my "roommate": thank you for making me laugh every day. You are the best.

Lastly, I want to say, all of this might not have been possible without the encouragement of my parents. Thank you for supporting me all along the way.

Table of Contents

List of Figures	xi
1 Introduction	1
2 Atomic Physics	6
2.1 Alkali Atoms	6
2.2 Atomic and Interaction Hamiltonian	7
2.3 Energy States	8
2.3.1 Orbital Angular Momentum	8
2.3.2 Time Dependence	11
2.3.3 Spin Angular Momentum	12
2.3.4 Quantum Defect	13
2.3.5 Fine Structure and Total Electronic Angular Momentum . . .	13
2.3.6 Russell-Saunders Notation	14
2.3.7 Hyperfine Structure and Total Angular Momentum	15
2.4 Zeeman Effect and the Hyperfine Structure	16
2.5 Atom-Laser Interactions	18
2.5.1 Electric-Dipole Transitions	18
2.5.2 Magnetic Dipole Interactions	21
2.5.3 Two Level System	24
2.6 Relaxation	29
2.6.1 Absorption	31

2.6.2	Weak Driving Intensity	31
2.6.3	High Intensity Limit	32
2.7	Optical Pumping	34
3	Magnetometry with MAOP	39
3.1	Alkali Vapor Magnetometers	39
3.1.1	General Magnetometry	40
3.1.2	Zero-Field Magnetometers	42
3.2	Experimental Setup	43
3.2.1	Microwave Cavity	44
3.2.2	Microwave Source	45
3.2.3	Rubidium Dispensing System	45
3.2.4	Helmholtz Coils	46
3.2.5	Optical Setup	46
3.3	Microwave-Optical Double Resonance	47
3.3.1	Three Level Model	50
3.4	Vector Magnetometry	54
3.4.1	Theory	55
3.4.2	Experimental Data	58
4	Microfabricated Vapor Cells	61
4.1	Background	61
4.2	Alkali Atom Source	62
4.3	Architecture	63
4.3.1	Silicon	64
4.3.2	Design	66
4.3.3	Sealing	67
4.4	Process Flow	67
4.4.1	Wafer Cleaning	69

4.4.2	LPCVD Nitride Deposition	69
4.4.3	Resist Spin Coat	70
4.4.4	Direct-Write Laser Lithography	72
4.4.5	Nitride Etch and Resist Strip	73
4.4.6	KOH Wet Etch	75
4.4.7	Electron-Beam Deposition of Thin Films	76
4.4.8	Anodic Bonding	79
4.4.9	Laser Activation	82
4.5	Rubidium Spectroscopy	85
4.5.1	Optical Setup	85
4.5.2	Reflectance	85
4.5.3	Absorption Measurements	86
4.6	Future Directions	90
4.6.1	Optimizing Rb Vapor Release	90
4.6.2	Through-Hole Cells	90
4.6.3	Extending Polarization Lifetimes	90
4.6.4	Cell Lifetime	92
5	Conclusion and Future Prospects	93
	Bibliography	96
	Appendix A: Matrix Representation of State Vectors and Operators	101
A.1	Bra and Ket Vectors	101
A.2	Operator Matrices	102
	Appendix B: Linear Optics	104
B.1	Polarization and Susceptibility	104
B.2	Absorption	106
B.2.1	Absorption Cross Section	107

Appendix C: Broadening Mechanisms	109
C.0.1 Collision Broadening	109
C.0.2 Doppler Broadening	109

List of Figures

2.1	Energy level diagram for the $n = 5$ shell of ^{87}Rb , where the valence electron resides. The S and the P shell are split due to screening effects and other factors. Adapted from [17].	15
2.2	Energy level due to the low field Zeeman effect in the ground state of ^{87}Rb . Adjacent sublevels are shifted by an amount $\Delta E_Z = \hbar\omega_L$. Nine possible magnetic dipole transitions exist at seven different frequencies. The magnitude of the matrix elements of these transitions are labeled. Transitions (<i>iii</i>) and (<i>iv</i>) have a degeneracy of two.	17
2.3	(a) Linearly polarized light does not change the angular momentum along the quantization axis z , driving π -transitions, (b) left circularly polarized light removes angular momentum, driving σ_- transitions, and (c) right circularly polarized light adds angular angular momentum, driving σ_+ transitions. The red arrows indicate the time dependence of the direction of the electric field.	21
2.4	The microwave field \mathbf{B}_μ lies at an angle θ with respect to the static magnetic field \mathbf{B}_{DC} . \mathbf{B}_μ is confined along the axis of a microwave cavity. \mathbf{B}_{DC} defines the quantization axis.	22
2.5	The Bloch vector lies on the Bloch sphere and precesses about the torque vector $\mathbf{\Omega}$, shown here to lie along the x -axis in the case where $\delta = 0$. The blue dots trace out the trajectory of the Bloch vector, which oscillates between the two states $ \psi_a\rangle$ and $ \psi_b\rangle$	28

2.6	Absorption coefficient $\kappa(\omega)$ at high and low light intensities, in units of $N\sigma_o$, for $I_{\text{sat}} = I$. At high intensities, absorption is reduced and the full-width half maximum is broadened, compared to the situation at low intensities.	32
2.7	A three level ground-state system with one excited state that is (a) unpolarized and absent of light interactions, (b) optically pumped by light linearly polarized along z , and (c) optically pumped by light linearly polarized along x . The angular momentum probability surfaces are shown on the right and the light propagates along y . Asymmetry in the AMPS indicates that there is anisotropy in the system.	34

- 3.1 (a) Energy level diagram for optical pumping schematic with linearly polarized light along x [red arrows]. (a) Presence of transverse static magnetic field \mathbf{B}_{DC} causes the atomic polarization of the ensemble to precess about the magnetic field axis, z . (b) When pumping is synchronized with the Larmor frequency ω_L , the anisotropy axes of the atoms pumped at different times are aligned, generating a macroscopic dynamic polarization. Here, we show amplitude-modulated light, the time-dependence of the beam intensity is illustrated by different shading of the double-headed red arrows. The k direction indicated by the dotted black arrow along y indicates the propagation direction of the beam. Adapted from [25]. (c) Anisotropy causes circular birefringence, in which left and right hand circularly polarized light travel at different speeds in the medium. Linearly polarized light is rotated about the precession axis by an amount θ . (d) Balanced polarimetry setup for detecting Faraday rotation. A half-wave plate [HWP] rotates the plane of polarization of the beam at 45° with respect to the polarizing beam splitter [PBS]. Two photodetectors PD1 and PD2 detect the x - and y -components, respectively, of the intensity of the laser field. . . . 41
- 3.2 Experimental setup of the microwave vector magnetometry experiment. Abbreviations: beam blocker [BB], polarizing beam splitter [PBS], 50/50 beamsplitter [50/50], quarter-wave plate [QWP], photodetector [PD]. 43
- 3.3 Schematic of microwave cavity geometry [not to scale]. Right: main cavity body made of polished copper. White indicates the outer surface of the cavity. Left: cavity end cap. A 2-by-2 mm ring on the end cap splits the modes of the cavity. There are two end caps, only one is shown. 44

3.4	<p>(a) Energy level diagram showing our microwave-optical double resonance setup. A strong pump beam [red arrow] connects $F = 2$ to $F' = 2$, while a probe beam [blue arrow] is tuned to the $F = 1 \rightarrow F' = 0$ transition. A microwave field [green arrow] of frequency ω_μ pumps atoms between $1\rangle = F = 1, m_1\rangle$ and $2\rangle = F = 2, m_2\rangle$. (b) In the presence of a static magnetic field, there is hyperfine splitting and adjacent m_F sublevels within the same hyperfine state F are split by an amount proportional to ω_L. When the microwave field frequency is equal to $\omega_o - 3\omega_L$, atoms are pumped out of $m_1 = -1$. The pump removes atoms from $F = 2$ while the probe measures the population in $F = 2$. (c) Three level approximation used in our theoretical model. We ignore the pump by treating the removal of atoms from $F' = 2\rangle$ as a transverse relaxation represented by γ_2.</p>	47
3.5	<p>MAOP spectra in the presence of (a) Earth's magnetic field, which causes Zeeman splitting of the hyperfine levels, and (b) zero field. The fields were zeroed by applying magnetic fields in the direction opposite to the ambient field using Helmholtz coils. The amplitudes have been normalized such that the maximum amplitude is 1. The data shown are from one of the photodetectors.</p>	48
3.6	<p>Double resonance spectra when the microwave field is (a) parallel to \mathbf{B}_{DC} [π-polarization] and (b) when the field is perpendicular to \mathbf{B}_{DC} [equal parts σ_\pm-polarization]. The amplitudes have been normalized such that the maximum amplitude is 1.</p>	50

3.7 (a) Theoretical [blue triangles] and experimental [red circles] plot of $A_{\pi}^{(iv)}/A_{\sigma_{\pm}}^{(v)}$ [Eq. 3.26] as a function the angle θ between \mathbf{B}_{DC} and \mathbf{B}_{μ} . For the theoretical plot, $\Omega_{\text{P}} = 10^6$ Hz, $\Omega_{\mu} = 0.5 \times 10^3$ Hz, $\gamma_1 = \gamma_2 = 10$ Hz, $\Gamma^* = 10^9$ Hz. The values of γ_i were selected to try to match the maximum relative amplitudes of the theoretical and experimental data. (b) DR spectrum as a function of microwave detuning and increasing axial field strength when we apply a bias field of 0.2 G along the vertical direction. 55

3.8 The infinite possible directions of \mathbf{B}_{DC} lie on a cone with aperture 2θ . 56

3.9 Calibrating the axial coils. (a) σ_+ transitions are detuned by $+\omega_{\text{L}}$ while (b) the right right π transitions are detuned by $2\omega_{\text{L}}$. MAOP spectra as a function of microwave detuning and increasing current in the axial coils due to a magnetic field applied in the (b) vertical and (e) axial direction. Labeled on the last curves are the corresponding frequency shift ω_{L} and $2\omega_{\text{L}}$, which are measured from the first peak on the right to the center peak as shown by the dotted lines. The frequency shift (c) ω_{L} are plotted as a function of applied vertical current and (f) $2\omega_{\text{L}}$ as a function of applied axial current, both fitted to a linear function to obtain the calibration factor m 57

4.1 Vapor cell with reflecting sidewalls schematic; (a) 3D view and (b) side view cut out. 64

4.2 (a) Miller indices for the [100], [110], and [111] directions, and the corresponding (100), (110), (111) planes, which are perpendicular to their respective directions. (b) Diamond structure of silicon. Each atom has four adjacent neighbours. 65

4.3	(a) Conventions for silicon wafer flat orientations. (b) 100 n-type wafer showing the {100} plane and [100] direction. The primary flat gives the [110] direction. (c) Schematic of anisotropically etched features on a $\langle 100 \rangle$ wafer with a square mask.	66
4.4	Vapor cell [red line] and shadow mask (purple line) pattern. The numbers beside each cell indicates the width of the interrogation chamber on the vapor cell wafer.	67
4.5	Process flow showing the 3D and side views of the wafers at each step.	68
4.6	(a) Photoresist exposed to UV light. The mask serves as a photoresist pattern. After exposure (b) for negative-tone photoresist, parts that are not exposed to light are removed during development, (c) while for positive-tone photoresist, parts that are exposed to light are removed during development.	71
4.7	Maskless lithography uses a spatial light modulator. Figure from [44].	73
4.8	Vapor cell after (a) photoresist patterning, exposure, and development, (b) nitride stripping, (c) photoresist stripping, and (d) KOH etching.	74
4.9	KOH etching on a $\langle 100 \rangle$ Si wafer produces sidewalls oriented at 54.7° relative to the surface. (a) KOH etching is highly selective: parts that are not protected by a mask [pink] are etched away. (b) The shadow mask wafer is etched all the way through, while the vapor cell wafer is etched partly through, to a depth of $X \mu\text{m}$. The bottom width of the shadow mask pattern needs to be the same size as the opening of the chamber, so the pattern was designed to be $2\delta = 2 \times 525 \mu\text{m} \times \cot 54.7^\circ$ wider than B	76

4.10	(a) Electron beam deposition schematic. A CTM measures the thickness of the film. (b) The electron beams scan across the crucible which contains the film material. (c) Closed position of the shutter to prevent unwanted deposition. (d) Open position of the shutter. The shinier part of the interrogation chamber is where the Al was deposited, which was not covered by the shadow mask. (e) vapor cell wafer after Al deposition.	78
4.11	(a) The two wafers are fixed by a clamp on the fixture and placed on top of the bottom plate of the bonding system. The top plate is also the lid of the bonder and is the cathode. (b) Result of bonding. The wafer is noticeably cracked where the clamps/spacers were located. . .	79
4.12	Schematic of anodic bonding. (a) The Si wafer [purple] is placed on the bottom of the fixture and the glass wafer [blue] on top. A spacer separates the two wafers. The sandwich is clamped and the fixture is placed on top of the bottom plate. (b) During anodic bonding, the spacer and clamps spring outwards, and a force is applied, pushing down the top plate. A cathode located on the top plate applies a voltage. The bottom plate kept electrically grounded, causing positive ions in the Si wafer to flow upwards towards the boundary and negative ions in the glass to flow downwards. Both plates are kept heated. . .	80
4.13	Anodic bonding steps. The actions in the cell editor are as follows: in step 5 the clamps are removed; in 6, the spacers are removed; in 8, the universal bonding tool is moved down; in 10, two electrodes are set; in 15 the universal bonding tool [a combination of the pressure and the bond head] is moved up.	81
4.14	Imaging and dispenser activation setup. $f_1 = f_2 = f = 150$ mm. . . .	83
4.15	Image of (a) the 1064 laser beam [bright circle] and dispenser [grey circle] and (b) a target with a 0.5 mm diameter hole.	83

4.16	Activated Rb dispenser [bottom left] and inactivated dispenser [top right].	84
4.17	Doppler broadened spectra of rubidium at various cell temperatures [solid lines] give four peaks. The dotted red dotted line shows the reference signal from the EDCL. The transmission amplitudes were shifted in such a way that the maximum amplitudes were equal to the maximum amplitude of the reference signal. Because the reference signal, which was used to trigger the signal on the oscilloscope, shifted along the frequency axis between measurements, and because we show only one reference signal from one temperature measurement, the data points were shifted along the frequency axis so that the dips are located at the proper frequency detunings. All of the data were convoluted with a box of unit magnitude of size 100 to smooth out the digital noise from the oscilloscope. The laser scan was unable to cover the full range of the absorption spectrum of ^{87}Rb	87
4.18	Absorption cross-section for the ^{87}Rb $F = 2$ and the ^{85}Rb $F = 3$ transitions at $T = 315$ K. Dotted colored lines show the individual absorption cross sections for a given transition $ J, F\rangle \rightarrow J', F'\rangle$ [4.9], and the solid black line show the total absorption cross section [Eq. 4.8]. Only two peaks are shown because these transitions will be used to estimate the number density n	89

Chapter 1

Introduction

Quantum mechanics, in contrast to classical physics, takes a probabilistic rather than deterministic view of nature. It is arguably one of the most profound theories ever formulated, exploring phenomena that cannot be explained by classical physics. The non-intuitive nature of quantum mechanics is embodied by the wave-particle duality concept. In quantum mechanics, particles can behave both as a particle and as a wave. Particles such as the electron occupy discrete [quantized] energy levels, which can be described by wave functions. They can also be in a superposition of one or several energy states until measured.

Quantum theory was born in the early 1900s out of research exploring the absorption of light at the subatomic level and other phenomena such as the behavior of heat in solids. The branch of physics concerning the interaction of matter with light at the subatomic scale is encompassed by atomic, molecular, and optical [AMO] physics. Atoms are studied by manipulating their quantum states with radiation such as light.

While quantum computing may be one of the most talked-about revolutionary applications of quantum mechanics, other successful, more readily commercialized quantum technologies include quantum atomic sensors. By definition, quantum sensing refers to one of the following: *(i)* the use of a quantum object that is characterized by discrete energy levels, to measure a classical or quantum quantity, *(ii)* the use of quantum coherence [a spatial or temporal superposition of states] to measure a phys-

ical quantity, or (*iii*) the use of quantum entanglement to improve the sensitivity or precision of a measurement, beyond the classical limit [1]. There has been much effort to replace classical technologies such as communication, where electromagnetic fields are transmitted and received, and magnetometry, where the strengths and/or directions of static magnetic fields are measured, by their quantum counterparts. Since atoms can interact strongly with electric and magnetic fields, these phenomena can be exploited for detecting electromagnetic waves. A subclass of quantum sensors is atomic interferometers, which are used for gravity sensing in geological surveying for detecting the density properties of subsurface materials. The atomic interferometer method depends on the wave nature of particles and measures the difference in phase between the wave functions of atoms at different positions in space to obtain the gradient of Earth's gravitational field [2].

One particular interest in the AMO community is the interaction of microwave fields with atoms because certain frequency spacing between energy levels in alkali atoms lie in the radio to microwave frequency regime. Traditionally, microwave sensing has been used for imaging dielectric bodies, as in remote sensing, i.e. imaging weather patterns, and shorter-range applications such as weapon detection [3]. An example of atom-microwave fields technology is the Rydberg-atom-based quantum receiver, which measures the entire radio-frequency range and surpasses the fundamental sensitivity, bandwidth, and frequency range of traditional electronics. Rydberg sensors use laser beams and amplitude-modulated microwave fields from a circuit to excite atoms into high energy Rydberg states. These highly excited states are extremely sensitive changes to the microwave circuit's voltage [4]. The RF signals are transduced into optical signals, which are detected via optical homodyne on a balanced photodetector. Other AMO applications of microwave fields include atomic-to-microwave optical transduction [5] and microwave-optical double resonance-based atomic clocks [6]. Atomic frequency standards are one of the most stable frequency references available. Standard atomic clocks vibrate at microwave frequencies, ap-

proximately 9 billion cycles per second, while optical atomic clocks vibrate at a much faster rate of about 500 000 billion cycles per second [7]. No electronic system can directly count the oscillations of optical clocks, and so optical clocks must be combined with optical frequency combs, which divide their oscillations into lower frequencies that can be linked with microwave standards. There is now demand for portable, chip-scale, low-power atomic clocks [8]. One of the main challenges of miniaturization is the size reduction of the microwave cavity resonator [MWR] [used to confine the microwave field for enhancing atom-field interactions] to below the wavelength of the atomic transition [9]. Existing solutions for millimeter-sized cells include strip-lines and micro-coupling loops [10], as well as a novel μ -MWR composed of a multi-layer stack of planar loop-gap resonator structures printed onto substrates coupled to a coaxial fed strip-line, having a total volume less than 0.9 cm^3 [9].

Quantum sensing is not limited to communications or surveying applications - it also has a niche in biology. Atomic magnetometers now have the sensitivity to probe the human brain better than other methods, such as SQUID-based magnetometers, which are expensive and occupy large spaces, as they require cryogenics. In optically pumped magnetometers, the spins of the electrons are pumped by a laser such that they are aligned in the same direction. The presence of a magnetic field acts as a torque to the spins, altering the amount of absorption of laser light. By monitoring the light absorption, the magnetic field strength can be measured. In 2018, a team at the University of Nottingham demonstrated the use of an array of wearable optically pumped magnetometers mounted on a human subject's head and detected activity in the motor cortex when the subject moved their finger [11].

Microwave detection techniques have also been actively researched as an alternative to existing biomedical imaging modalities, for example, for imaging breast tumors [3, 12]. Microwave fields are non-ionizing, posing low health risk compared to X-ray imaging, and can penetrate many optically opaque mediums such as living tissue. They operate over the frequency range covering hundreds of megahertz to tens of

gigahertz, are low cost, and less time-consuming compared to magnetic resonance imaging. A few atomic microwave sensors have been recently demonstrated, including one capable of detecting microwave magnetic fields at arbitrary frequencies, from the gigahertz to tens of gigahertz regime [13].

At the heart of all these sensors are the vapor cells and optical components. With the advancements in quantum sensors, there is now demand for small, portable, or wearable quantum devices, which can be accomplished by reducing the size of the optical setup. About twenty years ago, researchers adopted silicon micromachining techniques to fabricate chip-sized atomic vapor cells, which can be made in large batches compared to the traditional glass-blowing method [8]. The precision of nanofabrication allows the integration of millimeter-sized optics components such as the vertical-cavity surface-emitting laser and waveguides.

The research presented here focuses on two aspects: the study of microwave-optical double resonance in warm rubidium vapor and the micro-fabrication of chip-sized rubidium vapor cells. We work with alkali atoms, which have a single outer valence electron that can interact with electromagnetic fields to change optical properties in the medium. In particular, we worked with the isotope ^{87}Rb , which has a natural abundance of approximately 27%. Our lab also focuses on ultracold atom experiments, and rubidium-87 is more easily cooled by evaporative cooling. Because of its positive scattering length, it also allows a more stable Bose-Einstein condensate. Therefore, the lasers we have available operate at frequencies corresponding to some of the optical transitions in ^{87}Rb and ^{85}Rb , the latter which has a high natural abundance of 72%. In principle, for the work demonstrated in this research, the isotope ^{85}Rb can be used, but we would need to re-design and enlarge the microwave cavity used in our microwave-assisted optical pumping experiment, as the ground-state hyperfine transition frequency is lower in ^{85}Rb . Other isotopes have a much smaller natural abundance, and would not provide us with the atomic number density sufficient for absorption spectroscopy.

First, in Chapter 2 of this thesis, I cover the basics of light-matter interactions from a semi-classical perspective relevant to our experiments. Then in Chapter 3, I present a vector magnetometry experiment based on microwave-optical double resonance [MODR], in which the atoms are pumped by both optical and microwave fields. I measured the strength of a DC magnetic field by looking at the double-resonance spectrum and study the relationship between the direction of the static field relative to the microwave field direction. I describe our setup, discuss MODR theory, and provide preliminary data. In Chapter 4, I demonstrate the micro-fabrication of millimeter-sized vapor cells and show the results of our test for the presence of rubidium inside these cells. I outline the process flow step-by-step and conclude the chapter by discussing improvements in the fabrication process that would make them suitable for magnetometry purposes.

Chapter 2

Atomic Physics

In this chapter, we will briefly introduce alkali atoms, cover the origins of atomic energy levels, and discuss absorption spectroscopy using a two-level atom model, which will help us better understand how we use light to probe the energy levels of an atomic vapor.

2.1 Alkali Atoms

Alkali metal atoms, which are soft, shiny, and have a low melting temperature, are the group of atoms in which chemical elements lithium [Li], sodium [Na], potassium [K], rubidium [Rb], and francium [Fr] belong. They have a single unpaired electron, called the valence electron, in their outermost electronic orbital. Alkali atoms are used in quantum sensing applications because their optical properties can be manipulated by interacting the atoms, and hence their electrons, with electromagnetic fields. Being unpaired, the electron can be readily lost, making alkali metals very reactive at room temperature and standard atmospheric pressure. Only unpaired electrons will exhibit the spin properties described in this chapter. The energy of an alkali metal can be approximated by considering only the outermost electron and the nucleus. Although not part of the alkali group, hydrogen is in the same column as alkali atoms in the periodic table, labeled Group 1A. In the classical picture, the hydrogen atom is composed of one negatively charged electron that orbits around a nucleus formed from

a single positive charge, the proton. The electronic wave function of the hydrogen atom is well-studied and the results obtained for the hydrogen atom can be transposed to the case of rubidium atoms, the type of alkali atoms used in this research. Rubidium atoms are well studied, and their properties are well-documented, allowing us to better design experimental parameters.

2.2 Atomic and Interaction Hamiltonian

In this section, we give an expression for the general Hamiltonian that describes the interaction of a particle of charge q with a time-dependent electromagnetic field. Consider an electromagnetic wave with wave vector \mathbf{k} and angular frequency $\omega = ck$, where c is the speed of light and $k = |\mathbf{k}|$. In terms of the vector and scalar potentials $\mathbf{A}(\mathbf{r}, t)$ and $\varphi(\mathbf{r}, t)$ respectively, the electric field is

$$\mathbf{E}(\mathbf{r}, t) = -\frac{\partial A(\mathbf{r}, t)}{\partial t} - \nabla\varphi \quad (2.1)$$

and the magnetic field is

$$\mathbf{B}(\mathbf{r}, t) = \nabla \times \mathbf{A}(\mathbf{r}, t). \quad (2.2)$$

With a suitable choice of gauge, we can set $\varphi = 0$ and consider only $\mathbf{A}(\mathbf{r}, t)$, which has the form

$$\mathbf{A}(\mathbf{r}, t) = A_o e^{ikz - i\omega t} \mathbf{e}_{\text{rad}} + A_o^* e^{-(ikz - i\omega t)} \mathbf{e}_{\text{rad}}, \quad (2.3)$$

where \mathbf{e}_{rad} is the polarization direction of the vector potential and is the same as the electric field polarization. The amplitude of the vector potential, A_o , is related to the amplitude of the electric field, E_o , via $A_o = E_o/(2i\omega)$. The general Hamiltonian for a particle of mass m and charge q in a gauge potential is

$$\hat{\mathbf{H}} = \frac{1}{2m} [\hat{\mathbf{p}} - q\mathbf{A}(\mathbf{r}, t)]^2 + V(\mathbf{r}) - \frac{q}{m} \mathbf{S} \cdot \mathbf{B}, \quad (2.4)$$

where $\hat{\mathbf{p}}$ is the momentum operator of the particle and $V(\mathbf{r})$ is the potential energy of the system in which the particle resides. Usually, the momentum term is much larger

than the vector potential term. In position space, the momentum operator is given by $\hat{\mathbf{p}} = -i\hbar\nabla$, where $\nabla = \sum_i^n \mathbf{e}_i \partial/\partial x_i$ is the vector differential operator. The first term in the Hamiltonian accounts for the force of the electromagnetic field, while the last term accounts for the magnetic field acting on the spin. We can separate this Hamiltonian into a part containing the non-relativistic atomic Hamiltonian \hat{H}_o that is intrinsic to the particle,

$$\hat{H}_o = \frac{\hat{\mathbf{p}}^2}{2m} + V(\mathbf{r}) = -\frac{\hbar^2 \nabla^2}{2m} + V(\mathbf{r}), \quad (2.5)$$

and a part containing terms where the particle interacts with the field,

$$\hat{H}_{\text{int}} = -\frac{q}{m} \mathbf{A}(\mathbf{r}, t) \cdot \hat{\mathbf{p}} - \frac{q}{m} \hat{\mathbf{S}} \cdot \mathbf{B}(\mathbf{r}, t) + \frac{q^2}{2m} [\mathbf{A}(\mathbf{r}, t)]^2. \quad (2.6)$$

The interaction Hamiltonian can be expanded into terms with different orders, corresponding to electric-dipole [Section 2.5.1], magnetic-dipole [Section 2.5.2], electric-quadrupole, magnetic-quadrupole and higher-order terms. In the next section, we will use our atomic Hamiltonian in Eq. 2.5 to solve for the energy states of an atom.

2.3 Energy States

2.3.1 Orbital Angular Momentum

We now consider the charged particle to be an electron of charge $-e$, mass m that orbits around a positively charged nucleus with Z positive charges e , mass M , in a single-electron atomic system. The electron and the nucleus interact due to the Coulomb potential given by,

$$V_C(\mathbf{r}) = -\frac{Ze^2}{4\pi\epsilon_o|\mathbf{r}|}, \quad (2.7)$$

where ϵ_o is the permittivity of free space and $|\mathbf{r}|$ is the absolute distance between the electron and the nucleus. This form of the potential energy in an atomic system neglects relativistic effects and the intrinsic spin angular momentum of the electron and the nucleus.

The Coulomb interaction between the electron and the positively charged nucleus causes the electron to reside in discrete energy levels characterized by principal quantum number n . The energy levels E_n are found from the eigenvalue equation,

$$\hat{H} |\psi(\mathbf{r})\rangle = E_n |\psi(\mathbf{r})\rangle, \quad (2.8)$$

where \hat{H} is the Hamiltonian that is associated with the energy of the system [the $\hat{\cdot}$ denotes an operator], $|\psi(\mathbf{r})\rangle$ is the eigenfunction that corresponds to the wave function of the electron, and $|\mathbf{r}|$ is the electron-proton distance. For a review on matrix representation of state vectors and operators, see Appendix A. If there are no external fields, considering only the effect of the nucleus, the Hamiltonian for this system is the atomic Hamiltonian,

$$\hat{H} = \hat{H}_{\text{at}} = \frac{\hat{\mathbf{p}}^2}{2\mu} + V_C(\mathbf{r}), \quad (2.9)$$

where $\mu = Mm/(M+m)$ is the reduced mass of the system. If $M \gg m$, then $\mu \approx m$, and Eq. 2.9 reduces to Eq. 2.5. The first term in the Hamiltonian represents the kinetic energy of the atom in the center of mass frame. From the eigenvalue equation Eq. 2.8, we can solve for the eigenfunctions and eigenvalues, which give the wave functions and the energy levels of the atomic system, respectively. In spherical coordinates, where ϕ is the azimuthal angle and θ the polar angle, the wave function split into radial and angular components is

$$\psi_n(r, \theta, \phi) = R_{n,\ell}(r)Y_{\ell,m_\ell}(\theta, \phi). \quad (2.10)$$

$R_{n,\ell}(r)$ is the radial part of the wave function and $Y_{\ell,m_\ell}(\theta, \phi)$ is the angular dependent part. The radial part depends on two integers, n and ℓ , and has the form

$$R_{n,\ell}(r) \propto e^{-r/a_0 n} \left[\frac{2r}{na_0} \right]^\ell \mathcal{L}_{n-\ell-1}^{2\ell+1} \left(\frac{2r}{na_0} \right), \quad (2.11)$$

where a_0 is the Bohr radius and $\mathcal{L}(x)$ are the associated Laguerre polynomials. The spherical component depends on two integers, l and m_l , and has the form

$$Y_{\ell,m_\ell}(\theta, \phi) = \ell(\ell+1)\mathcal{P}_{\ell,m_\ell}(\cos\theta)e^{im_\ell\phi}, \quad (2.12)$$

where $\mathcal{P}_{\ell,m}(x)$ are the associated Legendre polynomials. In Dirac notation, eigenfunctions of the electron are written as $|n, \ell, m_\ell\rangle$. Here, n is the principal quantum number and can take on integer values from $1, 2, \dots, \infty$. The orbital angular momentum quantum number ℓ can assume values $0, 1, \dots, n - 1$. For the single-electron atom, the energy levels that satisfy Eq. 2.8 for the wave function in Eq. 2.10 are given by

$$E_n = -hcR_\infty \frac{1}{n^2}, \quad (2.13)$$

which is n^2 -fold degenerate, as there are multiple states for a given n that have this energy. When $\ell = 0$, the electron is said to be in the ground, or S , state. When $\ell = 1$, the electron is in the first excited, or P , state. Physically, this orbital angular momentum arises from the electron orbiting around the nucleus. The orbital angular momentum operator $\hat{\mathbf{I}}$ is related to the quantum number ℓ through

$$\hat{\mathbf{I}}^2 |n, \ell, m_\ell\rangle = \hbar^2 \ell(\ell + 1) |n, \ell, m_\ell\rangle. \quad (2.14)$$

The magnitude of the orbital angular momentum $\hat{\ell}$ can be obtained from Eq. 2.14,

$$|\hat{\ell}| = \sqrt{\langle n, \ell, m_\ell | \hat{\mathbf{I}} \cdot \hat{\mathbf{I}} | n, \ell, m_\ell \rangle} = \hbar \sqrt{\ell(\ell + 1)}. \quad (2.15)$$

Note that $\hat{\mathbf{I}} = \hat{l}_x \mathbf{e}_x + \hat{l}_y \mathbf{e}_y + \hat{l}_z \mathbf{e}_z$ is a vector operator specified by its magnitude and direction [14]. However, in quantum mechanics, it is impossible to know the direction in space. In other words, we cannot simultaneously know all three components of the angular momentum. The maximal information we can obtain is the projection of angular momentum along a chosen axis called the quantization axis. For the rest of this thesis, the z -axis will be chosen as our quantization axis. The projection of angular momentum along this axis is

$$l_z = \hat{l}_z |n, \ell, m_\ell\rangle = m_\ell \hbar |n, \ell, m_\ell\rangle, \quad (2.16)$$

where m_ℓ can take on integer values $-\ell, -\ell + 1, \dots, 0, \dots, \ell - 1, \ell$. The x and y components of the angular momentum can be obtained from the raising and lowering

operators which satisfy

$$\hat{\ell}_{\pm} |\ell, m_{\ell}\rangle = \hbar \sqrt{(\ell \mp m_{\ell})(\ell \pm m_{\ell} + 1)} |\ell, m_{\ell} \pm 1\rangle \quad (2.17)$$

which can be shown using the relations

$$\hat{\ell}_x = \frac{1}{2} (\hat{\ell}_+ + \hat{\ell}_-) \quad (2.18a)$$

$$\hat{\ell}_y = -\frac{i}{2} (\hat{\ell}_+ - \hat{\ell}_-). \quad (2.18b)$$

The raising and lowering operators act on states $|\ell, m_{\ell}\rangle$ by adding or removing one unit of angular momentum, bringing the particle to the final state $|\ell, m_{\ell} \pm 1\rangle$. Experimentally, this can be achieved with a time-dependent oscillating electric field with left and right-hand polarization [Section 2.5.1].

2.3.2 Time Dependence

In the previous section, we did not consider the time dependence of the system. However, to describe quantum motion, we need to consider how a system in a particular state $|\psi(t)\rangle$ evolves with time. This time evolution is governed by Schrödinger's equation

$$i\hbar \frac{\partial}{\partial t} |\psi(t)\rangle = \hat{H} |\psi(t)\rangle. \quad (2.19)$$

Equation 2.19 can be used to look at the evolution of energy eigenstates $|\psi_n\rangle$ of a Hamiltonian

$$i\hbar \frac{\partial}{\partial t} |\psi_n(t)\rangle = \hat{H} |\psi_n(t)\rangle = E_n |\psi_n(t)\rangle, \quad (2.20)$$

where E_n are the eigenvalues. The solution to this first order differential equation for $|\psi_n(t)\rangle$ is

$$|\psi_n(t)\rangle = e^{-iE_n t/\hbar} |\psi_n(0)\rangle. \quad (2.21)$$

The effect of time evolution is to multiply the initial state by a phase factor $e^{-iE_n t/\hbar}$. Since the phase does not influence the outcome of an observation, we can see that a system in an eigenstate is a stationary state and does not evolve. Therefore, if an

electron finds itself in the state $|n, \ell, m\rangle$, it will remain in that state forever. In this case, we say that the quantum numbers n, ℓ, m are “good quantum numbers”. Good quantum numbers are so named because the operators associated with these numbers commute with the total Hamiltonian of the system, satisfying the eigenvalue equation. The eigenvalues are conserved quantities - the state does not evolve. Physically, this means that the wave function does not change if there are no other perturbations to the system. Of course, in reality, atomic systems are constantly perturbed; external factors such as collisions and interactions with the environment can cause their states to evolve.

2.3.3 Spin Angular Momentum

In addition to orbital angular momentum, the electron also has intrinsic angular momentum caused by a quantum property called spin. The spin appears naturally from the Dirac equation, which is an equation for the electron that satisfies both the postulates of special relativity and quantum mechanics [15]. For a single electron, the spin quantum number is $s = 1/2$. The modulus of the spin angular momentum is always [14]

$$|\hat{\mathbf{s}}| = \sqrt{s(s+1)}\hbar, \quad (2.22)$$

and the projection of the spin angular momentum along the quantization axis is $s_z = m_s\hbar$, where $m_s = \pm\frac{1}{2}$ is the magnetic spin quantum number. Including the effect of spin, the eigenfunction of the electron in Dirac notation is labelled as $|n, l, m_l, s, m_s\rangle$.

The nucleus also has spin and orbital angular momentum, denoted by $\hat{\mathbf{I}}$. For the isotope ^{87}Rb , the value of the quantum number I is $3/2$. that we use lower case letters for a single electron or single proton system, and capital letters for a system that is multi-electron or multi-proton.

2.3.4 Quantum Defect

For hydrogen atoms, the energy levels depend only on n , not ℓ . But for atoms with more than one electron, such as alkali atoms, this is not the case: the energy levels are not degenerate. This is due to the screening effect, where electrons closer to the nucleus see more of the nuclear charge, while electrons further away are “screened” by other electrons and experience almost the same potential as in a hydrogen atom. Therefore, s -electrons are lower in energy than p -electrons. The correction for the energy levels in a multi-electron atom is [16]

$$E_{n,\ell} = -hc \frac{R_\infty}{(n - \delta_\ell)^2}, \quad (2.23)$$

where δ_ℓ is a quantity known as the quantum defect.

2.3.5 Fine Structure and Total Electronic Angular Momentum

Relativistic effects lead to small shifts in the atomic energy called the fine-structure splitting. The fine-structure Hamiltonian is

$$\hat{H}_{\text{FS}} = \frac{1}{2m^2c^2} \frac{1}{R} \frac{dV(r)}{dr} \hat{\ell} \cdot \hat{s} - \frac{\hat{\mathbf{p}}^4}{8m^3c^2} + \frac{h^2}{8m^2c^2} \nabla^2 V(r). \quad (2.24)$$

The first term contributing to the fine-structure splitting is due to spin-orbit interaction, which couples the orbital and spin angular momentum of the electron. The interaction arises from the motion of the electron in the electrostatic field created by the positively charged nucleus. Special relativity indicates that, in the electron’s rest frame, the orbiting of the nucleus around the electron produces a magnetic field. This magnetic field interacts with the magnetic moment of the electron associated with its spin. The Hamiltonian has the form $\xi \hat{\ell} \cdot \hat{s}$, where ξ is the spin-orbit coupling constant and is typically measured. When the spin-orbit interaction is taken into account, the quantum numbers n, ℓ, m_ℓ, s, m_s are no longer “good quantum numbers” because the hyperfine structure Hamiltonian does not commute with $\hat{\ell}$ and \hat{s} , due to

its $\hat{\boldsymbol{\ell}} \cdot \hat{\boldsymbol{s}}$ term. Instead, we need to consider the total electronic angular momentum operator $\hat{\mathbf{j}} = \hat{\mathbf{l}} + \hat{\mathbf{s}}$, which does commute with \hat{H}_{FS} , as well as a new set of eigenstates $|n, \ell, s, j, m_j\rangle$. When working with a state of fixed n, ℓ, s , it is common to label an eigenstate by its total [electronic] angular momentum. For example, $|n, \ell, s, j, m_j\rangle$ becomes $|j, m_j\rangle$. The magnitude of the total electronic angular momentum \mathbf{j} is related to the quantum number j ,

$$|\hat{\mathbf{j}}| = \sqrt{j(j+1)}\hbar, \quad (2.25)$$

where j lies in the range

$$|\ell - s| \leq j \leq \ell + s. \quad (2.26)$$

Due to the spin-orbit interaction, the energy level of a state $|j, m_j\rangle$ is shifted by an amount

$$E_{\text{SO}} = \langle j, m_j | \xi \hat{\boldsymbol{\ell}} \cdot \hat{\boldsymbol{s}} | j, m_j \rangle = \frac{\xi}{2} [j(j+1) - \ell(\ell+1) - s(s+1)]. \quad (2.27)$$

For heavier atoms such as rubidium, the spin-orbit coupling can be significant. Other terms that contribute to the fine-structure splitting arise from the relativistic variation of the electron mass with its velocity [second term], and from the non-local interaction between the electron and the Coulomb field, called the Darwin term [third term], in which the electron is affected by all the values taken on by the field in a region centered at the point \mathbf{r} , instead of the value of the field at point \mathbf{r} [15]. The Darwin correction only affects electrons in the ground state where $\ell = 0$. Compared to the non-relativistic Hamiltonian H_o , the fine-structure Hamiltonian terms are an order α^2 smaller, where $\alpha \approx 1/137$ is the fine-structure constant.

2.3.6 Russell-Saunders Notation

The energy state of an atom in the eigenstate $|n, \ell, j = \ell + s\rangle$ can be written as $n^{2s+1}\ell_j$. This is called the Russell-Saunders notation. For example, for the valence electron in the $n = 5$ shell of ^{87}Rb , the ground state is written as $5^2S_{1/2}$. The first excited state, with $n = 5$, $\ell = 1$, splits into two states $j = \ell \pm 1/2 = 1/2, 3/2$, due to fine-structure

splitting. These two excited states are written as $5^2P_{1/2}$ and $5^2P_{3/2}$. This results in the D_1 and D_2 transitions, as shown in Fig. 2.1 for ^{87}Rb [a D transition is a transition from $\ell = 0$ to $\ell = 1$].

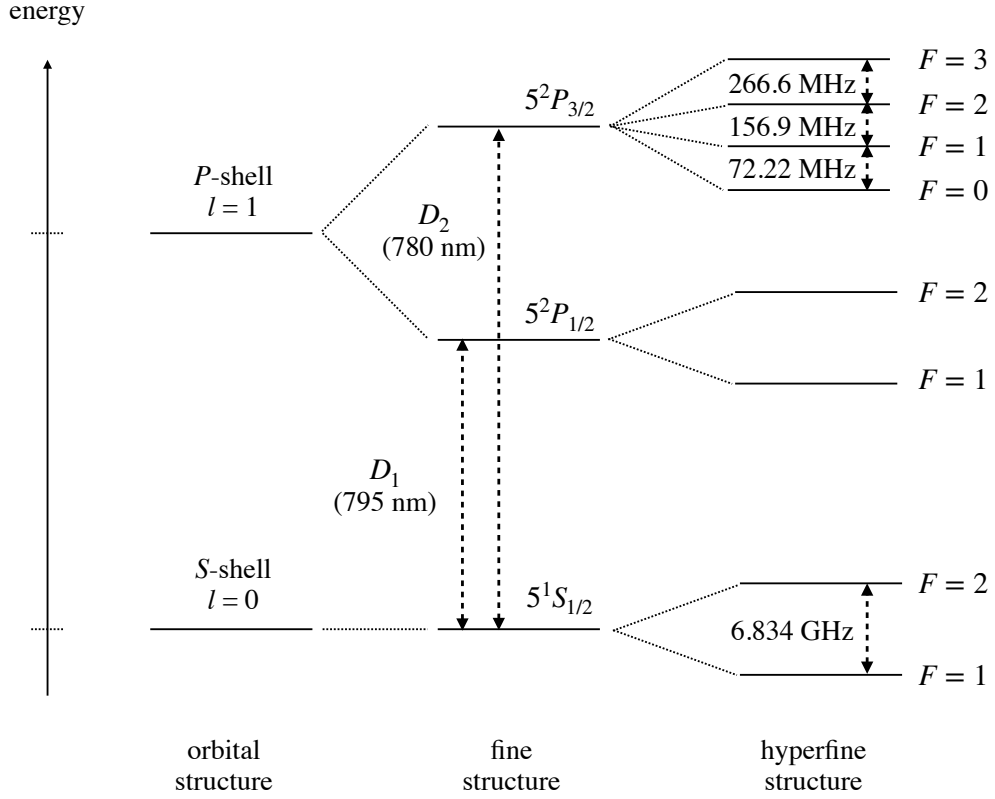


Figure 2.1: Energy level diagram for the $n = 5$ shell of ^{87}Rb , where the valence electron resides. The S and the P shell are split due to screening effects and other factors. Adapted from [17].

2.3.7 Hyperfine Structure and Total Angular Momentum

Associated with the spin $\hat{\mathbf{I}}$ of a nucleus is a magnetic moment equal to $\hat{\boldsymbol{\mu}}_I = g_I \mu_N \hat{\mathbf{I}}$, where μ_N is the nuclear Bohr magneton and g_I the nuclear g -factor. In its own rest frame, the nucleus sees the orbiting electron as an effective magnetic field \mathbf{B}_{eff} and interacts with it. The hyperfine Hamiltonian describing this interaction is

$$\hat{H}_{\text{HFS}} = A_{\text{HFS}} \hat{\mathbf{I}} \cdot \hat{\mathbf{j}}, \quad (2.28)$$

where A_{HFS} is the hyperfine constant. Note that for ground-state electrons, $\hat{\mathbf{j}} = \hat{\mathbf{s}}$. When the hyperfine splitting effect is in play, the quantum numbers j , m_j are no longer good quantum numbers. We define a new quantum number $\hat{\mathbf{F}} = \hat{\mathbf{I}} + \hat{\mathbf{j}}$, an operator associated with the total atomic angular momentum. The projection of the total angular momentum along the quantization axis, m_F , are integers in the range $-F \leq m_F \leq F$. The corresponding eigenstates $|F, m_F\rangle$ are eigenstates of $\hat{\ell}^2, \hat{s}^2, \hat{\mathbf{j}}^2, \hat{\mathbf{F}}^2$ and \hat{F}_z , but not of $\hat{\ell}_z, \hat{s}_z$ and \hat{j}_z . These new eigenstates can be written as superpositions of the $|j, m_j\rangle$ eigenstates using Clebsch-Gordan coefficients. The energy shift of the $|F, m_F\rangle$ states due to the hyperfine interaction is

$$E_{\text{HFS}} = \langle F, m_F | \hat{H}_{\text{HFS}} | F, m_F \rangle = \frac{A_{\text{HFS}}}{2} [F(F+1) - I(I+1) - j(j+1)]. \quad (2.29)$$

In the ground-state, the separation energy between adjacent levels $F \pm \frac{1}{2}$ is $\Delta E_{\text{HFS}} = 2A_{\text{HFS}}$; this is approximately 6.834 GHz for ^{87}Rb in units of \hbar . The hyperfine interaction lifts the degeneracies between levels of different F , but not between different m_F . For example, the $5^2S_{1/2}$ ground-state fine structure level of ^{87}Rb splits into two hyperfine states, $F = |1/2 - 3/2| = 1$ and $F = 3/2 + 1/2 = 2$. Each of these levels has $2F + 1$ sublevels, which are degenerate in the absence of a static magnetic field.

2.4 Zeeman Effect and the Hyperfine Structure

In the presence of an external static magnetic field \mathbf{B} , the m_F sublevels are not degenerate. Each Zeeman sublevel shifts by an amount proportional to the magnitude of the magnetic field. This energy shift is called the Zeeman shift. Physically, the magnetic moment $\boldsymbol{\mu}$ of the atoms interacts with the magnetic field, with the Zeeman interaction Hamiltonian given by,

$$\hat{H}_Z = -\boldsymbol{\mu} \cdot \mathbf{B}. \quad (2.30)$$

In the approximation that the nuclear magnetic moment is much smaller than the electron magnetic moment, the magnetic dipole moment in the presence of hyperfine

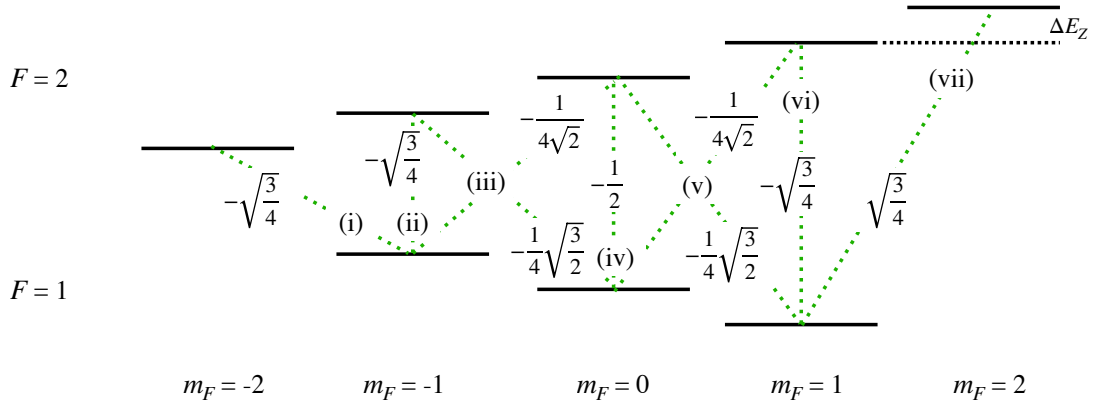


Figure 2.2: Energy level due to the low field Zeeman effect in the ground state of ^{87}Rb . Adjacent sublevels are shifted by an amount $\Delta E_Z = \hbar\omega_L$. Nine possible magnetic dipole transitions exist at seven different frequencies. The magnitude of the matrix elements of these transitions are labeled. Transitions *(iii)* and *(iv)* have a degeneracy of two.

splitting is

$$\hat{\boldsymbol{\mu}} = g_J\mu_B\hat{\mathbf{J}} + g_I\mu_N\hat{\mathbf{I}} \approx g_J\mu_B\hat{\mathbf{J}}. \quad (2.31)$$

Here $\mu_B = -\frac{e\hbar}{2m}$ is the Bohr magneton, which is a measure of how much magnetic moment there is for every bit of charge q , and μ_N is the nuclear Bohr magneton, which is much smaller than μ_B .

When the field strength is low, the Zeeman shift is smaller than the hyperfine splitting: $\langle H_Z \rangle \ll \langle H_{\text{HFS}} \rangle$, and the magnetic field interaction acts as a perturbation to the hyperfine interaction. In this situation, F and m_F are good quantum numbers and can be used to describe the state of the atom. We may wish then to write \hat{H}_Z as a function of $\hat{\mathbf{F}}$. This can be done via the Wigner-Eckart theorem, which says that for any operator $\hat{\mathbf{V}}$ whose effect is small compared to another operator $\hat{\mathbf{J}}$ acting on state $|J, m_J\rangle$, $\hat{\mathbf{V}}$ can be expressed in terms of $\hat{\mathbf{J}}$ by projecting $\hat{\mathbf{V}}$ onto $\hat{\mathbf{J}}$:

$$\hat{\mathbf{V}} = \left\{ \frac{\langle J, m_J | \hat{\mathbf{V}} \cdot \hat{\mathbf{J}} | J, m_J \rangle}{J(J+1)} \right\} \hat{\mathbf{J}}. \quad (2.32)$$

The term in curly brackets is just a number and determines how much of $\hat{\mathbf{V}}$ is in the new operator $\hat{\mathbf{J}}$. This theorem is also known as the projection theorem. To replace

$\hat{\mathbf{j}}$ in \hat{H}_Z with $\hat{\mathbf{F}}$, we project $\hat{\mathbf{j}}$ onto $\hat{\mathbf{F}}$. The resulting Hamiltonian in the basis of $\hat{\mathbf{F}}$ simplifies to

$$\hat{H}_Z = g_F \mu_B \hat{\mathbf{F}} \cdot \mathbf{B}. \quad (2.33)$$

where the factor g_F is given by

$$g_F = g_J \left[\frac{1}{2} + \frac{J(J+1) - I(I+1)}{2F(F+1)} \right]. \quad (2.34)$$

For ^{87}Rb , the Landé factor g_J is approximately equal to 2. Thus, for $F = 1$, $g_F = -1/2$, and for $F = 2$, $g_F = 1/2$. If we choose the direction of the magnetic field as our quantization axis, so that $\hat{\mathbf{F}} \cdot \mathbf{B} = F_z |\mathbf{B}|$, the low-field Zeeman energy shift is

$$E_Z = g_F \mu_B |\mathbf{B}| \times \langle F, m_F | F_z | F, m_F \rangle = g_F m_F \mu_B |\mathbf{B}|, \quad (2.35)$$

which is linear in magnetic field strength. Figure 2.2 shows a visual representation of Zeeman energy shifts for the ground state of ^{87}Rb . The energy difference between adjacent m_F sublevels is $\Delta E_Z = g_F \mu_B B = \hbar \omega_L$, where ω_L is the Larmor frequency. Measuring the Larmor frequency provides a method for magnetometry, discussed in Section 3.1. Note that the $m_F = 0$ sublevel is unaffected by the magnetic field in this approximation. In our experiments, we work in the low magnetic field regime, so we refrain from discussing the high-field Zeeman effect.

2.5 Atom-Laser Interactions

We now turn our attention back to the interaction Hamiltonian, Eq. 2.6, which describes a charged particle interacting with an oscillating electromagnetic field. We restrict our discussion to electric-dipole and magnetic-dipole interactions and ignore higher-order terms in the Hamiltonian.

2.5.1 Electric-Dipole Transitions

The leading term in the interaction Hamiltonian is the first term. If we suppose that the spatial distance over which the interaction occurs is of the order of the atom's

size, then $e^{ikz} = 1 + (ikz) + (ikz)^2/2 + \dots \approx 1$. Working in the basis of the eigenstates of H_o ,

$$\hat{H}_o |\psi_i\rangle = h\omega_i |\psi_i\rangle \quad (2.36)$$

and considering only transitions where the electromagnetic field is near-resonant to the transition between two states $|\psi_1\rangle$ and $|\psi_2\rangle$,

$$\omega \approx \omega_2 - \omega_1, \quad (2.37)$$

we can use the commutation relationship

$$\hat{\mathbf{p}} = \frac{im}{\hbar} [\hat{\mathbf{r}}, \hat{H}_o], \quad (2.38)$$

to express the first term in Eq. 2.6 $[\frac{q}{m} \mathbf{A} \cdot \hat{\mathbf{p}}]$ as

$$\hat{H}_{E1} = -\frac{q}{2} E_o (e^{-i\omega t} + e^{+i\omega t}) \mathbf{e}_{\text{rad}} \cdot \hat{\mathbf{r}} = -q \mathbf{E}(t) \cdot \hat{\mathbf{r}}. \quad (2.39)$$

This Hamiltonian is the electric-dipole [E1] Hamiltonian and describes the interaction between the oscillating electric field and the charged particle. Assuming that $E_2 > E_1$, the first term $e^{-i\omega t}$ corresponds to an absorption process, while the second term with $e^{i\omega t}$ corresponds to a spontaneous emission process. The physical implications are as follows: when the oscillating electromagnetic field interacts with an atomic gas, it induces oscillating electric-dipole moments in the atoms. The average dipole moment of the ensemble orients itself along the direction of the field. In an isotropic medium, this field generates a polarization $\mathbf{P}(\omega)$ proportional to the electric field,

$$\mathbf{P}(\omega) = \epsilon_o \chi(\omega) \mathbf{E}(\omega). \quad (2.40)$$

The proportionality factor is determined by the linear susceptibility $\chi(\omega)$, given by the quadrature components of the oscillating dipole moments. It provides information on the absorption and dispersion properties of the gas. These optical properties can be measured by looking at the absorption of an oscillating electromagnetic field in the atomic medium. Note that in an anisotropic medium, the relationship between

the polarization and the electric field are related by the susceptibility tensor, which can induce birefringence [see Section 3.1].

The oscillating field can impart angular momentum to the electron and excite it to a state with higher angular momentum. We can derive the “selection rules” for allowed transitions between an initial state $|n_i, \ell_i, m_i\rangle = R_{n_i, \ell_i} \times Y_{\ell_i, m_i}$ and a final state $|n_f, \ell_f, m_f\rangle = R_{n_f, \ell_f} \times Y_{\ell_f, m_f}$ by looking at the static part of $\langle \ell_f, m_f | H_{\text{E1}} | \ell_i, m_i \rangle$

$$-eE_0 \langle \ell_f, m_f | \mathbf{e}_{\text{rad}} \cdot \hat{\mathbf{r}} | \ell_i, m_i \rangle = \mathcal{D}_{12} \mathcal{I}_{\text{ang}}, \quad (2.41)$$

The equation has been separated into a radial part \mathcal{D}_{12} depending only on r and an angular part depending only on θ and ϕ . Expressed as an integral, the angular part in position space is

$$\mathcal{I}_{\text{ang}} = \int_0^{2\pi} \sin \theta d\theta \int_0^\pi Y_{\ell_f, m_f}^*(\theta, \phi) \left(\frac{\mathbf{r}}{|\mathbf{r}|} \cdot \mathbf{e}_{\text{rad}} Y_{\ell_i, m_i}(\theta, \phi) \right). \quad (2.42)$$

and is non-zero unless $\Delta \ell = \ell_f - \ell_i = \pm 1$, meaning that the electric-dipole Hamiltonian drives only transitions from the final state $|\ell_f = l \pm 1, m_f\rangle$ from the initial state $|\ell_i = l, m_i\rangle$. The frequency difference between states corresponding to such transitions is usually in the optical regime. Depending on the polarization of the electric field, there are three possible values for $\Delta m = m_f - m_i$: $\Delta m = 0, \pm 1$, corresponding to a π - and σ_{\pm} -transition, respectively. A π -transition is excited by light polarized linearly along the quantization axis,

$$\mathbf{E}_{\pi}(t) = E_o \text{Re}\{e^{i\omega t}\} \mathbf{e}_z = E_o \cos(\omega t) \mathbf{e}_z, \quad (2.43)$$

while σ_{\mp} transitions are excited by left and right circularly polarized light, respectively,

$$\mathbf{E}_{\sigma_-} = E_o \text{Re}\left\{e^{i\omega t} \left(\frac{\mathbf{e}_x - i\mathbf{e}_y}{\sqrt{2}} \right)\right\} = \frac{E_o}{\sqrt{2}} [\cos(\omega t) \mathbf{e}_x - \sin(\omega t) \mathbf{e}_y] \quad (2.44a)$$

$$\mathbf{E}_{\sigma_+} = E_o \text{Re}\left\{e^{i\omega t} \left(\frac{\mathbf{e}_x + i\mathbf{e}_y}{\sqrt{2}} \right)\right\} = \frac{E_o}{\sqrt{2}} [\cos(\omega t) \mathbf{e}_x + \sin(\omega t) \mathbf{e}_y] \quad (2.44b)$$

The time dependence of the different electric fields is shown in Fig. 2.3. Physically, polarization can be thought of as carrying angular momentum that can be transferred to the electron to change its angular momentum state. A π -transition corresponds to a situation where there is no change in electronic angular momentum along $\pm z$ since the force from the electric field is parallel to z . For σ_+ transitions, electronic angular momentum is added along the $+z$ direction, while for σ_- transitions, angular momentum can be thought of as being removed from the atom along $+z$, or as being added along $-z$.

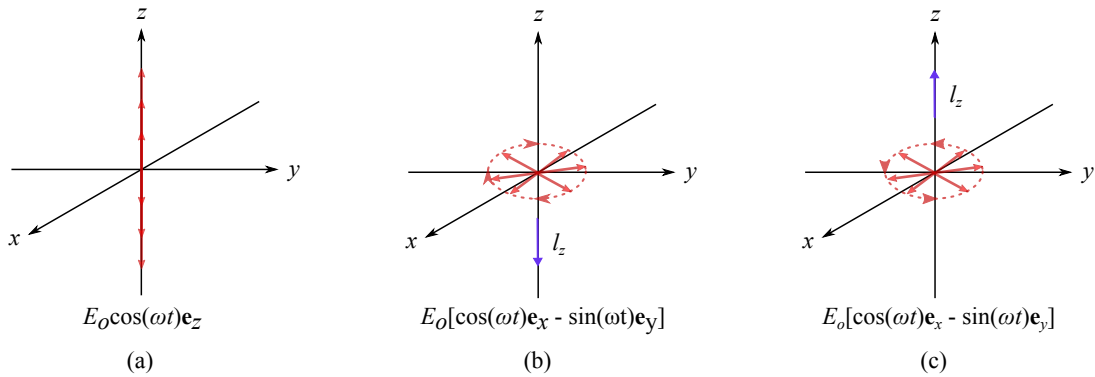


Figure 2.3: (a) Linearly polarized light does not change the angular momentum along the quantization axis z , driving π -transitions, (b) left circularly polarized light removes angular momentum, driving σ_- transitions, and (c) right circularly polarized light adds angular angular momentum, driving σ_+ transitions. The red arrows indicate the time dependence of the direction of the electric field.

2.5.2 Magnetic Dipole Interactions

The next higher-order term is the magnetic dipole [M1] interaction, generated by the interactions between an oscillating magnetic field $\mathbf{B}(t)$ with the electronic, spin, and nuclear magnetic moments. The magnitude of M1 interactions is usually smaller than E1 interactions by a factor of a_o/λ , where λ is the corresponding wavelength of the transition. Magnetic dipole interactions have different selection rules. This can be

seen from the M1 interaction Hamiltonian

$$H_{M1} = \left(\mu_B \hat{\mathbf{I}} + g_s \mu_B \hat{\mathbf{s}} - g_I \mu_B \hat{\mathbf{I}} \right) \cdot \mathbf{B}(t), \quad (2.45)$$

which, unlike the E1 Hamiltonian, does not have spatial dependence [no dependence on \mathbf{r}]. The magnetic field interacts only with the orbital and spin angular momentum of the electron. Since there is no spatial dependence in the Hamiltonian and neither operators $\hat{\mathbf{I}}$ nor $\hat{\mathbf{s}}$ changes the quantum numbers ℓ and s , the selection rules for M1 transitions must be $\Delta l = 0$ and $\Delta s = 0$. However, components of ℓ or s perpendicular to the quantization axis can induce transitions in which $\Delta m_{\ell,s} = \pm 1$, and components parallel to z can induce transitions where $\Delta m_{\ell,s} = 0$. Transitions where $\Delta f = 0, \pm 1$ and $\Delta j = 0, \pm 1$ are permitted, with the restriction that $j_i = 0 \rightarrow j_f = 0$ and $F_i = 0 \rightarrow F_f = 0$ are not allowed.

Microwave-Induced Ground State Transitions

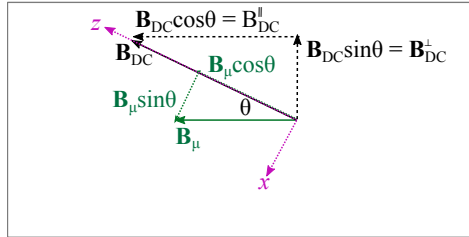


Figure 2.4: The microwave field \mathbf{B}_μ lies at an angle θ with respect to the static magnetic field \mathbf{B}_{DC} . \mathbf{B}_μ is confined along the axis of a microwave cavity. \mathbf{B}_{DC} defines the quantization axis.

Consider a linearly polarized microwave field of the form $\mathbf{B} = \mathbf{B}_\mu \cos(\omega_\mu t)$ that couples the two hyperfine ground states, $|F = 1, m_F\rangle$ and $|F' = 2, m_{F'}\rangle$, in an ensemble of ^{87}Rb atoms. Suppose that a weak external static magnetic field is applied along \mathbf{e}_z , lifting the degeneracies of the Zeeman sublevels, and defining the quantization axis. The polarization of the microwave field lies in the xz -plane at an angle θ with respect to the magnetic field direction, as shown in Fig. 2.4. In this DC field strength

regime, F , and m_F are good quantum numbers. There are nine possible magnetic dipole transitions, indicated by the dotted green lines in Fig. 2.2, but two pairs of them, labeled by (iii) and (iv) have the same frequency. In the approximation that the nuclear magnetic moment is small compared to the electronic magnetic moment, the magnetic dipole interaction Hamiltonian is, from Eq. 2.45,

$$\hat{H}_\mu = g_J \mu_B \hat{\mathbf{S}} \cdot \mathbf{B}_\mu \cos(\omega_\mu t) \quad (2.46)$$

$$= g_J \mu_B \left(\hat{S}_x B_\mu \sin \theta \mathbf{e}_x + \hat{S}_z B_\mu \cos \theta \mathbf{e}_z \right). \quad (2.47)$$

As in Section 2.5.1, the π -transitions [$\Delta m_F = 0$] are induced by the component of the field parallel to the quantization axis,

$$B_\mu^\pi = \mathbf{B}_\mu \cdot \mathbf{e}_z = B_\mu \cos \theta. \quad (2.48)$$

and have transition amplitudes [18] equal to

$$M_\pi(I, m_F) = -\frac{\mu_B B_\mu^\pi}{2I + 1} \sqrt{I(I + 1) - m_F^2 + \frac{1}{4}}. \quad (2.49)$$

Since linearly polarized light is an equal superposition of left and right handed circularly polarized light, σ_\pm transitions [$\Delta m_F = \pm 1$], are induced by components of the field perpendicular to the quantization axis,

$$B_\mu^{\sigma_\pm} = \mathbf{B}_\mu \cdot \mathbf{e}_x = B_\mu \sin \theta. \quad (2.50)$$

The σ_\pm transition amplitudes between $F = I \pm \frac{1}{2}$ levels are equal to

$$M_{\sigma_\pm}(I, m_F) = \mp \frac{\mu_B B_\mu^{\sigma_\pm}}{2I + 1} \sqrt{(I \mp m_F)^2 - \frac{1}{4}}. \quad (2.51)$$

The amplitudes of the magnetic dipole matrix elements $M_{\pi, \sigma_\pm} = \langle F' = 2, m'_F | S_z | F = 1, m_F \rangle$ are labeled in Fig. 2.2.

In our experiment, the microwave field direction was fixed along the axis of a microwave-cavity resonator, but the direction of an external static magnetic field \mathbf{B}_{DC} could be varied. The full setup is presented in Section 3.2.

2.5.3 Two Level System

As an example on how the electromagnetic field induces transitions between states, we will study the dynamics of a two-level system under the influence of an electromagnetic field of the form $\mathbf{E}(t) = E_o \cos(\omega t) \mathbf{e}_{\text{rad}}$, which can be a monochromatic laser beam. We will assume that the oscillation frequency is near resonance to the transition between the two states, $\omega \approx (\omega_b - \omega_a) = \omega_o$. As before, we will work in the basis of atomic states; for a two-level system, the eigenstates are $|\psi_a(\mathbf{r})\rangle$ and $|\psi_b(\mathbf{r})\rangle$, and the eigenvalues satisfying Eq. 2.8 are $E_a = \hbar\omega_a$ and $E_b = \hbar\omega_b$. We assume that $\omega_b > \omega_a$, i.e. state $|\psi_b(\mathbf{r})\rangle$ is a higher energy state than state $|\psi_a(\mathbf{r})\rangle$, and that the states have opposite parity, so E1 interactions are allowed.

Since shifting the origin of the energy levels does not affect the eigenfunctions, we can lower the origin of zero energy by $\frac{1}{2}(\omega_b + \omega_a)$, so that $E_a \rightarrow E_a - \frac{1}{2}(\omega_b + \omega_a) = -\frac{1}{2}\omega_o$ and $E_b \rightarrow E_b - \frac{1}{2}(\omega_b + \omega_a) = \frac{1}{2}\omega_o$. The general time-dependent state $\Psi(\mathbf{r}, t)$ of the entire system is a linear combination of all the possible time-dependent states,

$$|\Psi(\mathbf{r}, t)\rangle = c_a(t)e^{i\omega_o t/2} |\psi_a(\mathbf{r})\rangle + c_b(t)e^{-i\omega_o t/2} |\psi_b(\mathbf{r})\rangle \rightarrow \begin{pmatrix} c_a(t)e^{i\omega_o t/2} \\ c_b(t)e^{-i\omega_o t/2} \end{pmatrix}. \quad (2.52)$$

where c_a and c_b are linear expansion coefficients that relate to observables, such as population, and are in general time-dependent.

When we have an ensemble of atoms, we are interested in the probabilities of the populations and coherences of the system as a whole, instead of wave functions. We introduce the density operator,

$$\hat{\rho}(t) = \sum_{nm} c_n(t)c_m^*(t) |\psi_n\rangle \langle\psi_m| = \sum_{nm} \rho_{nm} |\psi_n\rangle \langle\psi_m|, \quad (2.53)$$

which is a collection of the amplitudes of the states of interest. For the two-level system, the matrix representation of the density operator in the atomic basis $|\psi_a\rangle, |\psi_b\rangle$ is

$$\hat{\rho} = \begin{pmatrix} |c_a|^2 & c_1 c_2^* \\ c_1^* c_2 & |c_b|^2 \end{pmatrix}. \quad (2.54)$$

The diagonal elements ρ_{ii} represent the probability of occupying a state $|\psi_i\rangle$ and is related to the population of a state, while the off-diagonal elements ρ_{ij} represent the coherences between the states $|\psi_i\rangle$ and $|\psi_j\rangle$ and provide information on how much superposition there is in the state $|\Psi\rangle$. For a two-level system, the normalization of the density matrix imposes the condition $\rho_{11} + \rho_{22} = 1$. If the coherences are non-zero, then the system exhibits an electronic dipole moment. The evolution of the density matrix can be calculated from the following equation

$$i\hbar \frac{\partial \hat{\rho}}{\partial t} = [\hat{H}, \hat{\rho}], \quad (2.55)$$

which is known as Liouville's equation and can be derived from Schrödinger's equation.

For this two-level system, the atomic Hamiltonian is

$$\hat{H}_{\text{at}} = \frac{\hbar\omega_o}{2} \begin{pmatrix} -1 & 0 \\ 0 & 1 \end{pmatrix}, \quad (2.56)$$

From Eq. 2.39, the interaction Hamiltonian for this system is

$$\hat{H}_{\text{E1}} = -\hbar \begin{pmatrix} \langle \psi_a | \hat{H}_{\text{E1}} | \psi_a \rangle & \langle \psi_b | \hat{H}_{\text{E1}} | \psi_a \rangle \\ \langle \psi_a | \hat{H}_{\text{E1}} | \psi_b \rangle & \langle \psi_a | \hat{H}_{\text{E1}} | \psi_b \rangle \end{pmatrix} = -\hbar \begin{pmatrix} 0 & \Omega_R \cos \omega t \\ \Omega_R \cos \omega t & 0 \end{pmatrix}, \quad (2.57)$$

where $\Omega_R = \langle \psi_b | e\mathbf{r} \cdot \mathbf{E}_o | \psi_a \rangle / \hbar$ is called the Rabi frequency and is assumed to be real, $\Omega_R = \Omega_R^*$. Since the electric-dipole Hamiltonian does not couple the same state to itself, $\langle \psi_a | \hat{H}_{\text{E1}} | \psi_a \rangle = \langle \psi_b | \hat{H}_{\text{E1}} | \psi_b \rangle = 0$, meaning that there is no permanent dipole moment in an atom.

The electromagnetic field drives the system at frequency ω , which is usually of high-frequency in the 10^{12} Hz regime. To uncover the slower processes of the system, we will move into the frame that rotates at the laser frequency. Obtaining the Hamiltonian in the rotating basis requires applying a unitary transformation operator \hat{U} , such that

$$\hat{H} = \hat{U}^{-1} \hat{H} \hat{U} + i\hbar \left(\frac{d}{dt} \hat{U}^{-1} \right) \hat{U}. \quad (2.58)$$

For this two-level system, we apply the following transformation operator

$$\hat{U} = \begin{pmatrix} e^{i\omega t/2} & 0 \\ 0 & e^{-i\omega t/2} \end{pmatrix}. \quad (2.59)$$

The transformation $\hat{U}^{-1}\hat{H}\hat{U}$ does not change the atomic Hamiltonian, however, if Ω_R were not real, there will be a phase shift in c_a and c_b , which would present itself in the atomic Hamiltonian [Eq. 2.56]. A different transformation would then be necessary to eliminate the phase shift.

After the transformation, the E1 Hamiltonian becomes

$$\hat{U}^{-1}\hat{H}_{\text{E1}}\hat{U} = \frac{\hbar\Omega_R}{2} \begin{pmatrix} 0 & e^{-2i\omega t} + 1 \\ e^{2i\omega t} + 1 & 0 \end{pmatrix}. \quad (2.60)$$

In the rotating-wave approximation, the terms that contain 2ω are discarded, as these terms are non-resonant with the atomic transition of interest. Doing so gives us the total Hamiltonian in the rotating frame

$$\hat{H} = -\frac{\hbar}{2}\{\delta\hat{\sigma}_z + \Omega_o\hat{\sigma}_x\} = -\frac{\hbar}{2}\mathbf{\Omega} \cdot \boldsymbol{\sigma}, \quad (2.61)$$

where $\mathbf{\Omega} = (\Omega_R, 0, \delta)^T$ is a vector that we will later see acts as a torque vector, $\boldsymbol{\sigma} = (\sigma_x, \sigma_y, \sigma_z)^T$ is a vector that has the Pauli spin matrices σ_x , σ_y , σ_z as its components, and $\delta = \omega_o - \omega$ is the laser detuning frequency. This Hamiltonian has no time-dependence, which is expected since we are in a frame that rotates at the frequency of the laser field. We write the rotating frame states by applying the inverse transformation to the state in the laboratory frame

$$\tilde{\Psi}(\mathbf{r}, t) = \hat{U}^{-1}\Psi(\mathbf{r}, t) = \begin{pmatrix} c_a(t) \\ c_b(t) \end{pmatrix} = \begin{pmatrix} \tilde{c}_a(t) \\ \tilde{c}_b(t) \end{pmatrix} \quad (2.62)$$

while the density operator in the rotating frame is given by

$$\hat{\rho} = \hat{U}^{-1}\hat{\rho}\hat{U}. \quad (2.63)$$

In the rotating frame, the solutions to the time-dependent Schrodinger equation with initial conditions $\tilde{c}_a(t=0) = 1$, $\tilde{c}_b(t=0) = 0$ are

$$\tilde{c}_a(t) = \cos \frac{\Omega t}{2} - \frac{i\delta}{\Omega} \sin \frac{\Omega t}{2} \quad (2.64a)$$

$$\tilde{c}_b(t) = -\frac{i\Omega_R}{\Omega} \sin \frac{\Omega t}{2}, \quad (2.64b)$$

where $\Omega = \sqrt{\Omega_R^2 + \delta^2}$ is the generalized Rabi-frequency. The dynamics of the system can also be analyzed in terms of population and coherence, by evaluating Liouville's equation and by substituting the results for \tilde{c}_a and \tilde{c}_b into the definitions of ρ_{nm} . The solutions can be re-written in terms of the Bloch vector

$$\mathbf{R} = \begin{pmatrix} R_x & R_y & R_z \end{pmatrix}^T = \begin{pmatrix} \tilde{\rho}_{ab} + \tilde{\rho}_{ba} \\ -i(\tilde{\rho}_{ab} - \tilde{\rho}_{ba}) \\ \tilde{\rho}_{aa} - \tilde{\rho}_{bb} \end{pmatrix}, \quad (2.65)$$

where the transverse components R_x and R_y describe the in- and out-of-phase coherence, while R_z describes the population difference between the two states. In terms of the Bloch vector and the Pauli spin vector, the density matrix for the two-level atom can be written as

$$\hat{\rho} = \frac{1}{2} \left(\hat{\mathbb{I}} + \mathbf{R} \cdot \hat{\boldsymbol{\sigma}} \right), \quad (2.66)$$

which converts the density matrix into a vector that lies on a three-dimensional sphere, called the Bloch sphere [Fig. 2.5]. The dynamics of the system can be better visualized by considering the equation of motion of the Bloch vector, which can be obtained by substituting Eqs. 2.66 and 2.61 into Liouville's equation and using the commutation relations for the Pauli spin matrices. This gives

$$\frac{d\mathbf{R}}{dt} = \mathbf{R} \times \boldsymbol{\Omega} = \begin{pmatrix} \delta R_y \\ -\delta R_x + \Omega_R R_z \\ -\Omega_o R_y \end{pmatrix}. \quad (2.67)$$

These equations constitute the ‘‘Bloch Equations’’ and describe the precession of the Bloch vector about the ‘‘torque’’ vector $\boldsymbol{\Omega} = (\Omega_R, 0, \delta)^T$ at angular frequency $|\boldsymbol{\Omega}| = \sqrt{\Omega_R^2 + \delta^2}$. The solutions to the equations of motion for the Bloch vector are

$$R_x(t) = \tilde{c}_a \tilde{c}_b^* + \tilde{c}_b \tilde{c}_a^* = \frac{\delta \Omega_R}{\Omega^2} (1 - \cos \Omega t) \quad (2.68a)$$

$$R_y(t) = -i(\tilde{c}_a \tilde{c}_b^* - \tilde{c}_b \tilde{c}_a^*) = \frac{\Omega_r}{\Omega} \sin \Omega t \quad (2.68b)$$

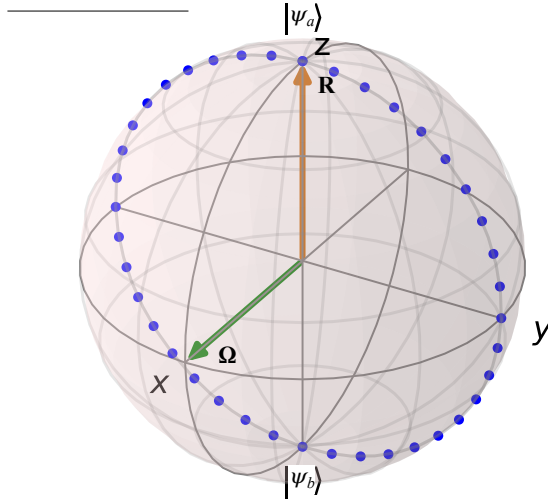


Figure 2.5: The Bloch vector lies on the Bloch sphere and precesses about the torque vector $\mathbf{\Omega}$, shown here to lie along the x -axis in the case where $\delta = 0$. The blue dots trace out the trajectory of the Bloch vector, which oscillates between the two states $|\psi_a\rangle$ and $|\psi_b\rangle$.

$$R_z(t) = |\tilde{c}_a|^2 - |\tilde{c}_b|^2 = 1 - \frac{\Omega_R^2}{\Omega^2}(1 - \cos \Omega t). \quad (2.68c)$$

The time evolution depends on the generalized Rabi frequency Ω and the field detuning from resonance δ . We can visualize the Bloch vector on the Bloch sphere, where every point on the surface of the sphere represents a possible state $|\tilde{\psi}\rangle = c_a |\tilde{\psi}_a\rangle + c_b |\tilde{\psi}_b\rangle$. The north pole of the sphere represents the pure state $|\tilde{\psi}_a\rangle$ while south pole represents the pure state $|\tilde{\psi}_b\rangle$. Physically, the radiation field “pumps” the atoms out of the ground state, polarizing the ensemble. A polarized ensemble can be described by a single wave function, and for a two-level system, there exists a fixed phase relationship between the two levels. For example, all points on the equator of the Bloch sphere correspond to states of equal superposition between $|\psi_a\rangle$ and $|\psi_b\rangle$, but with different phase ϕ , such that $|\tilde{\psi}\rangle = \frac{1}{\sqrt{2}}(|\tilde{\psi}_a\rangle + e^{i\phi}|\tilde{\psi}_b\rangle)$. In contrast, for a mixed state system, the atoms are in a disordered state, with no correlation existing between each of the individual wave functions.

In the case of zero detuning [$\delta = 0$], $\mathbf{\Omega}$ is aligned along the x -axis, and \mathbf{R} rotates about it at frequency Ω_R , corresponding to a situation where the state oscillates

between the two eigenstates, which can be seen by substituting Eq. 2.64 into the expression for the Bloch vector. This is called “Rabi flopping”.

2.6 Relaxation

In reality, atomic systems are subjected to random perturbations arising from interactions from the environment that can have a damping effect on coherence and population dynamics. These perturbations cause relaxation processes, such as spontaneous emission, a fully quantum mechanical process in which the atoms interact with the vacuum electromagnetic field modes [19]. We can account for relaxation by introducing phenomenological parameters into the Bloch equations. The first parameter is the decay rate, or the longitudinal relaxation term, Γ_1 , which describes the transfer of population from the excited state to the ground state,

$$\dot{\tilde{\rho}}_{11} = -\dot{\tilde{\rho}}_{22} = \Gamma_1 \tilde{\rho}_{22}. \quad (2.69)$$

The decay rate is inversely proportional to the lifetime τ_1 of the excited state. The lifetime, which denotes energy relaxation, is affected by spontaneous emission and interactions with the environment that may cause energy transfer to other atoms [20]. In terms of R_z ,

$$\dot{R}_z = \Gamma_1(1 - R_z). \quad (2.70)$$

The second parameter $\Gamma_2 = 1/\tau_2$ describes the decay of coherence due to spontaneous emission and other causes such as collisions and the Doppler effect. The transverse relaxation time τ_2 , which denotes phase relaxation, is the correlation time between the amplitudes \tilde{c}_a and \tilde{c}_b [21]. The effect of relaxation on the transverse components of the Bloch vector is

$$\dot{R}_x = -\Gamma_2 R_x \quad (2.71a)$$

$$\dot{R}_y = -\Gamma_2 R_y \quad (2.71b)$$

In free atoms, the phase relaxation rate is half the energy relaxation rate, $\Gamma_2 = \Gamma_1/2$ [$\tau_1 = 2\tau_2$]. The energy relaxation rate is due to spontaneous emission and

can be calculated by comparing Einstein's rate equations and the blackbody energy radiation formula, giving

$$\Gamma_1 = \frac{\omega^3 d_{ab}^2}{3\pi\epsilon_0 \hbar c^3}, \quad (2.72)$$

where $d_{ab} = \langle \psi_b | \mathbf{er} | \psi_a \rangle$. The polarization of the emitted light depends on the transition: if the transition has $\Delta m = +1$, then the emitted light is σ_- polarized, whereas if the transition has $\Delta m = -1$, then the emitted light is σ_+ polarized. If there is no change in angular momentum [$\Delta m = 0$], then the emitted light is linearly polarized. The ω^3 dependence originates from counting the modes available for the radiation. Low-frequency transitions are much less susceptible to spontaneous emission and can have a longer lifetime. For example, the hyperfine transitions in alkali metal, which correspond to microwave transitions, are much longer lived than the optical transitions. Atoms are also in constant collision with each other and the walls confining the gas, shortening their excited state and coherence lifetimes. These processes may be elastic, affecting only the phase relaxation and not the energy relaxation. In general, the decoherence time is shorter than the excited state lifetime, $\tau_2 \leq 2\tau_1$.

Relaxation can be accounted for by adding Eqs. 2.70 and 2.71 to the Bloch equations [Eq. 2.67], forming optical Bloch equations,

$$\frac{d\mathbf{R}}{dt} = \boldsymbol{\Omega} \times \mathbf{R} + \begin{pmatrix} -\Gamma_2 R_x \\ -\Gamma_2 R_y \\ \Gamma_1(1 - R_z) \end{pmatrix}. \quad (2.73)$$

In the Bloch sphere picture, relaxation causes the Bloch vector to shrink. The Bloch vector is no longer restricted to the surface of the Bloch sphere. As time goes on, the vector decays to the point $(0, 0, 0)$. The solution to the optical Bloch equations in steady state [$t = \infty$] is found by setting $\dot{\mathbf{R}} = 0$,

$$\mathbf{R}_\infty = \frac{1}{\frac{\Omega_R^2 \Gamma_2}{\Gamma_1} + \delta^2 + \Gamma_2^2} \begin{pmatrix} \Omega_R \delta \\ \Omega_R \Gamma_2 \\ \delta^2 + \Gamma_2^2 \end{pmatrix}. \quad (2.74)$$

2.6.1 Absorption

The amount of absorption of a propagating wave with angular frequency ω in a two-level ensemble can be obtained from the stationary solutions of the Bloch vector. The Beer-Lambert law relates the incident intensity I_o to the output intensity $I(z)$ in a medium of thickness z

$$I(z) = I_o e^{-\kappa(\omega)z}. \quad (2.75)$$

The absorption coefficient $\kappa(\omega)$ can be obtained from χ'' , the imaginary part of the susceptibility of the medium [see Appendix B.2],

$$\kappa(\omega) = \frac{\omega}{c} \chi''. \quad (2.76)$$

As previously mentioned in Section. 2.5.1, the two quadrature components of the coherence, $R_x + iR_y$, gives the complex susceptibility of the medium [20], which is equal to [see Appendix B.1 for derivation]

$$\chi = \chi' - i\chi'' = n \frac{d_{ab}^2}{3\epsilon_o \hbar} \left(\frac{\delta + i\Gamma_2}{\frac{\Omega_R^2 \Gamma_2}{\Gamma_1} + \delta^2 + \Gamma_2^2} \right), \quad (2.77)$$

where n is the density of the medium. Thus, for a two-level system, the absorption coefficient is

$$\kappa(\omega) = \frac{\omega}{c} \text{Im}\{\chi\} = \frac{N\omega}{Vc} \frac{d_{ab}^2}{3\epsilon_o \hbar} \left(\frac{\Gamma_2}{\frac{\Omega_R^2 \Gamma_2}{\Gamma_1} + \delta^2 + \Gamma_2^2} \right). \quad (2.78)$$

2.6.2 Weak Driving Intensity

When the driving intensity is weak $\Omega_R \leq \Gamma_1, \Gamma_2$, the first term in the denominator in Eqs. 2.78 and 2.77 can be neglected. In this regime, the susceptibility is linear in \mathbf{E}_o . The absorption coefficient as a function of the applied frequency has the form of Lorentzian:

$$\kappa(\omega) = \frac{N\omega}{Vc} \frac{d_{ab}^2}{3\hbar\epsilon_o} \left(\frac{\Gamma_2}{\delta^2 + \Gamma_2^2} \right). \quad (2.79)$$

The full-width at half maximum is $\Delta\omega_{1/2} = 2\Gamma_2$. Thus, the broadening of the absorption spectrum is determined by the transverse relaxation rate Γ_2 . If the finite

excited state lifetime $\tau = 1/\Gamma$ is the only factor contributing to the transverse relaxation rate, then this type of broadening is called natural line broadening. Natural line broadening can also be explained by the time-energy uncertainty principle:

$$\Delta E \Delta t \sim h. \quad (2.80)$$

Because of the uncertainty in the excited state lifetime, there is a range of possible frequencies $\Delta\omega \sim 1/(2\pi\Delta t)$ from the photon emitted as a result of spontaneous emission. The natural linewidth is generally small and is not often observed because other broadening factors, such as the Doppler shift, dominate [see Appendix C for more on other broadening factors]. For the D2 transition in ^{87}Rb , decay rate is $\Gamma = 38.11 \times 10^6 \text{ s}^{-1}$, giving a natural linewidth of $\Delta\omega = 2\pi \times 6.065 \text{ MHz}$ [17].

2.6.3 High Intensity Limit

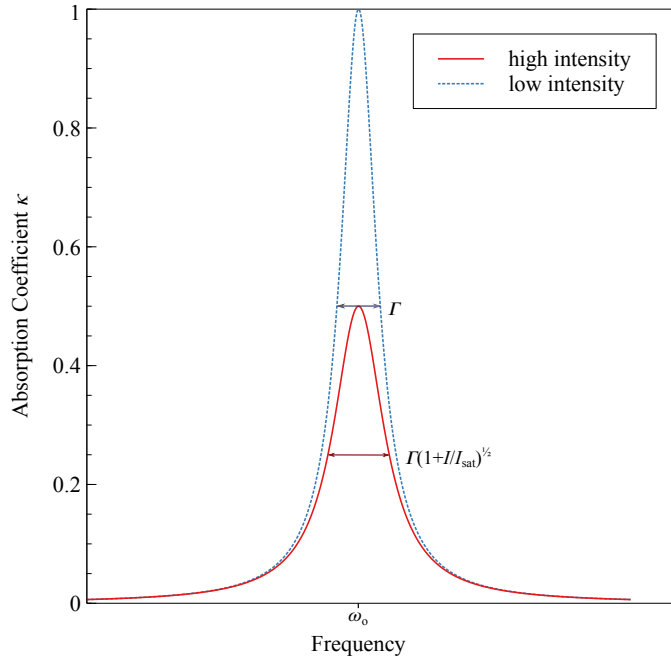


Figure 2.6: Absorption coefficient $\kappa(\omega)$ at high and low light intensities, in units of $N\sigma_o$, for $I_{\text{sat}} = I$. At high intensities, absorption is reduced and the full-width half maximum is broadened, compared to the situation at low intensities.

When the amplitude of the driving field is large, the Ω_R^2 term in the denominator

of Eq. 2.78 cannot be neglected, and the pumping process becomes nonlinear. Re-writing the absorption coefficient for free atoms in terms of the resonant scattering cross section $\sigma_o = 3\lambda^2/(2\pi)$ [see Eq. B.23 in Appendix B.2.1] gives us

$$\kappa(\omega) = \frac{N}{V} \sigma_o \frac{\Gamma_2^2}{\frac{\Omega_R^2}{2} + \delta^2 + \Gamma_2^2}. \quad (2.81)$$

We can show that in the high-intensity limit, the absorption is reduced by re-writing $\kappa(\omega)$ in terms of the saturation intensity $I_s(\omega)$, which is defined as

$$I_s(\omega) = \frac{\delta^2 + \Gamma_2^2}{6\pi c^2 \Gamma_2} \hbar \omega^3. \quad (2.82)$$

On resonance, $\delta = 0$, the saturation intensity is

$$I_{\text{sat}} = \frac{4\pi^2 \hbar c}{3\lambda^3} \Gamma_2, \quad (2.83)$$

which allows us to write

$$\frac{I}{I_s(\omega)} = \frac{I}{I_{\text{sat}}} \frac{\Gamma_2^2}{\delta^2 + \Gamma_2^2}. \quad (2.84)$$

Noting that the square of the Rabi frequency $\Omega_R^2 = d_{ab}^2 E_o^2$ can be written as [from Eq. B.22]

$$|\Omega_R|^2 = \frac{12\pi c^2}{\hbar \omega^3} \Gamma_2 I, \quad (2.85)$$

where $I = \epsilon_o c E_o^2 / 2$ is the intensity of the radiation field, the terms in Eq. 2.78 may be rearranged to give

$$\kappa(\omega) = \frac{N}{V} \frac{\Gamma_2^2}{\delta^2 + \Gamma_2^2 (1 + I/I_{\text{sat}})}, \quad (2.86)$$

which is a Lorentzian and has a full-width-half-maximum equal to

$$\Delta\omega = 2\Gamma_2 \sqrt{1 + \frac{I}{I_{\text{sat}}}}. \quad (2.87)$$

On resonance, the absorption coefficient is equal to $\kappa(\omega_o) = N\sigma_o/(1 + I/I_{\text{sat}})$, smaller than in the case of the low intensity limit where $\kappa(\omega_o) = N\sigma_o$. By comparing a plot of the high and low-intensity limit in Fig. 2.6, we can see that the absorption is reduced and the full-width at half-maximum is broadened. This phenomenon is called

“power broadening” or “saturated absorption”. Physically, this occurs because when Rabi frequency is greater than the spontaneous emission rate, there is no chance for the atoms in the excited state to undergo spontaneous emission and re-absorb the radiation.

2.7 Optical Pumping

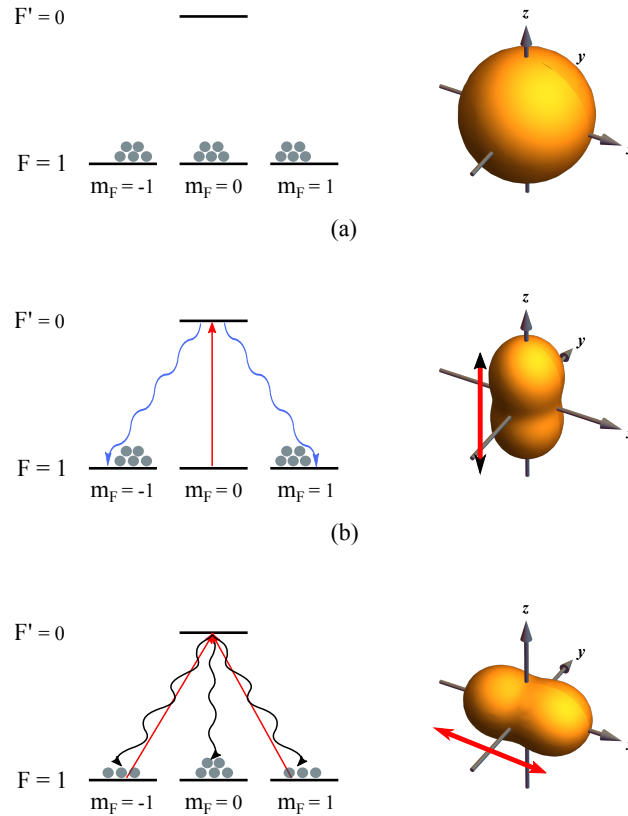


Figure 2.7: A three level ground-state system with one excited state that is (a) unpolarized and absent of light interactions, (b) optically pumped by light linearly polarized along z , and (c) optically pumped by light linearly polarized along x . The angular momentum probability surfaces are shown on the right and the light propagates along y . Asymmetry in the AMPS indicates that there is anisotropy in the system.

Optical pumping is a process in which atoms are pumped out of an energy level into high energy level[s] by the use of polarized light at the proper frequency. Ideally, atoms are brought from a disordered state into a polarized, ordered state where the

internal states of the atoms are identical due to the interaction with the light. We will use the terminology "atomic polarization" to refer to a state where the atoms in an ensemble are a preferred angular momentum state, to avoid confusion with the electromagnetic field polarization, which specifies the geometric orientation of the wave oscillations. We will discuss optical pumping in the context of a system with excited state $F' = 0$ and ground states $|F = 1, m_F = 0, \pm 1\rangle$.

For an unpolarized atomic ensemble, the three Zeeman ground states have equal populations, and no coherence exists. This means that if we measure the angular momentum along any axis, the result would be the same, as the system overall is not in a preferred angular momentum state. The density matrix for such a system in the basis $|m_F = 1\rangle, |m_F = 0\rangle, |m_F = -1\rangle$

$$\rho = \begin{pmatrix} 1/3 & 0 & 0 \\ 0 & 1/3 & 0 \\ 0 & 0 & 1/3 \end{pmatrix}, \quad (2.88)$$

which we can visualize by plotting the angular momentum probability surface [AMPS] for the density matrix, as in Fig. 2.7(a). The surface gives the probability of finding the maximum projection along the (θ, ϕ) direction. More details can be found in [14]; we will only briefly present the mathematical formulation here. Suppose we measure the projection of the angular momentum of a system with total angular momentum F along some axis: the possible outcomes are $-F, -F + 1, \dots, F$. The probability of measuring a given value m along the quantization axis is $\rho_{mm} = \langle F, m | \rho | F, m \rangle$ and the probability of maximum possible projection $m = F$ is $\rho_{FF} = \langle F, F | \rho | F, F \rangle$. We will use this maximum possible projection probability to characterize the atomic polarization state along the quantization axis. Along an arbitrary (θ, ϕ) direction, ρ_{FF} is given by

$$\rho_{FF}(\theta, \phi) = \langle FF(\theta, \phi) | \rho | FF(\theta, \phi) \rangle \quad (2.89)$$

$$= \sum_{mm'} D_{mF}^{(F)*}(\phi, \theta, 0) \rho_{mm'} D_{m'F}^{(F)*}(\phi, \theta, 0), \quad (2.90)$$

where the Wigner- D functions are

$$D_{mF}^{(F)}(\phi, \theta, 0) = e^{-i(\phi m')} d_{m'm}^{(F)}(\theta) \quad (2.91)$$

and $d_{m'm}^{(F)}(\theta)$ is the matrix of rotations about the y -axis. The Wigner formula for $d_{m'm}^{(F)}(\theta)$ is

$$d_{m'm}^{(F)}(\theta) \sum_k (-1)^{k-m+m'} \frac{(F+m)!(F-m)!(F+m')!(F-m')!}{F+m-k)!k!(F-k-m')!(k-m+m')!}, \quad (2.92)$$

where the sum runs over values of k for which none of the arguments of the factorials are negative. In this case, the probability distribution is a sphere with a radius of $1/3$. The results were calculated and plotted in *Mathematica* [22]. In Fig. 2.7(a), we plot the probability surface for the unpolarized ensemble under consideration. The shape is hollow inside and the volume of the shape is generally different between atomic polarization states of the same ensemble, even if we have the same amount of atoms. One of the purposes of visualizing the surface is to show the rotational symmetry properties of the density matrix, which determines the kind of optical anisotropy a system can have. There is no preferred direction for an unpolarized atomic ensemble because the states have equal population. Moreover, optical properties such as the absorption coefficient and the refractive index are independent of the light polarization. If the system has k -fold symmetry about the quantization axis, then coherences exist between states only for which $|\Delta m| = k$.

Now, suppose that we apply a beam linearly polarized along z to the unpolarized ensemble. Because of the selection rule $\Delta m_F = 0$, only atoms in $m_F = 0$ are excited to $m_{F'} = 0$, and then decay with equal probability into all three sublevels. After enough absorption cycles, the population in $m_F = 0$ is eventually depleted, filling the states $m_F = \pm 1$, which become non-absorbing dark states as they do not interact with the beam. The density matrix in this case is

$$\rho = \begin{pmatrix} 1/2 & 0 & 0 \\ 0 & 0 & 0 \\ 0 & 0 & 1/2 \end{pmatrix}, \quad (2.93)$$

and is plotted in Fig. 2.7(b). The distribution is peanut-shaped and is aligned along z , as there is a high probability of measuring maximum angular momentum in that direction. The rotational symmetry about z indicates that the density matrix has no coherence. When the distribution is asymmetric, absorption depends on the direction of the field. Here, the vapor will tend to transmit light linearly polarized along z while absorbing orthogonally polarized light, since, in the spherical basis, linearly polarized light is an equal superposition of left and right circularly polarized light.

The same analysis can be applied for optical pumping by linearly polarized light along x . To find the density matrix, we can rotate the coordinate system about y by $\pi/2$, taking z into x . The density matrix transformation is

$$\rho' = D(0, \pi/2, 0)\rho D(0, \pi/2, 0)^\dagger, \quad (2.94)$$

where

$$D(\alpha, \beta, \gamma) = e^{-i\hat{J}_z\alpha/\hbar}e^{-i\hat{J}_y\beta/\hbar}e^{-i\hat{J}_x\gamma/\hbar} \quad (2.95)$$

is the rotation operator and \hat{J}_i , $i = x, y, z$ are the angular momentum spin operators. The result is [14]

$$\rho = \begin{pmatrix} 1/4 & 0 & 1/4 \\ 0 & 1/2 & 0 \\ 1/4 & 0 & 1/4 \end{pmatrix}, \quad (2.96)$$

which is plotted in Fig. 2.7(c). The peanut shape is now aligned along x , and preferentially transmits light linearly polarized along this axis. There is $k = 2$ fold symmetry about z , which correspond to the $\Delta m = 2$ coherences. From the density matrix, we can see that there is a coherent superposition between the $m_F = \pm 1$ sublevels and the population in the $m_F = \pm 1$ states are not all absorbing atoms; some of the atoms in $m_F = 0$ are in a dark state. The state with equal superposition between the $m_F = \pm 1$ sublevels with the same phase is also a dark state [14].

To summarize, optical pumping creates ground state atomic polarization, caused by population imbalance or existence of coherence between the ground states, changing

the optical properties of the medium which depend on the characteristics of the light field [14]. In practice, however, relaxation processes such as collisions can redistribute the atoms between ground states.

Chapter 3

Magnetometry with MAOP

We present in this chapter a vector magnetometry experiment with rubidium vapor inside a microwave cavity resonator. Our method is based on measuring the frequency and amplitude differences of microwave-assisted optical pumping [MAOP] curves for different magnetic-dipole transitions. First, we give a brief overview of general magnetometry based on optical pumping and discuss zero-field magnetometers. Second, our experimental setup is described Section 3.2. We then discuss microwave-optical double resonance, provide a theoretical model, and then explain how we use the double resonance spectrum for vector magnetometry. Finally, we present some preliminary data. These results motivate the micro-fabrication of rubidium vapor cells for magnetometry, which is presented in the following chapter.

3.1 Alkali Vapor Magnetometers

Alkali vapor cell magnetometers use the coherent precession of atomic spins to detect and measure magnetic fields [23]. By observing the resonance frequency of the Larmor precession due to the magnetic field, we can measure the magnetic field amplitude. Alkali atoms-based magnetometers have come to rival SQUID-based magnetometers in terms of sensitivity, which is the smallest change in magnetic field a sensor can discern, usually given in units of $\text{T}/\sqrt{\text{Hz}}$. Alkali magnetometers have been able to achieve $\text{fT}/\sqrt{\text{Hz}}$ sensitivities at low bandwidths, and $\text{nT}/\sqrt{\text{Hz}}$ at higher bandwidths

of 100 Hz [24]. The sensitivity depends on the polarization lifetime of the spins, reduced by wall collisions and other relaxation effects. The polarization lifetime is maximized by using high-pressure buffer gases in the vapor to inhibit diffusion and/or by using anti-relaxation coatings on the cell walls [see Section 4.6.3]. Because all of the types of alkali atoms have different excited-state lifetimes, sensors made with one type of alkali atoms will have a different sensitivity compared to sensors made with another kind of alkali atom. Which type of atoms are best depends on the application's needs.

3.1.1 General Magnetometry

As previously discussed in Section 2.7, optical pumping can give rise to Zeeman coherences, which creates anisotropy in the angular momentum distribution, polarizing the atomic spins in the direction of the beam. For example, for the $F = 1 \rightarrow F' = 0$ transition, light linearly polarized along x creates coherence between the ground states $m = \pm 1$ with a momentum distribution symmetric about x . Application of a static magnetic field transverse to the pump field, shown in Fig. 3.1(b) causes the atomic density matrix to evolve, which manifests as a rotation of the atomic polarization about the magnetic field axis at a rate equal to the Larmor frequency. The transverse magnetic field reduces the efficiency of the optical pumping. In the Bloch vector picture, the magnetic field vector acts as the torque vector Ω about which the atomic polarization vector precesses.

Simultaneous to pumping and precession is relaxation; all three effects generate a net anisotropy that causes circular birefringence, where the circular components of the linearly polarized field see different indices of refraction. These components transmit through the medium at different speeds, causing a phase difference to build up, resulting in a polarization rotation of the electric field at an angle θ ; this effect is called nonlinear Faraday rotation or nonlinear magneto-optic rotation [NMOR] [25]. In this case, the NMOR effect is due to Zeeman coherences. One method of detecting

the rotation angle is by using balanced polarimetry, where we measure the difference between the intensities of x and y component of the transmitted field, $I_x - I_y$, which is proportional to θ for small-angle rotations [Fig. 3.1(d)].

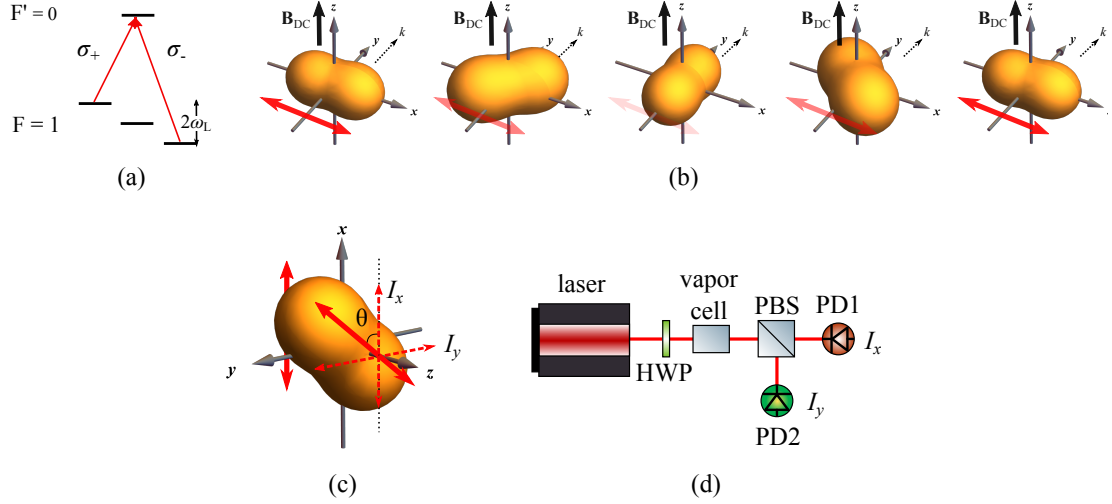


Figure 3.1: (a) Energy level diagram for optical pumping schematic with linearly polarized light along x [red arrows]. (a) Presence of transverse static magnetic field \mathbf{B}_{DC} causes the atomic polarization of the ensemble to precess about the magnetic field axis, z . (b) When pumping is synchronized with the Larmor frequency ω_L , the anisotropy axes of the atoms pumped at different times are aligned, generating a macroscopic dynamic polarization. Here, we show amplitude-modulated light, the time-dependence of the beam intensity is illustrated by different shading of the double-headed red arrows. The k direction indicated by the dotted black arrow along y indicates the propagation direction of the beam. Adapted from [25]. (c) Anisotropy causes circular birefringence, in which left and right hand circularly polarized light travel at different speeds in the medium. Linearly polarized light is rotated about the precession axis by an amount θ . (d) Balanced polarimetry setup for detecting Faraday rotation. A half-wave plate [HWP] rotates the plane of polarization of the beam at 45° with respect to the polarizing beam splitter [PBS]. Two photodetectors PD1 and PD2 detect the x - and y -components, respectively, of the intensity of the laser field.

Because of the simultaneous pumping and rotation of the anisotropy axis, atoms with all spatial orientations exist. To generate a macroscopic atomic polarization, we can use synchronous pumping, where we modulate the pumping frequency ω_P so that it coincides with ω_L . In the amplitude modulation scheme, light is on when the anisotropy axis is parallel to the polarization direction of the field, and light is

attenuated when the anisotropy axis is perpendicular to the field. The amplitude of the signal is maximized when $\omega_P = 2\omega_L$ because the atomic polarization surface is the same when it is oriented at 0° and 180° . By extracting Larmor frequency, we can determine the strength of the magnetic field.

This type of effect, where the component of the magnetic field vector that is transverse to the pumping direction is measured by probing the atomic polarization transverse to the electric field polarization, is known as the Hanle effect [26]. In the setup described above, if the transmission of an unmodulated pump beam is measured as a function of the magnitude of the transverse magnetic field, then we will obtain a Lorentzian curve that is symmetric about $|\mathbf{B}_{DC}| = 0$.

3.1.2 Zero-Field Magnetometers

Atomic zero-field magnetometers operate near the zero-field regime [nT scale] and are highly sensitive, requiring magnetic shielding and additional coils to cancel the ambient field. Their operation is based on the ground-state Hanle effect. The magnetometer can be made selectively sensitive to a component of the magnetic field vector [27, 28] by modulating one or several components of an external AC magnetic field. These types of magnetometers are classified as vector magnetometers. A sub-class of zero-field magnetometers are spin-exchange relaxation-free [SERF] magnetometers. In low magnetic fields, the dominant relaxation is due to the spin-exchange mechanism, which, counter-intuitively, can be suppressed by increasing the spin-exchange collision rate [23]. When this collision rate is high, the atomic spins are more likely to precess in phase and maintain their polarization longer, giving a better optical signal. The collision rate can be increased by increasing the temperature of the atomic vapor, which increases the density and hence the frequency of collisions. SERF magnetometers, which typically have sensitivities in the $\text{fT}/\sqrt{\text{Hz}}$ regime, are used to measure biomagnetism, such as for fetal magnetocardiography [28] and magnetoencephalography [29], however, their fundamental sensitivity limits have not yet been attained,

which is on the $\text{aT}/\sqrt{\text{Hz}}$ scale [30]. Miniaturization and portability are also important for magnetoencephalography. There is considerable research on chip-scale SERF magnetometers based on MEMS technology [31], which motivates our research on micro-fabricating Rb vapor cells.

3.2 Experimental Setup

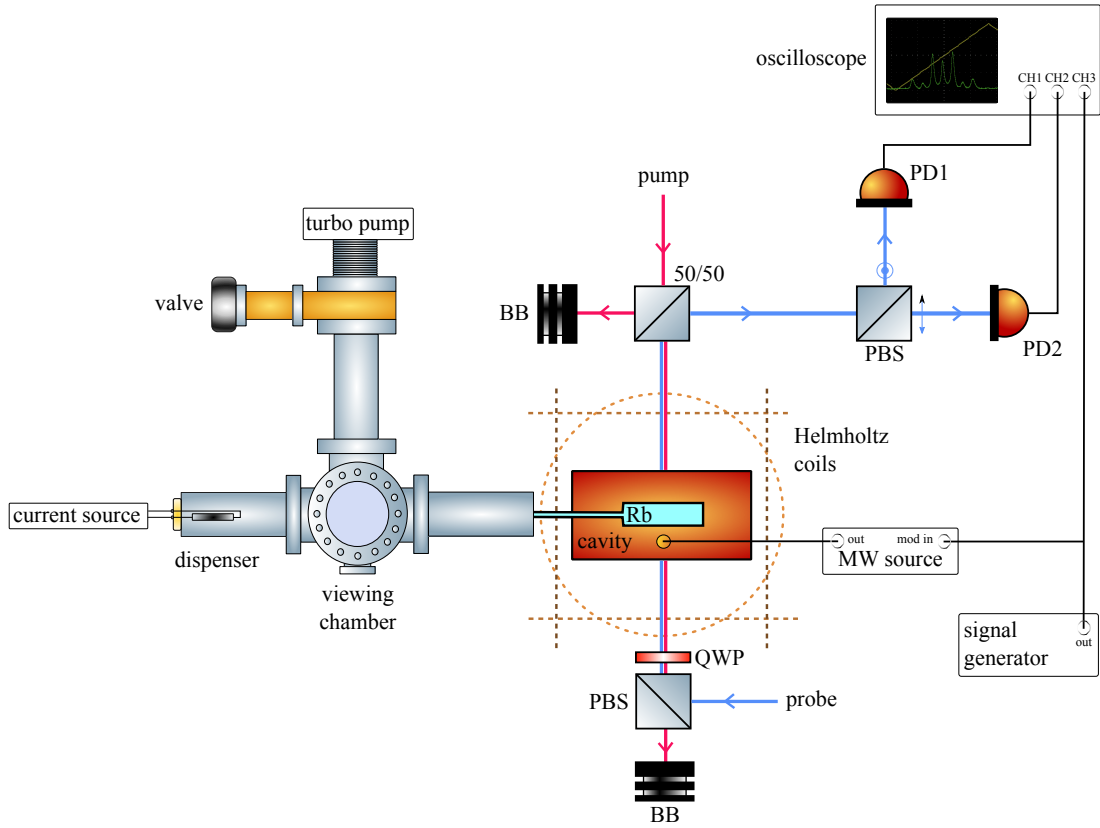


Figure 3.2: Experimental setup of the microwave vector magnetometry experiment. Abbreviations: beam blocker [BB], polarizing beam splitter [PBS], 50/50 beamsplitter [50/50], quarter-wave plate [QWP], photodetector [PD].

Before discussing the theoretical concepts of our experiment, we first describe the setup. The schematic is shown in Fig. 3.2.

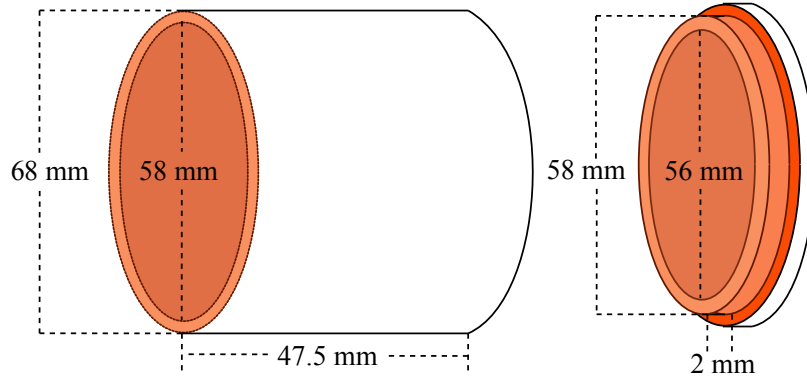


Figure 3.3: Schematic of microwave cavity geometry [not to scale]. Right: main cavity body made of polished copper. White indicates the outer surface of the cavity. Left: cavity end cap. A 2-by-2 mm ring on the end cap splits the modes of the cavity. There are two end caps, only one is shown.

3.2.1 Microwave Cavity

A rubidium vapor glass cell was placed at the center of a high-quality tunable cylindrical microwave copper cavity [5]. The cavity was designed and fabricated by Clinton Potts. Because of the high-quality factor of $Q = 27,000$ at room temperature, only frequencies close to the resonance frequency are enhanced, while frequencies that further away are suppressed [32]. The outer diameter of the cavity is 68 mm, while the inner diameter is 58 mm [Fig. 3.3]. The main body of the cavity has a length of 47.5 mm. The microwave cavity was specifically designed to work so that for the dimensions of our vapor cell, in the TE_{011} mode, the resonance frequency, which depends on the ratio of the cavity diameter and the cavity length, is equal to the ground-state hyperfine splitting frequency of ^{87}Rb . The fields of the TE_{011} modes for a perfect cylinder are, in spherical coordinates (ρ, ϕ, z) , [33]

$$B_z = B_o J_0\left(\frac{p_{11}\rho}{a}\right) \sin \frac{\pi z}{d} \quad (3.1a)$$

$$B_\rho = \frac{\beta a}{p_{11}} B_o J_1\left(\frac{p_{11}\rho}{a}\right) \cos \frac{\pi z}{d} \quad (3.1b)$$

$$E_\phi = \frac{ik\eta a}{p_{11}} \frac{B_o}{\mu} J_1\left(\frac{p_{11}\rho}{a}\right) \sin \frac{\pi z}{d}, \quad (3.1c)$$

where p_{nm} is the m^{th} zero of the $J_n(x)$ Bessel functions [$p_{11} \approx 3.83$], H_o is the amplitude of the microwave field, a is the radius of the cavity, d is the cavity length, $\beta = \sqrt{k^2 - (p_{11}/a)^2}$ is the propagation constant, $k = \omega\sqrt{\mu\epsilon}$ is the wavenumber in the medium filling the cavity, and $\eta = \sqrt{\mu/\epsilon}$, where μ and ϵ are the permeability and permittivity, respectively, of the filling medium. The microwave magnetic field in the TE_{011} mode is localized at the center of the cavity, where the vapor cell is located, and points along the cavity axis [Fig. 2.4, green arrow]. The TE_{011} mode is degenerate with the TM_{111} mode [34], so a 2-by-2 mm ring on the end cap of the cavity separated the modes by geometrical perturbation. The microwave cavity can be tuned by adjusting the position of its end cap, which changes the ratio of the cavity length to cavity diameter and thus the resonance frequency. Two holes were drilled on opposite sides of the body, allowing light to pass through the cavity and the cell for atomic interrogation.

3.2.2 Microwave Source

The microwave signal derived from a microwave source was externally frequency-modulated [1 MHz depth] by a signal generator with a ramp function [100 Hz, 1 VPP] to generate a range of microwave frequencies -1 MHz to +1 MHz detuned from the ground state hyperfine transition frequency. The signal was delivered to the cavity by an SMA pin coupler. We set the microwave power to -10 dBm.

3.2.3 Rubidium Dispensing System

The stem of the vapor cell was unsealed and connected to a vacuum system, where rubidium gas, evaporated from a dispenser housed inside the vacuum system and heated by a current source, flowed in. 5A of current was usually sufficient to observe fluorescence inside the viewing chamber. However, higher currents were required a few days after replacing the dispenser, which we later found out was due to a leak. A vacuum turbopump was connected to the system and a valve allowed us to open or

seal the system from the atmosphere; it was open when the turbopump was running. We heated the system to temperatures above 50 °C [the heater is not shown] by current flow. A digital temperature meter and a thermocouple monitored the system temperature.

3.2.4 Helmholtz Coils

A set of three-axis Helmholtz coils placed around the cavity allowed us to apply a static field along, vertical to, and horizontally transverse to the cavity axis, as represented by the dotted lines in Fig. 3.2. The direction of the DC field, \mathbf{B}_{DC} defines the quantization axis to which we reference the microwave field alignment.

3.2.5 Optical Setup

We used circularly polarized light tuned to the $F = 1 \rightarrow F' = 0$ D2 transition to probe the rubidium atoms and linearly polarized light tuned to the $F = 2 \rightarrow F' = 2$ D2 transition to pump the atoms. Here, F [without the prime] denotes the hyperfine ground state where $\ell = 0$, while F' denotes the excited hyperfine states where $\ell = 1$. The laser setup was part of the hybrid quantum systems project. The probe and the pump light counter propagate through the cell. A quarter-wave plate [QWP] placed at the entrance of the cavity generates circularly polarized probe light. After exiting the cavity, part of the probe beam reflected off a 50/50 beamsplitter [50/50], transmitted 50% of the light towards to polarizing beamsplitter [PBS]. The PBS separates the horizontal and vertical components of the beam, which are transmitted and reflected into two photodetectors [PD1, PD2]. Both photodetectors were connected to the oscilloscope to view and collect the transmission signals. Note that we define the light polarization relative to its propagation direction \mathbf{k} , while the microwave direction is defined relative to the applied static magnetic field.

3.3 Microwave-Optical Double Resonance

In the presence of a low-strength DC magnetic field, the Zeeman sublevels are shifted by an amount $\hbar\omega_L$ from each other, where ω_L is the Larmor frequency. Through optical pumping, the populations of atomic energy levels can be selectively altered. Despite the terminology, pumping can also be done with microwave magnetic fields to alter the Zeeman sublevel populations. In our experiment, a microwave field resonantly pumps atoms from the $|F = 1, m_1\rangle$ ground-state to the $|F = 2, m_2\rangle$ ground state, which subsequently decays with equal probability into all the Zeeman sublevels in $F = 1$. Eventually, the m_1 sublevel will be depleted. For example, a left circularly polarized microwave field of frequency $\omega_o - 3\omega_L$ can induce transition (i) [the other nine transitions are shown in Fig. 2.2], as shown schematically in Fig. 3.4(b). Atoms pumped out of $m_1 = -1$ redistribute themselves into $m_1 = 0, 1$.

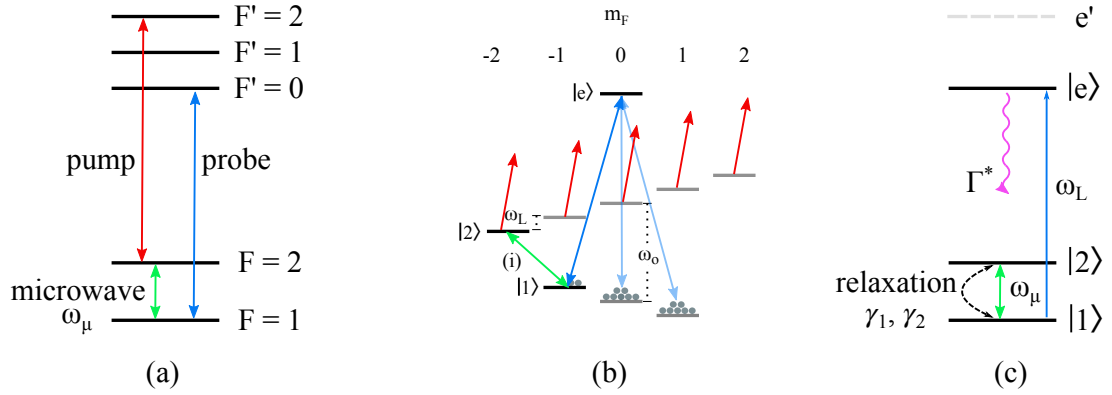


Figure 3.4: (a) Energy level diagram showing our microwave-optical double resonance setup. A strong pump beam [red arrow] connects $F = 2$ to $F' = 2$, while a probe beam [blue arrow] is tuned to the $F = 1 \rightarrow F' = 0$ transition. A microwave field [green arrow] of frequency ω_μ pumps atoms between $|1\rangle = |F = 1, m_1\rangle$ and $|2\rangle = |F = 2, m_2\rangle$. (b) In the presence of a static magnetic field, there is hyperfine splitting and adjacent m_F sublevels within the same hyperfine state F are split by an amount proportional to ω_L . When the microwave field frequency is equal to $\omega_o - 3\omega_L$, atoms are pumped out of $m_1 = -1$. The pump removes atoms from $F = 2$ while the probe measures the population in $F = 2$. (c) Three level approximation used in our theoretical model. We ignore the pump by treating the removal of atoms from $|F' = 2\rangle$ as a transverse relaxation represented by γ_2 .

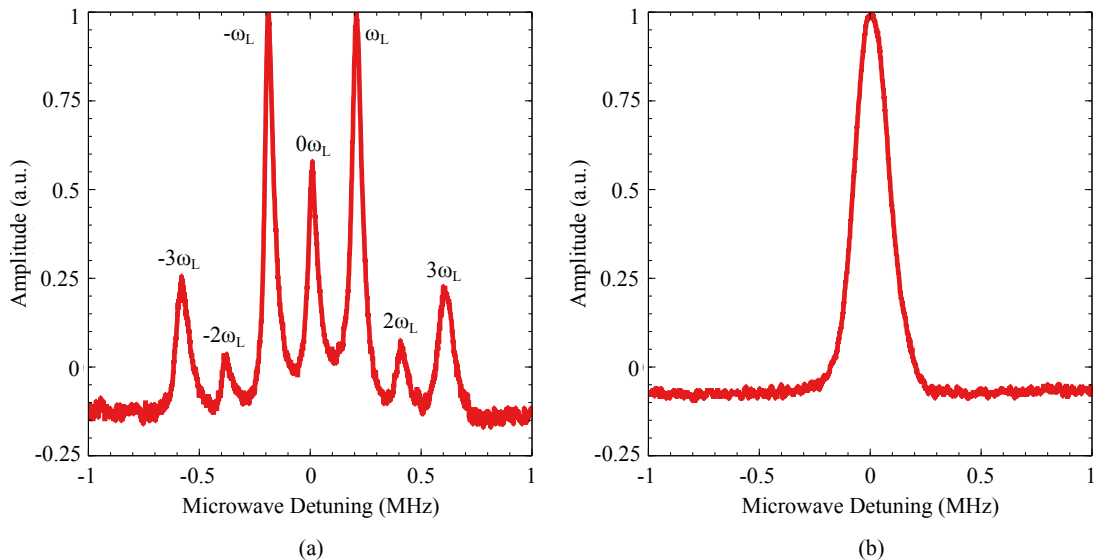


Figure 3.5: MAOP spectra in the presence of (a) Earth’s magnetic field, which causes Zeeman splitting of the hyperfine levels, and (b) zero field. The fields were zeroed by applying magnetic fields in the direction opposite to the ambient field using Helmholtz coils. The amplitudes have been normalized such that the maximum amplitude is 1. The data shown are from one of the photodetectors.

Figure 3.4(a) shows the pumping scheme. We apply a strong beam, the “pump”, tuned to the $F = 2$ to $F' = 2$ transition, to atoms in the $F = 1$ states, since atoms will decay from $F' = 2$ to either $F = 2$ or $F = 1$. Atoms in the $F = 1$ sublevels are then redistributed by the microwave field, emptying $m_F = -1$. The population in the lower state can be probed by another electromagnetic field. In our experiment, we apply a weak laser beam, the “probe”, tuned to the optical $F = 1 \rightarrow F' = 0$ transition and measure its transmission through the atomic gas. The probe field has a spectrum that is broad enough to cover the possible splitting of each hyperfine level caused by an applied magnetic field but is much narrower than that of the ground-state hyperfine splitting. When the two fields, laser, and microwave, are simultaneously resonant with their respective transitions, the situation is called “double resonance” [DR] [35]. Specifically, in our case, we have a microwave-optical double resonance. Through a measurement of transmission, the probe beam measures the population of atoms in the $F = 1$ sublevels, allowing us to resolve each of the hyperfine transitions.

Ideally, most of the probe light will be transmitted as there are no absorbing atoms in $m_1 = -1$. The probe beam power was on the order of tens of μW while the pump beam was 1-2 mW. If either beam power is too high, then we get saturation, and the DR signal disappears. The absorption cross-section is on the order of 10^{-15} m^{-3} .

When the microwave field has both parallel and perpendicular components with respect to \mathbf{B}_{DC} and is swept through the frequency range covering $\omega_o \pm 3\omega_L$, a measurement of the probe transmission as a function of microwave frequency would give us seven curves corresponding to 3 π -transitions and 6 σ_{\pm} transitions, two of which are degenerate [Fig. 3.5(a)]. The peaks are shifted from the center by an amount proportional to their Zeeman shifts. Therefore, measuring the frequency shifts of the transitions provides a method for scalar magnetometry. The linewidth is determined by the quality factor of the microwave cavity, which acts as an amplifier, as well as the sweep rate of the microwave source. A smaller linewidth indicates less loss of photons, although a misaligned cavity will also give us sharper, but asymmetric peaks.

When the microwave field is parallel to the direction of the static magnetic field [π -polarization], three peaks are observed [Fig. 3.6(a)]. When the field is perpendicular to \mathbf{B}_{DC} [σ -polarization], four peaks are observed [Fig. 3.6(b)]. The presence of a peak at the center of Fig. 3.6(b) indicates that the microwave field is not precisely perpendicular and has a parallel component. We note that this experimental setup does not differentiate between the two perpendicular fields in the vertical and horizontally transverse directions; the spectrum appears to look the same regardless of which perpendicular field direction we have.

When there is no field, accomplished by canceling the ambient field using the Helmholtz coils, the Zeeman sublevels are degenerate. Therefore, there is only one double resonance peak [Fig. 3.5(b)]. This peak appears to have a broader FWHM compared to the peaks in the presence of Earth's field. One reason may be because the static magnetic field is not precisely zero, so there exist closely spaced Zeeman sub-levels. The nine transitions are not resolved and overlap, giving a broader peak.

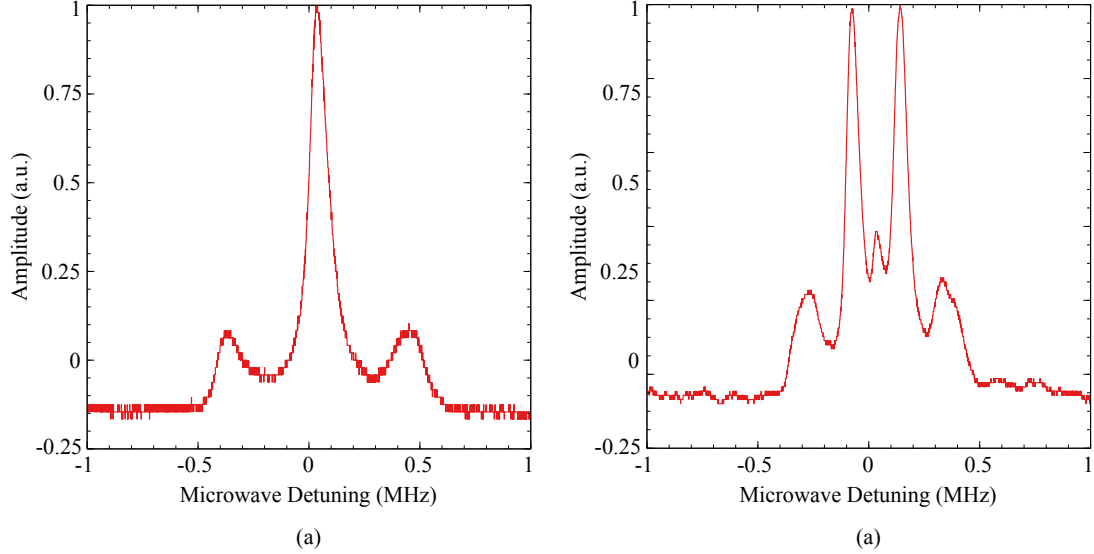


Figure 3.6: Double resonance spectra when the microwave field is (a) parallel to \mathbf{B}_{DC} [π -polarization] and (b) when the field is perpendicular to \mathbf{B}_{DC} [equal parts σ_{\pm} -polarization]. The amplitudes have been normalized such that the maximum amplitude is 1.

To verify, we will need to modify our setup to better null the ambient field.

3.3.1 Three Level Model

We can analyze the system using a three-level approximation [36], as shown in Fig. 3.4(c). The ground states $|1\rangle$ and $|2\rangle$ with energies $\hbar\omega_1$ and $\hbar\omega_2$ respectively, represent each of the two pairs of hyperfine ground states involved in the transitions driven by the microwave field. The excited state $|e\rangle$ of energy $\hbar\omega_e$ represents the state $|F' = 0, m_{F'} = 0\rangle$. The microwave field is assumed to be on resonance and homogeneous over the cell, having the following form

$$\mathbf{B}_{\mu}(r, t) = B_{\mu} \cos(\omega_{\mu}t) \mathbf{e}_{\mu}, \quad (3.2)$$

The microwave field has angular Rabi frequency equal to $\hbar\Omega_{\mu} = \mu_{\text{B}}B_{\mu}M_{\pi, \sigma_{\pm}}^n$, where $M_{\pi, \sigma_{\pm}}$ is the M1 matrix element from Eqs. 2.49 and 2.51 for transition number n . The probe addressing levels $|1\rangle$ and $|e\rangle$ has the form

$$\mathbf{E}_{\text{P}}(\omega_{\text{L}}, t, r) = E_{\text{o}} \cos(\omega_{\text{P}}t) \mathbf{e}_{\text{rad}}. \quad (3.3)$$

The interaction Hamiltonian is $H_{E1} = -e\mathbf{r} \cdot \mathbf{E}_P$, giving an optical Rabi frequency of $\hbar\Omega_P = E_o \langle e | e\mathbf{r} \cdot \mathbf{e}_{\text{rad}} | 1, 2 \rangle$. Only atoms in $|1\rangle$ contribute to absorption. The decay from the excited state proceeds at a rate Γ^* and includes the effect of spontaneous emission. If the pumping rate is greater than the microwave Rabi frequency rate, which is true for our pump beam, we can treat the optical pumping rate as a longitudinal relaxation [Γ_1 in Section 2.6] between the two ground states, which we will denote as γ_1 . The total Hamiltonian for this system in the basis $|1\rangle, |2\rangle, |e\rangle$ is

$$\hat{H} = \hbar \begin{pmatrix} \omega_1 & \Omega_\mu e^{-i\omega_\mu t} & \Omega_P e^{-i\omega_P t} \\ \Omega_\mu e^{i\omega_\mu t} & \omega_2 & 0 \\ \Omega_P e^{i\omega_P t} & 0 & \omega_e \end{pmatrix}. \quad (3.4)$$

We calculate the evolution of the density matrix elements,

$$\rho = \begin{pmatrix} \rho_{11} & \rho_{12} & \rho_{13} \\ \rho_{21} & \rho_{22} & \rho_{23} \\ \rho_{31} & \rho_{32} & \rho_{33} \end{pmatrix}, \quad (3.5)$$

using Liouville's equation and then add the decay terms in a phenomenological manner, as was done in Sections 2.5.3 and 2.6. The results are

$$\frac{d}{dt}\rho_{11} = \Omega_\mu \text{Im}\{\rho_{12}e^{-i\omega_\mu t}\} + \Omega_P \text{Im}\{\rho_{1e}e^{-i\omega_P t}\} + \frac{\Gamma^*}{2}\rho_{ee} - \gamma_1\left(\rho_{11} - \frac{1}{2}\right) \quad (3.6)$$

$$\frac{d}{dt}\rho_{22} = -\Omega_\mu \text{Im}\{\rho_{12}e^{-i\omega_\mu t}\} + \frac{\Gamma^*}{2}\rho_{ee} - \gamma_1\left(\rho_{22} - \frac{1}{2}\right) \quad (3.7)$$

$$\frac{d}{dt}\rho_{ee} = -\Omega_P \text{Im}\{\rho_{1e}e^{-i\omega_P t}\} - \Gamma^*\rho_{ee} \quad (3.8)$$

$$\frac{d}{dt}\rho_{12} = i\omega_{21}\rho_{12} + i\frac{\Omega_\mu}{2}e^{i\omega_\mu t}(\rho_{11} - \rho_{22}) + i\frac{\Omega_P}{2}e^{i\omega_P t}\rho_{e2} - \gamma_2\rho_{12} \quad (3.9)$$

$$\frac{d}{dt}\rho_{1e} = i\omega_{e\mu}\rho_{1e} + i\frac{\Omega_P}{e^{i\omega_P t}}(\rho_{ee} - \rho_{11}) + i\frac{\Omega_\mu}{2}e^{i\omega_\mu t}\rho_{2e} - \frac{\Gamma^*}{2}\rho_{1e} \quad (3.10)$$

$$\frac{d}{dt}\rho_{2e} = i\omega_{e2}\rho_{2e} + i\frac{\Omega_\mu}{2}e^{-i\omega_\mu t}\rho_{1e} - i\frac{\Omega_P}{2}e^{i\omega_P t}\rho_{21} - \frac{\Gamma^*}{2}\rho_{2e}, \quad (3.11)$$

where we have written for short $\omega_i - \omega_j = \omega_{ij}$. We have also used the simplification,

$$\text{Im}(\rho_{nm}e^{i\omega_a t}) = -\frac{1}{i}\rho_{nm}(e^{i\omega_a t} - e^{-i\omega_a t}) = -\rho_{nm}\sin(\omega_a t). \quad (3.12)$$

If the intensity of the probe is low, which is true for our case, we can assume that $\rho_{ee} \approx 0$ and $\rho_{11} + \rho_{22} = 1$, which says that the total population is equal to the sum of the population in the ground states. We move into the rotating frame by substituting [37]

$$\rho_{12} = \delta_{12} e^{i\omega_\mu t} \quad (3.13a)$$

$$\rho_{1e} = \delta_{1e} e^{i\omega_P t} + \epsilon_{1e} e^{i(\omega_P - \omega_\mu)t} \quad (3.13b)$$

$$\rho_{2e} = \delta_{2e} e^{i\omega_P t} + \epsilon_{2e} e^{i(\omega_P - \omega_\mu)t}, \quad (3.13c)$$

into Eqs. 3.6(a)-(f), which we then solve for the coherence terms “rotating” with the same frequency as the probe frequency, δ_{ij} , in the steady-state. As the probe laser frequency is narrower than the hyperfine splitting [MHz vs. GHz], we can assume that only atoms in $|1\rangle$ contribute to absorption. Starting from the Maxwell’s equation,

$$\nabla \times \mathbf{E}_L = -\frac{\partial \mathbf{B}}{\partial t} \quad (3.14)$$

can derive the relationship between the electric field \mathbf{E}_L and the medium polarization $\mathbf{P} = \epsilon_o \chi(\omega) \mathbf{E}_L$ in a polarized medium with atom density n . We use the following equations,

$$\nabla \times \mathbf{H} = \mathbf{J} + \frac{\partial}{\partial t} \mathbf{D} \quad (3.15a)$$

$$\mathbf{B} = \mu_o (\mathbf{H} + \mathbf{M}) \quad (3.15b)$$

$$\mathbf{D} = \epsilon_o \mathbf{E}_L + \mathbf{P} \quad (3.15c)$$

$$\mathbf{J} = \sigma \mathbf{E}_L \quad (3.15d)$$

We assume that our medium, the rubidium vapor, has zero conductivity, $\sigma = 0$, and that the magnetization, \mathbf{M} , is zero. Taking the curl of Eq. 3.14 and simplifying the result using Eqs. 3.15a-d, we obtain the following relation between the electric field interacting with the atoms and the polarization created,

$$\frac{\partial^2 \mathbf{E}_L}{\partial z^2} - \epsilon_o \mu_o \frac{\partial^2 \mathbf{E}_L}{\partial t^2} = \mu_o \frac{\partial^2 \mathbf{P}}{\partial z^2}. \quad (3.16)$$

This can be rewritten in terms of the optical Rabi frequency as [37]

$$\frac{\partial \Omega_{\text{P}}}{\partial z} = \kappa(\omega_{1e}) \text{Im}\{\delta_{1e}\}, \quad (3.17)$$

where

$$\kappa(\omega_{e1}) = \text{Im}\{\chi\} = n \frac{\omega_{e1}}{c\epsilon_0 \hbar} |\langle e | \mathbf{e} \mathbf{r} \cdot \mathbf{E}_{\text{L}} | 1 \rangle|^2 \text{ m}^{-1} \text{ s}^{-1} \quad (3.18)$$

is the absorption coefficient. We integrate Eq. 3.17 as a function of z to obtain the Rabi frequency, which is proportional to the electric field \mathbf{E}_{L} at any point z in the atomic vapor. In particular, we are interested in \mathbf{E}_{L} at the end of the vapor cell where the light exits. Therefore, to find the transmission of the intensity of the laser, we need to calculate the complex amplitude of the optical coherence, $\text{Im}\{\delta_{1e}\}$. In the limit where the decay rate Γ^* is much greater than the optical Rabi frequency, the optical coherence in steady state after moving to the rotating frame is [37]

$$\delta_{1e} = -i \frac{\Omega_{\text{L}}/2}{\frac{\Gamma^*}{2} + i(\Omega_{\text{L}} - \omega_{e1})} \rho_{11}, \quad (3.19)$$

where

$$\rho_{11} = \frac{1}{2} \frac{\gamma_1}{\gamma'_1} + \frac{1}{4\gamma_1} \left(\frac{S^n}{S^n + 1} \right) \left(\frac{\Gamma_{\text{P}}}{1 + \Delta_{\mu}^2 / [\gamma'_2(S + 1)]} \right). \quad (3.20)$$

Here, $\gamma'_i = \gamma_i + \Gamma_{\text{P}}/2$, $\Delta_{\mu} = \omega_{\mu} - \omega_{21}$ is the microwave field detuning for the transition of interest, and

$$S^n = \frac{\Omega_{\mu}^2}{\gamma'_1 \gamma'_2} = \begin{cases} \frac{(B_{\mu} \cos \theta)^2}{\gamma'_1 \gamma'_2} M_{\pi}^n = S_{\pi}, & \pi \text{ transitions} \\ \frac{(B_{\mu} \sin \theta)^2}{\gamma'_1 \gamma'_2} M_{\sigma_{\pm}}^n = S_{\sigma_{\pm}}, & \sigma_{\pm} \text{ transitions.} \end{cases} \quad (3.21)$$

is the saturation factor for transition number n . The optical pumping rate Γ_{P} from $|1\rangle$ in the numerator of the second term of ρ_{11} is

$$\Gamma_{\text{P}} = \frac{|\Omega_{\mu}/2|^2 \Gamma^*}{(\Gamma^*/2)^2 + (\Omega_{\text{L}} - \omega_{\mu} - \omega_{e2})^2}, \quad (3.22)$$

and is obtained by solving for the solutions to the coherence terms in the rotating frame in steady state. When the laser radiation is on resonance with the $|1\rangle \rightarrow |e\rangle$ transition, the pumping rate is equal to $\Gamma_{\text{P}} = |\Omega_{\mu}|^2 / \Gamma^*$.

The first term in Eq. 3.20 gives the equilibrium population due to optical pumping and the second term is the double resonance signal under the influence of the applied microwave field. As our oscilloscope was set to AC coupling, the DC signal corresponding to the first term is subtracted out during data collection, so we observe only the second term. The double resonance signal is a Lorentzian and has a full-width half-maximum equal to

$$\Delta\omega_{1/2} = \frac{1}{\pi}\gamma'_2(S^n + 1)^{1/2}. \quad (3.23)$$

The maximum amplitude of the resonance curve depends on the projection of the microwave field along the x or z axis as well as the transition matrix element. It was obtained by taking the second term in Eq. 3.20 at zero-detuning. For π and σ_{\pm} transitions, the maximum amplitudes are

$$A_{\pi}^n = \frac{\Gamma_P}{4\gamma_1\gamma_2} \left(\frac{S_{\pi}^n}{S_{\pi}^n + 1} \right) \quad (3.24a)$$

$$A_{\sigma_{\pm}}^n = \frac{\Gamma_P}{4\gamma_1\gamma_2} \left(\frac{S_{\sigma_{\pm}}^n}{S_{\sigma_{\pm}}^n + 1} \right). \quad (3.24b)$$

We note that the resonance linewidth depends on how well the cavity is tuned to the correct resonance [32]. The linewidth is thinner when the cavity is off resonance. Furthermore, the symmetry of the spectra depends on how close the cavity resonance frequency is to the hyperfine splitting: if the cavity is mismatched, then the double resonance spectra is asymmetric instead of the symmetric form shown in Fig. 3.5(a).

3.4 Vector Magnetometry

In the following section, we discuss the possibility of vector magnetometry using the double resonance spectrum. We look at it from a theoretical perspective and then show preliminary data in the next sections. This discussion motivates an application of micro-fabricated vapor cells.

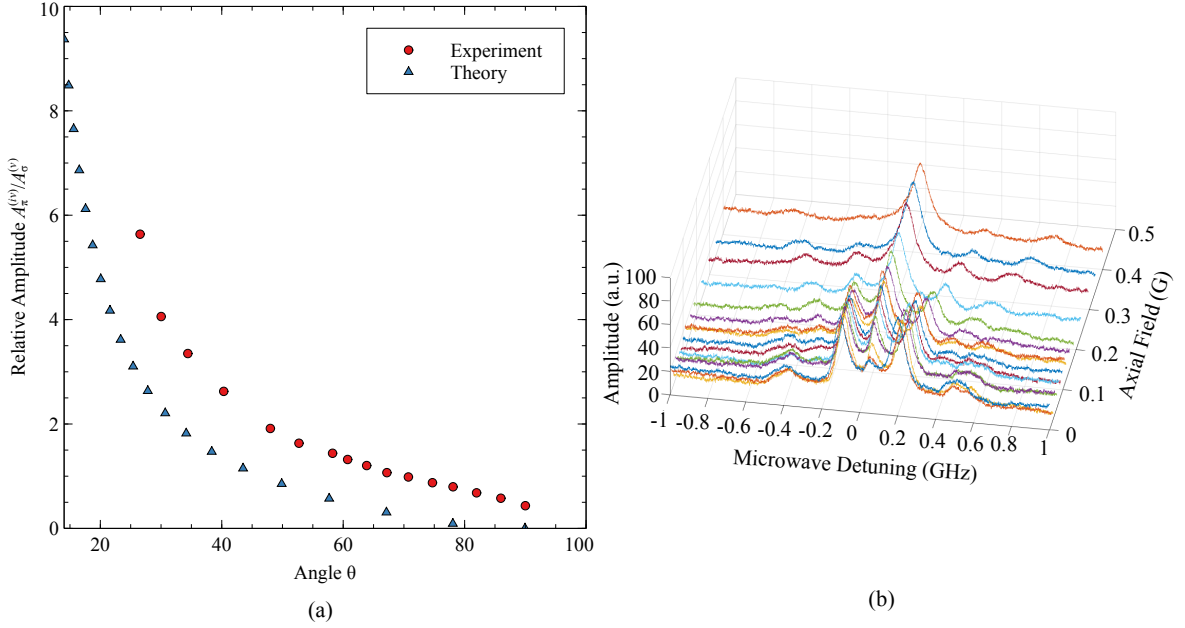


Figure 3.7: (a) Theoretical [blue triangles] and experimental [red circles] plot of $A_{\pi}^{(iv)}/A_{\sigma}^{(v)}$ [Eq. 3.26] as a function the angle θ between \mathbf{B}_{DC} and \mathbf{B}_{μ} . For the theoretical plot, $\Omega_{\text{P}} = 10^6$ Hz, $\Omega_{\mu} = 0.5 \times 10^3$ Hz, $\gamma_1 = \gamma_2 = 10$ Hz, $\Gamma^* = 10^9$ Hz. The values of γ_i were selected to try to match the maximum relative amplitudes of the theoretical and experimental data. (b) DR spectrum as a function of microwave detuning and increasing axial field strength when we apply a bias field of 0.2 G along the vertical direction.

3.4.1 Theory

The transitions induced by the parallel and perpendicular components of the microwave field \mathbf{B}_{μ} with respect to \mathbf{B}_{DC} are independent of each other and can be treated separately. This means that if we increase $(\mathbf{B}_{\mu})_z$ keeping $(\mathbf{B}_{\mu})_{\perp}$ fixed, then only the amplitudes of peaks (ii) , (iv) and (vi) corresponding to π -transitions will grow, while the amplitudes of peaks (i) , (iii) , (v) and (vii) corresponding to σ -transitions will remain the same. Similarly, if we increase $(\mathbf{B}_{\mu})_{\perp}$ keeping $(\mathbf{B}_{\mu})_z$ fixed, then only the amplitudes of peaks (i) , (iii) , (v) and (vii) will grow. The ratio between the amplitudes of the σ_{\pm} and π transitions gives a measure of the relative angle θ between

the microwave and the static magnetic field, since, from Fig. 2.4,

$$\theta = \arctan \frac{B_\mu \sin \theta}{B_\mu \cos \theta} = \arctan \frac{B_{\text{DC}}^\perp}{B_{\text{DC}}^\parallel}. \quad (3.25)$$

Between π transition n and σ transition m , the expression for the ratio is

$$\frac{A_\pi^n}{A_{\sigma_\pm}^m} = \frac{M_\pi^n}{M_{\sigma_\pm}^m} \left(\frac{B_\mu^2}{\tan \theta} \right) \left(\frac{B_\mu^2 \sin^2 \theta + \gamma'_1 \gamma'_2}{B_\mu^2 \cos^2 \theta + \gamma'_1 \gamma'_2} \right) \quad (3.26)$$

depends on θ . This gives us a method for vector magnetometry, where the ratio provides information on the direction of the DC field with respect to the microwave field alignment. In Fig 3.7(a), we plot with blue triangles the theoretical maximum amplitude ratio between transitions (iv) and (v) , $A_\pi^{(iv)}/A_{\sigma_+}^{(v)}$, as a function of θ , which shows that as the axial field is increased [decrease in θ], the π transition amplitude increases relative to its neighbouring σ_+ transitions. To find the magnitude of the field, it suffices to look at the frequency shifts of the peak due to Zeeman splitting. However, with the current configuration, we can only determine one angle, not the two needed to determine a unique direction in 3D space. With our setup, there is an infinite number of possible directions for \mathbf{B}_{DC} on a cone with angle θ relative to its axis [Fig 3.8].

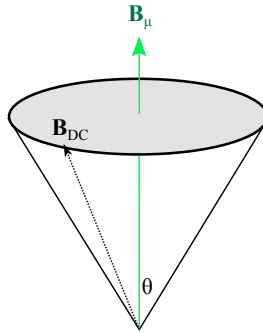


Figure 3.8: The infinite possible directions of \mathbf{B}_{DC} lie on a cone with aperture 2θ .

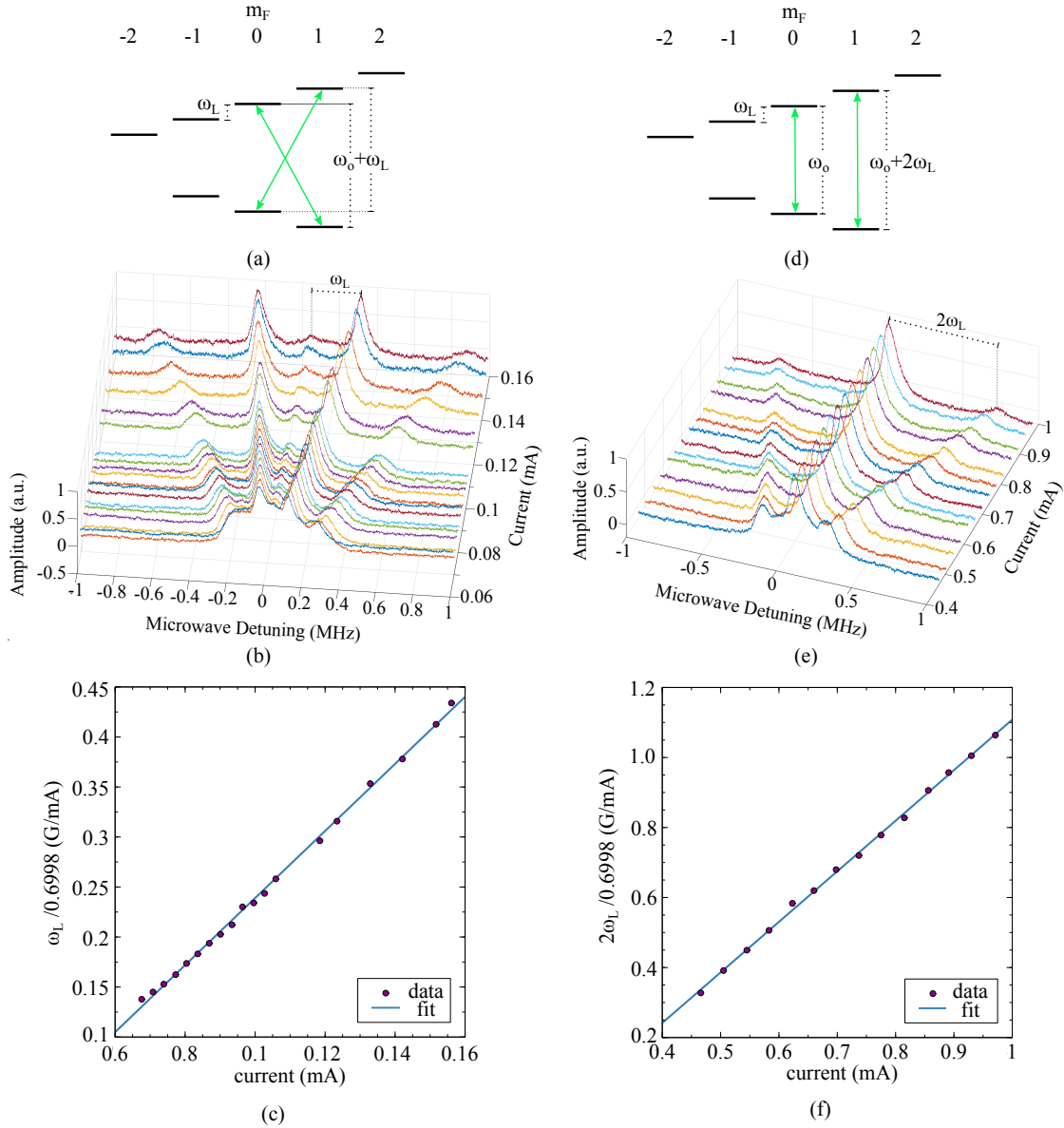


Figure 3.9: Calibrating the axial coils. (a) σ_+ transitions are detuned by $+\omega_L$ while (b) the right right π transitions are detuned by $2\omega_L$. MAOP spectra as a function of microwave detuning and increasing current in the axial coils due to a magnetic field applied in the (b) vertical and (e) axial direction. Labeled on the last curves are the corresponding frequency shift ω_L and $2\omega_L$, which are measured from the first peak on the right to the center peak as shown by the dotted lines. The frequency shift (c) ω_L are plotted as a function of applied vertical current and (f) $2\omega_L$ as a function of applied axial current, both fitted to a linear function to obtain the calibration factor m .

3.4.2 Experimental Data

Coil Calibration

To determine the relationship between the input current and the output magnetic field strength, the Helmholtz coils need to be calibrated. Calibration was done by measuring the current I through the wires with a multimeter and by measuring the Larmor frequency ω_L from the DR spectrum. Due to the low field Zeeman effect, the resonance frequency of the π -transitions occur at $\omega_o \pm 2\omega_L$ [Fig. 3.9(a)], which appears as curves shifted by $\pm 2\omega_L$ from zero detuning. For σ_{\pm} transitions numbers (iii) and (iv), the frequency shift is ω_L [Fig. 3.9(d)], where

$$\omega_L = \frac{\mu_B g_F}{\hbar} \times |\mathbf{B}_{DC}| = 0.6998 \frac{\text{MHz}}{\text{G}} \times |\mathbf{B}_{DC}|. \quad (3.27)$$

Therefore, to find $|\mathbf{B}_{DC}(I)|$, we need to measure the frequency shift of the first right-hand peak with respect to the center as a function of applied current I and then fit the data to the function

$$\frac{\omega_L}{0.6998 \frac{\text{MHz}}{\text{G}}} = mI + b, \quad (3.28)$$

where m is the slope corresponding to the magnitude of the field at a given current I , and b is the offset. A non-zero b indicates that the ambient field was not completely zeroed when calibrating the coils. As an example, shown in Fig. 3.9(a) is the double resonance spectra as a function of increasing axial current and microwave detuning. The frequency shift of the peaks appears to increase linearly with the applied current. This is confirmed by inspecting a plot of ω_L versus the applied current in Fig. 3.9(b). The results of the linear fits give the following calibration factors: 34 ± 4 mT/A for the vertical coils, 1.44 ± 0.09 mT/A for the axial coils, and 85 ± 1 mT/A for the horizontally transverse coils. The errors were taken from the standard error of the fit.

This technique for measuring the magnetic field strength is quick, taking only a few seconds for the signal to respond to a change in magnetic field strength or orientation as it depends only on the steady-state distribution of the atoms in the ground-state.

Unlike pump-probe experiments, we do not have to optically pump the atoms, probe the system during relaxation, and repeat the process to get an accurate measurement of the Larmor frequency. However, our sensitivity is limited by the linewidth of the peaks; we need to be able to resolve two peaks in order to measure their frequency separation. We estimate the smallest magnetic field strength we would be able to measure is about 0.15 G.

Vector Magnetometry (Preliminary Data)

Because the π -transitions are visually the same for both perpendicular fields, we apply only two combinations of the field: along the vertical and axial directions, or along the horizontally transverse or axial directions. An example is shown in Fig. 3.7(b), where we increase the net field $\mathbf{B}_{\text{DC}}^{\parallel} = [0, 0.44]$ G along the axial direction in the presence of a net bias field of $\mathbf{B}_{\text{DC}}^{\perp} = 2.0$ G along the vertical direction. We calculate θ by inserting in our values for the static fields in the second equality in Eq. 3.25.

When $\theta = 90^\circ$, the net field \mathbf{B}_{DC} points along the perpendicular direction. As the axial field increase, θ decreases. In Fig. 3.7(a) with red circles, we plot $A_{\pi}^{(iv)}/A_{\sigma_+}^{(v)}$, the ratio of amplitudes between π -transition (iv) and σ_+ -transition (v), against the θ . We can see from both plots that as we increase the axial field [decrease in θ], the center peak amplitude, which is caused by a π -transitions, increases relative to the neighbouring peaks caused by σ_+ .

The linewidth of each of the double-resonance peaks limits our ability to measure the Larmor frequency. When the magnetic field strength is small, the DR curves merge, and the curves are not well resolved. When the magnetic field strength is higher, we require a higher microwave detuning range to cover the spectrum. However, the further we move away from resonance, the lower the coupling efficiency is for the microwave field with the cavity, and the peak amplitudes begin to diminish. These factors limit the sensitivity of the magnetometer.

We calculated the amplitudes by subtracting the noise floor from the maximum

amplitude. Between measurements, the noise floor fluctuates quite a bit, possibly because of vibrations, and the cavity often became misaligned, which altered the peak amplitudes. Other issues with our data were inconsistency between measurements due to various factors such as insufficient and inconsistent vapor density, laser power instability due to perhaps the temperature in the room, and other unknown reasons. Between the same type of measurements, the relative amplitudes curves do not look the same. Compared to the theoretical curve, the experimental curve is shifted more to the right. Theory predicts that when the axial field is zero, the relative amplitude should be zero because we should not see any π -transitions. However, the height of the last red point corresponding to $\theta = 90^\circ$ in Fig. 3.7(a) is non-zero, indicating that there is a residual field along the microwave field direction. The experimental data is shifted more to the right, indicating that the maximum amplitude difference between the transitions (iv) and (v) is less than predicted. This may be because the decay terms $\gamma_{1,2}$ between the ground state is lower, due to the low density of our vapor. We did not measure atomic number density as we discovered a leak in our system, which was rapidly depleting our rubidium source within a day. We did not calibrate the pump and microwave Rabi frequency in the experiment, which is something to explore in the future to better understand our model.

Due to these inconsistencies, we do not fit our data to our model, as they look different, and we do not perform any statistical analysis. We also did not perform measurements to estimate the microwave Rabi frequency. Moreover, the model does not account for the cavity quality factor, which affects the signal linewidth and amplitudes. Therefore, the data presented seeks only to give a qualitative picture of the relationship between the peak amplitudes and the direction of the magnetic field. In principle, we would calibrate our “magnetometer” by fitting it to a curve, extract the damping terms, and then use those values to extrapolate the angle for a given amplitude ratio. s

Chapter 4

Microfabricated Vapor Cells

This chapter covers the micro-fabrication of a rubidium vapor cell. The primary motivation is to combine miniaturized cells with smaller microwave cavity resonators, which can be used for applications such as microwave-to-optical transduction [5] and optical switching [32]. Other applications include quantum sensing, such as magnetometry, as discussed in the previous chapter. As a first step, our goal was the test for the presence of rubidium, which was successful.

We introduce the basics of microfabricated vapor cells in Sections 4.1–4.3 and outline the fabrication steps in Section 4.4. Finally, in Section 4.5, we show results confirming the presence of both rubidium isotopes. As we have not yet optimized the cell to be compatible with quantum sensing applications, we outline future steps for improving vapor purity, cell lifetime, and reducing decoherence effects in Section 4.6.

4.1 Background

Glass-blowing is a common technique for fabricating vapor cells, but it is difficult to create cells with volumes less than a few mm^3 [8]. As such, many have adopted methods based on silicon micromachining to fabricate alkali vapor cells. In these cells, chambers that confine the alkali atoms are etched into a Si wafer. Glass wafers are bonded to the polished upper and lower surfaces of the Si wafer, forming a sealed glass-silicon-glass three-layer “sandwich”. The glass windows allow light to pass through

the cell for atom-light interrogation. There are a few advantages of silicon micromachined vapor cells. Firstly, the dimensions can be specified in the etch pattern and wafer thickness with sub-millimeter precision. Secondly, chambers can be fabricated in parallel on one wafer, allowing multiple cells to be made simultaneously. Moreover, microfabrication techniques easily permit the integration of optical components, such as micromirrors and vertical-cavity surface-emitting lasers.

4.2 Alkali Atom Source

Because alkali atoms are highly reactive and readily oxidize at standard room temperature and pressure, a challenging aspect of vapor cell fabrication is introducing alkali atoms and sealing the cell [8]. Pure alkali metal must be handled in an inert atmosphere, such as in N_2 , and stored in hermetically sealed containers. To circumvent challenges associated with the handling of pure alkali metals, one method is to react stable alkali-based compounds with reducing agents or by dissociating the compounds with heat or light within the sealed cell. For example, alkali molybdates or chromates, which are stable in air and ambient temperature, can be reacted with zirconium, titanium, aluminum, or silicon at temperatures above 350°C to produce alkali metal in elemental form. In our process, we used micro-pills containing ^{85}Rb and ^{87}Rb from **SAES Getters** [Italy]. These micro-pills are composed of rubidium molybdate and an alloy of zirconium and aluminum, all compressed together [38]. The pill is placed inside the vapor cell which is then subsequently sealed. A laser beam at high power heats the dispenser to temperatures above 600°C , evaporating Rb. The process yields the following chemical reaction



The byproducts of this reaction are chemically and thermally stable at temperatures below 1000°C [39]. The oxides and an excess of Zr_3Al_2 remain in the dispenser.

4.3 Architecture

Within the chamber, a transparent light path is necessary for laser interrogation. To avoid the disturbance of impurities in the optical path, we designed cells with two connected chambers, one of which contains the rubidium source and the other for laser interrogation. The interrogation chamber confines the atoms so that they can be excited and probed by electromagnetic fields. Because we were unable to acquire double-sided polish wafers, our cells have a blind hole instead of a through-hole design. The depth of the chamber is limited by the wafer thickness (in our case, 1 mm); the back panel cannot be too thin otherwise the wafer can easily shatter. Recalling the Beer-Lambert law, which relates the outgoing beam intensity $I(z)$ through an absorbing medium of density n to the initial intensity I_o ,

$$I(z) = I_o e^{-n\sigma(\omega)z}, \quad (4.2)$$

where $\sigma(\omega)$ is the photon absorption scattering cross-section [see Appendix B.2.1] and z is the optical path length. Therefore, if the optical path length increases, then there is more absorption. In the conventional glass-silicon-glass three-layer sandwich design, the wafer thickness limits the optical path length. Since polishing machines cannot accommodate thicker wafers, the thickness of Si wafers is usually less than 2 mm thick [40]. Instead of propagating the laser beam through the cell, the beam reflects off angled sidewalls [created by potassium hydroxide wet etching in the interrogation chamber], traveling along the chamber surface, as shown in Fig. 4.1. By increasing the chamber dimensions, we can increase the optical path length without sacrificing cell thickness. The entire process flow is detailed in Section 4.4. To increase the reflectance of the walls, we deposited a thin layer of pure aluminum [Al] on some of the samples. During the deposition process, a shadow mask covered parts of the cell that did not need a mirror coating. However, due to difficulties with beam size and angle alignment, we did not use the sidewalls. Instead, we reflected the beam from the back walls, which gave us an appreciable atomic signal.

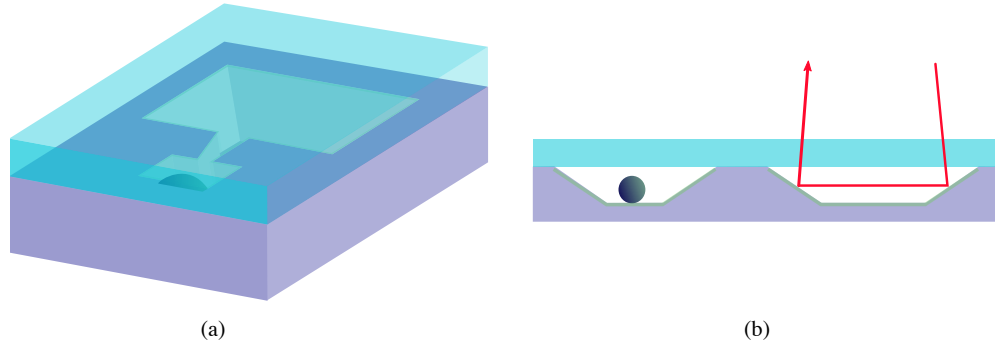


Figure 4.1: Vapor cell with reflecting sidewalls schematic; (a) 3D view and (b) side view cut out.

4.3.1 Silicon

Single-crystal silicon is an excellent electronics material. A common method for growing silicon crystals is the Czochralski [CZ] process but it tends to introduce more impurities compared to another popular method, the float-zone process. However, purity is not a concern for our purposes; the prime-grade wafers purchased for our experiments were grown with the CZ process. Similarly, for our purposes, the grade of the wafer is not of high importance and we purchased what was readily available.

Silicon belongs to the crystal cubic system and has a diamond structure. Each atom is symmetrically surrounded by four equally spaced neighbors in a tetrahedral arrangement, as shown in Fig. 4.2(b). By convention, the length of each edge is unity. The directions and planes in a crystal are identified by Miller indices h , k , and l . The Miller indices are determined by taking the reciprocal of the intercepts of that plane with the axes x , y , and z , and then multiplying them by the smallest common denominator to obtain whole numbers. Planes are denoted by parentheses and a family of planes are represented by curly brackets, e.g. the planes (001) , (100) , (010) , $(00\bar{1})$, $(\bar{1}00)$ and $(0\bar{1}0)$ are grouped under $\{100\}$ [the overline indicates negative direction]. The vector normal to the surface, written in square brackets, determines the direction, while the set of crystallographically equivalent di-

directions that form the same group is written with angular brackets, e.g. $\langle 100 \rangle$, $[010]$, and $[001]$ are part of the group of $\langle 100 \rangle$ directions. Planes (hkl) are perpendicular to the direction $[hkl]$. The angle θ between two planes (h_1, k_1, l_1) and (h_2, k_2, l_2) is given by

$$\theta = \cos^{-1} \frac{h_1 h_2 + k_1 k_2 + l_1 l_2}{\sqrt{h_1^2 + k_1^2 + l_1^2} \sqrt{h_2^2 + k_2^2 + l_2^2}}. \quad (4.3)$$

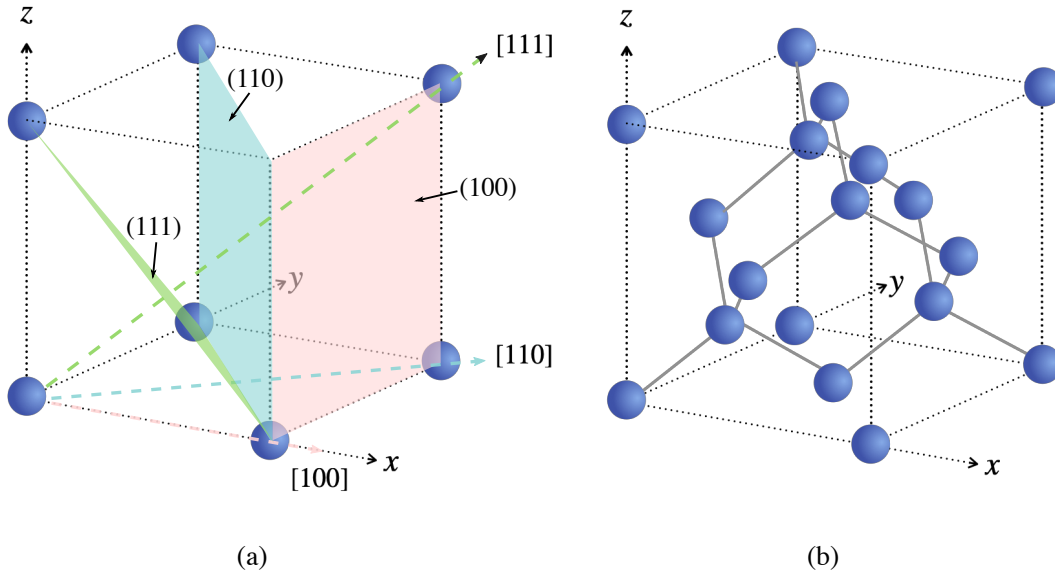


Figure 4.2: (a) Miller indices for the $[100]$, $[110]$, and $[111]$ directions, and the corresponding (100) , (110) , (111) planes, which are perpendicular to their respective directions. (b) Diamond structure of silicon. Each atom has four adjacent neighbours.

Silicon wafers come in different crystal orientations, which determines how a wafer is etched. A flat segment on a wafer helps determine the wafer orientation and conductivity type. Silicon can be p-type, where most of the charge carriers are positive, or n-type, where most of the charge carriers are negative. For vapor cells, the conductivity is not important, but the type of dopant can affect the plasma etching rates of silicon. Conventions for wafer flats are given in Fig. 4.3(a). On a $\{100\}$ wafer, the $[110]$ direction is given by the primary flat; an example with a $\{100\}$ n-type wafer showing the $\{100\}$ plane is illustrated in Fig. 4.3(c). We used $\langle 100 \rangle$, p-type [boron

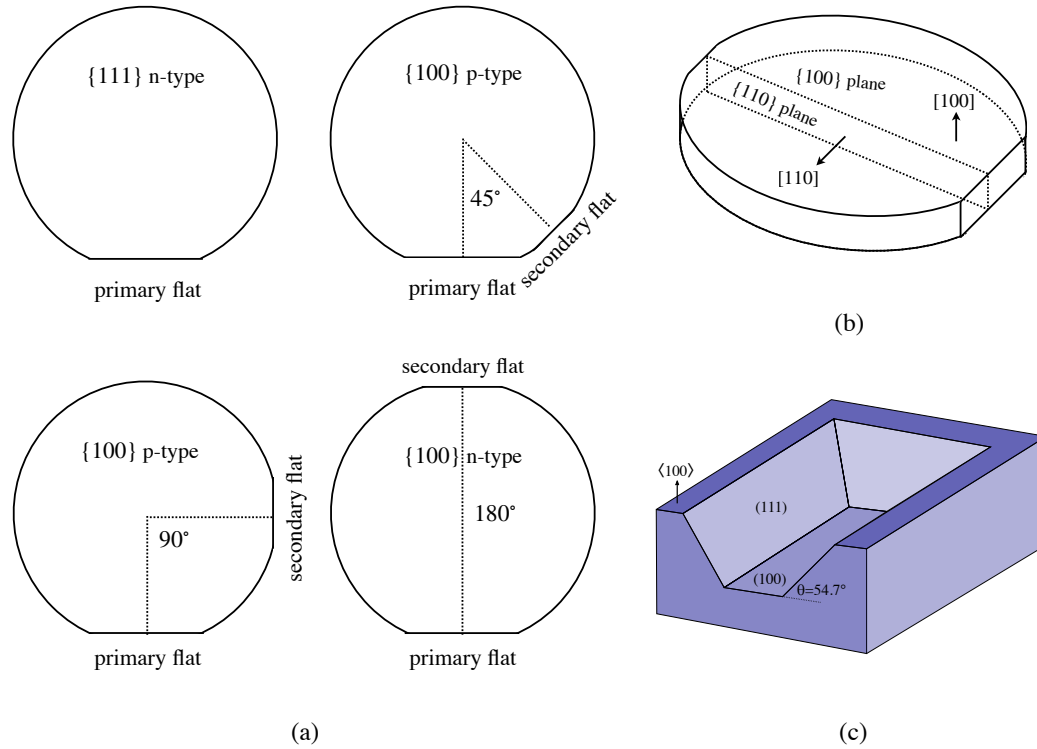


Figure 4.3: (a) Conventions for silicon wafer flat orientations. (b) 100 n-type wafer showing the $\{100\}$ plane and $[100]$ direction. The primary flat gives the $[110]$ direction. (c) Schematic of anisotropically etched features on a $\langle 100 \rangle$ wafer with a square mask.

doped] Si wafers for our vapor cells. From Eq. 4.3, the $\{111\}$ planes are angled 54.7° relative to the $\{100\}$ plane. Using KOH, we can anisotropically etch preferentially along $\langle 111 \rangle$ to create angled sidewalls.

4.3.2 Design

In the first round of fabrication, we patterned three sets of cells having interrogation chamber lengths $l = 6, 9, 12$ mm, giving a total of nine cells. In the second round, sixteen cells were made, with chamber lengths $l = 6, 9, 12, 15$ mm [not shown]. The cell patterns were designed in **MATLAB** using the **Raith_GDSII Toolbox** [41] and is shown in Fig. 4.4. We did not design a shadow mask for the second set of cells, as we omitted the aluminum deposition step.

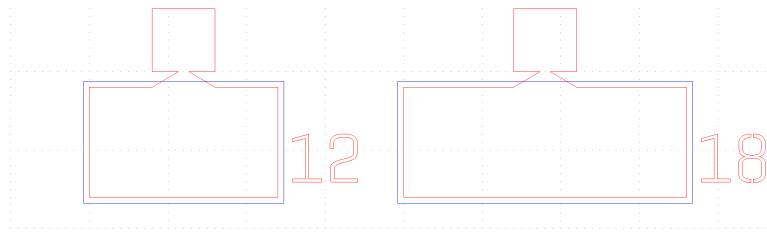


Figure 4.4: Vapor cell [red line] and shadow mask (purple line) pattern. The numbers beside each cell indicates the width of the interrogation chamber on the vapor cell wafer.

4.3.3 Sealing

The entire cell must be hermetic to prevent reactive contaminants such as oxygen and water from entering and oxidizing the alkali atoms and to prevent non-reactive contaminants such as He or N₂ from entering and leaving the cell, causing shifts in the transition frequency of the alkali atoms. The glass and silicon wafers are bonded under vacuum using anodic bonding [Section 4.4.8]. Bonding is only effective between two polished surfaces. Since we could only acquire single-sided polished wafers at the time, we did not design through-hole cells. We also chose to work with 100 mm in diameter wafers as some of the equipment in the nanoFAB were only compatible with 100 mm wafers.

4.4 Process Flow

The vapor cell pattern was created on the wafer by wet etching using potassium hydroxide [KOH]. Any part of the silicon wafer not covered by silicon nitride was etched away. The vapor cell pattern thus depends on the low-stress silicon nitride pattern. To create a silicon nitride pattern, we coat the layer of SiN with a photoresist pattern generated by direct-write laser lithography. Reactive ion etching then removes any part of the silicon nitride layer not protected by the photoresist. Finally, the photoresist was removed by plasma etching, exposing the silicon nitride layer. The etching of the Si wafer begins when we immerse the wafers in a solution of KOH.

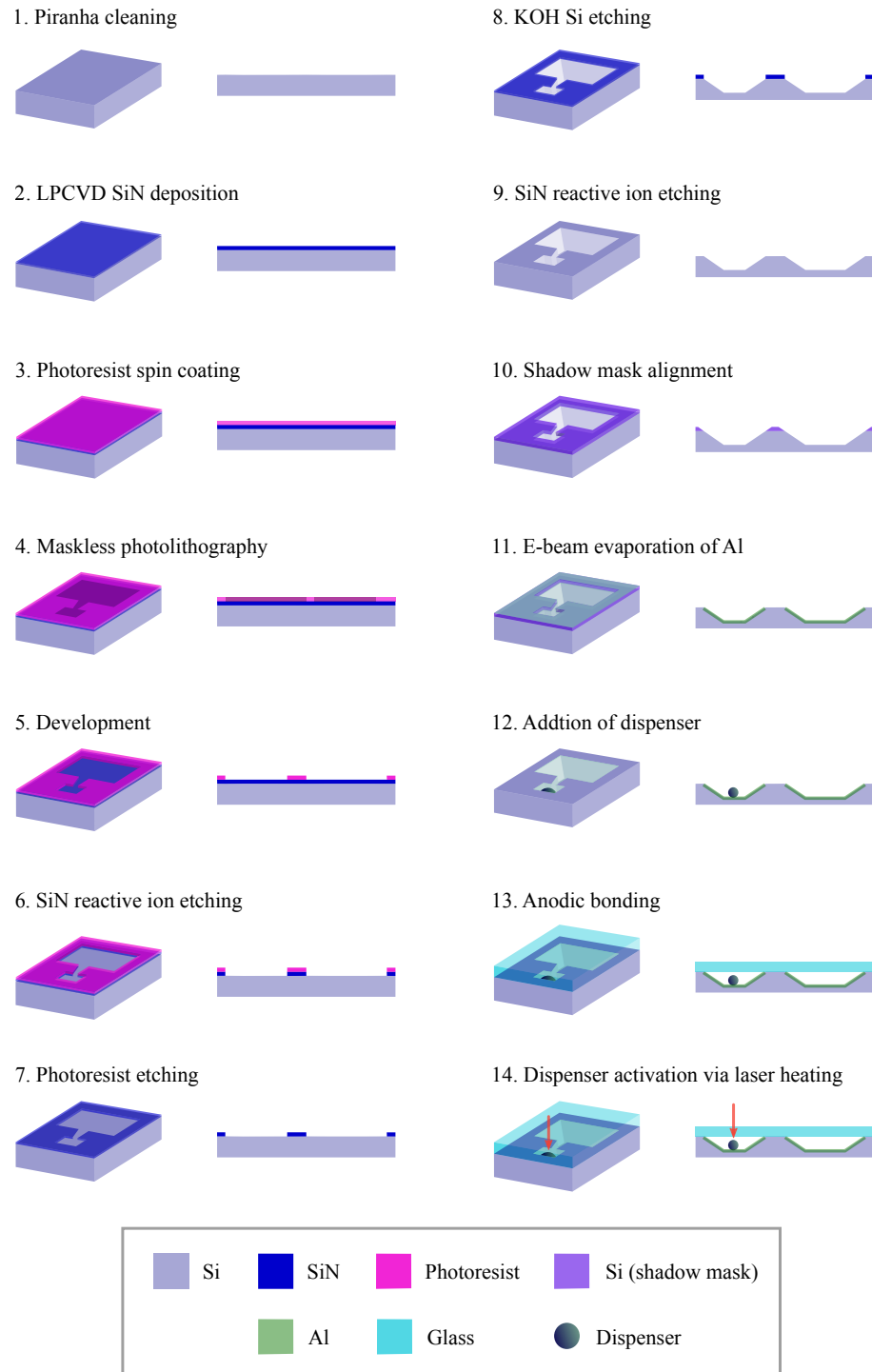


Figure 4.5: Process flow showing the 3D and side views of the wafers at each step.

4.4.1 Wafer Cleaning

As a first step, the vapor cell, shadow mask, and glass wafers were cleaned using the standard nanoFAB “Piranha” bath to remove organic and metallic components from substrates. We used a 3:1 mixture of sulphuric acid [H_2SO_4 , 96% concentration], a highly corrosive strong mineral acid, and hydrogen peroxide [H_2O_2 , 30% concentrate], a strong oxidizer. The solution can self-heat up to 120°C . Most surfaces become hydroxylated [addition of -OH group], becoming strongly hydrophilic. The wafers were placed in a Teflon carrier and immersed for 15 minutes in the Piranha bath. After 15 minutes, the solution cools, and the reaction is no longer vigorous enough to clean effectively. The wafers were removed from the bath and rinsed with de-ionized water.

4.4.2 LPCVD Nitride Deposition

After the Piranha cleaning process, a 75 nm thick film of low-stress silicon nitride [LS SiN] was deposited onto both silicon wafers by low-pressure chemical vapor deposition [LPCVD]. This process was done as a fee-for-surface by nanoFAB staff. Silicon nitride is a dielectric material that can be used as a KOH etch mask. The most thermodynamically stable silicon nitride is Si_3N_4 , but it does not always have that stoichiometry. LS SiN is richer in silicon, giving it very high tensile strength [tensile strength is a measure of the force required to pull something apart to the point it breaks]. Because the etch rate of LS SiN in KOH is very slow, it can be used as an etch-resistant barrier. In 44% KOH at 85°C for example, the etch rate of LPCVD SiN is less than 0.1 nm/min, which is slower than Si_3N_4 at 1 nm/min [42]. The reaction that occurs during LPCVD is



To produce LS SiN, a higher ratio of dichlorosilane SiH_2Cl_2 [DCS] to ammonia NH_3 is used. In chemical vapor deposition [CVD], the reactants DCS and 4NH_3 are trans-

ported as gases into the CVD reaction chamber where the substrate [Si wafer in our case] is located. The surface of the substrate exposed to the gases acts as the growth surface. The film precursor molecules adsorb onto this surface. The substrate is heated to very high temperatures to initiate surface reactions, causing continuous film growth. Any byproducts are then desorbed and flow away towards the reactor exit. The deposition method affects quality and dielectric strength. LPCVD usually occurs at pressures of 100 Pa, while atmospheric CVD occurs at 10-100 kPa. LPCVD decreases any unwanted gas-phase reactions, as well as increases the uniformity of the film. For LPCVD LS SiN growth, the deposition temperature is 800-840°C.

4.4.3 Resist Spin Coat

Resists are mainly composed of a polymer [a base resin], a sensitizer, and a casting solvent [42]. When exposed to radiation, the polymer changes structure and can be dissolved by a developer to form the design pattern. The solvent allows layers to be formed on the wafer surface and the sensitizer controls the chemical reactions in the polymeric phase.

Before coating the wafer with photoresist, which will be needed for the photolithography step, the wafer is first coated with hexamethyldisilazane [HMDS], a surface linking adhesion promoter [43]. Surface priming was introduced to improve the photoresist-wafer contacts. SiN is polar whereas photoresist is nonpolar, which creates adhesion problems between the two layers. The polar bonds on the SiN surface form long-range hydrogen bonds with water adsorbed onto the surface. The photoresist does not adhere to hydrated silicon surfaces, so the surface of the wafer must be dehydrated as well.

Wafer priming was accomplished in the **YES3TA HMDS Oven**, which elevates the wafer temperature and reduces the pressure, lowering the boiling point of water molecules. The chamber is then flooded with HMDS vapor, which when deposited, silylates the silicon nitride surface. This introduces a silyl group, R_3Si , leaving a non-

polar surface. We apply 1.1 μm thick layer of AZ1512 photoresist (approximately 5 mL), which bonds to HMDS, using the **CEE 200CB Coat Bake System**. The photoresist is poured onto the wafer which sits on a rotating mount. The wafer is first spun at 500 RPM for 10 seconds [s] to spread the photoresist, followed by 40 s at 5000 RPM.

After resist coating, the resist may contain built-in stresses. To remove these stresses and to promote adhesion, the wafer is soft-baked [also known as pre-baked] on a hotplate at 100 °C for 60 s. Soft-baking reduces the thickness of the photoresist by 10-25% [42]. Excessive baking can destroy the photosensitive compound and reduce sensitivity.

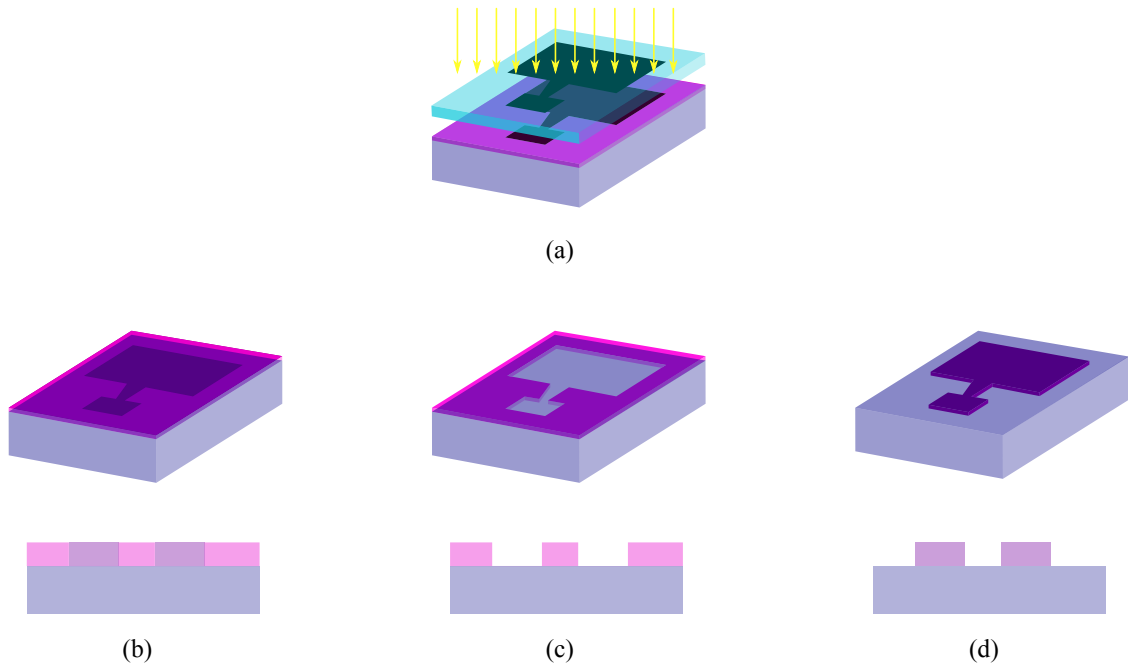


Figure 4.6: (a) Photoresist exposed to UV light. The mask serves as a photoresist pattern. After exposure (b) for negative-tone photoresist, parts that are not exposed to light are removed during development, (c) while for positive-tone photoresist, parts that are exposed to light are removed during development.

AZ1512 is a positive tone photoresist, suitable for both wet and dry etching. Exposure to light causes a reaction: the polymers break down and become soluble in a developer solution, as shown in Fig. 4.6(c). On the other hand, for negative-tone

photoresists, parts that have not been exposed to light are removed by the developer solution. Positive photoresists have better resistance to etchants, such as KOH, than negative photoresists, but do not adhere to silicon wafers as well as negative photoresists. The AZ1500 series photoresists have a wide process latitude, a larger extent to which they can be over or underexposed, while still providing acceptable results. The wavelengths of light used in photolithography range from very short wavelengths of extreme UV [10-14 nm] to near UV [350-500 nm]. AZ1500 photoresists provide good resolution in broadband and near UV. Typically, the “g” [436 nm], “h” [405 nm], or “i” [365 nm] line of a mercury lamp are used for near UV light.

4.4.4 Direct-Write Laser Lithography

In traditional lithography, a stencil, called a *mask*, is used to generate the lithography pattern [42]. A photomask, either a glass [transparent to near-ultraviolet (UV)] or quartz [transparent to deep UV] plate patterned with an absorber metal opaque to UV light, is placed in direct or near contact with the resist-coated wafer. The mask-wafer system is then exposed to UV light and then developed to generate the pattern on the substrate.

However, in our process, we use a maskless photolithography system, which does not require the use of a photomask. The **Heidelberg MLA150** is ideal for designs that involve size features over one micron [44]. In maskless photolithography, a spatial light modulator acts as a programmable, dynamic mask that is used to directly project the design onto the wafer.

After exposure to near UV light [we used the “h” line], the photoresist layer needs to be developed: unpolymerized resist that forms the latent image needs to be dissolved to form the design pattern. We developed our photoresist pattern at room temperature by placing the wafer in a glass container filled with a sufficient amount of AZ 400K 1:4 developer, a buffered potassium-based inorganic developer pre-diluted with de-ionized [DI] water. The container was gently agitated for about a minute to improve

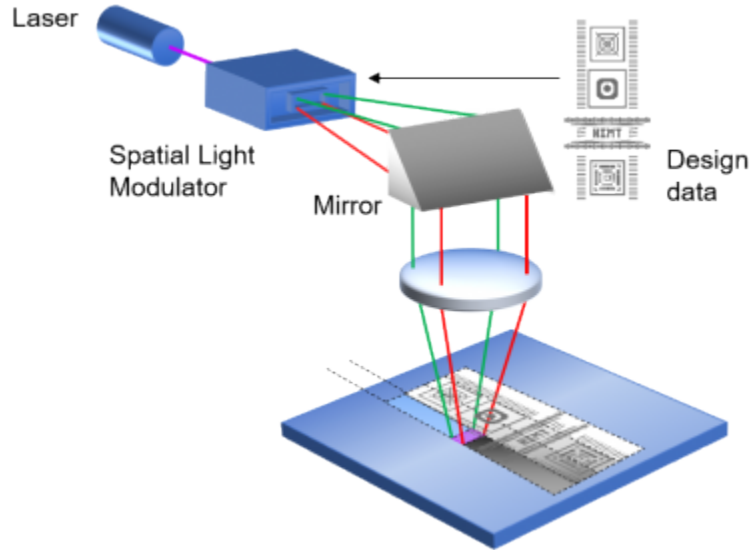


Figure 4.7: Maskless lithography uses a spatial light modulator. Figure from [44].

development uniformity. The wafer is then rinsed with DI water and dried with a nitrogen spray gun.

4.4.5 Nitride Etch and Resist Strip

The photoresist pattern now exposes certain regions of the nitride layer. These exposed nitride regions must be etched away to form the KOH etching mask. Reactive ion etching [RIE] is a dry etching technique that combines physical and chemical mechanisms to remove the surface of a material. The substrate is physically bombarded with ions with sufficient energy to break the chemical bonds of the surface atoms, which reduces the activation energy required for chemical etching reactions. In the **Trion Phantom RIE**, plasma, which are ionized gas molecules that are neutral with equal numbers of ions and electrons, is produced using a radiofrequency [RF] field. The wafer is placed on an RF power electrode, taking on a potential that accelerates ions towards its surface. The surface then chemically reacts with plasma molecules, and the reactants in the gas or vapor phase are removed by pumping. The ion bombardment is highly directional, so RIE is highly anisotropic, forming vertically etched sidewalls. RIE also has a high etch rate and high selectivity [selectivity

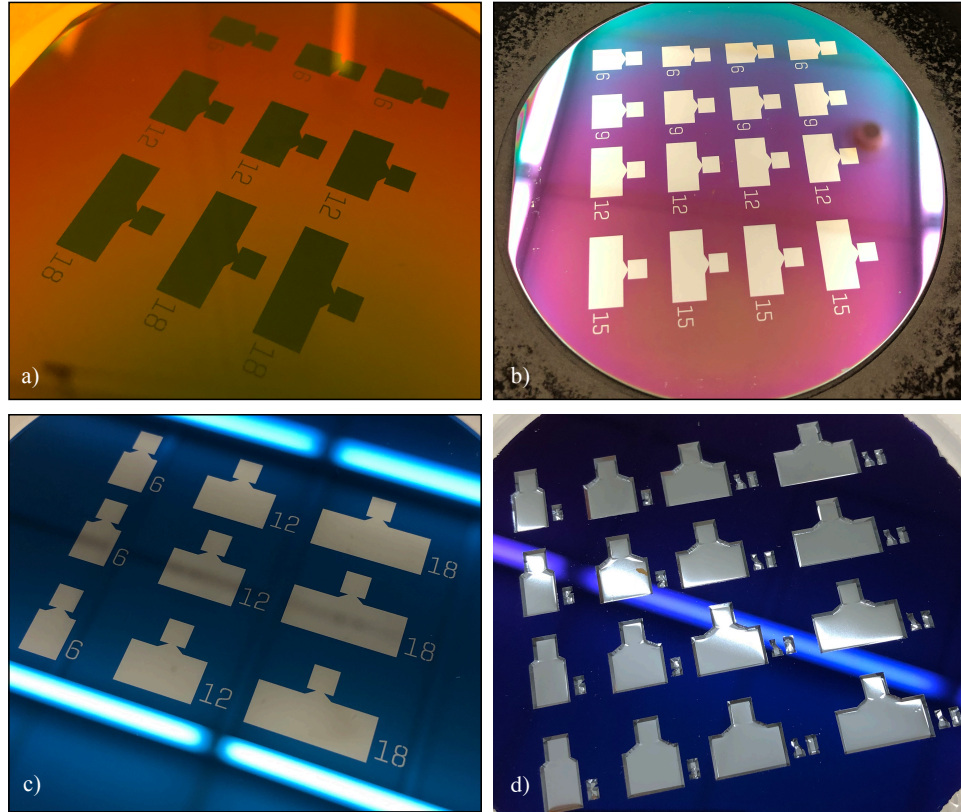


Figure 4.8: Vapor cell after (a) photoresist patterning, exposure, and development, (b) nitride stripping, (c) photoresist stripping, and (d) KOH etching.

is the ratio between the etch rate of the material to be removed and the etched rate of the material to remain]. The etch rate for the standard nanoFAB LS SiN recipe is 118 nm/min. We set the process to run for 42 seconds, which was sufficient to remove 75 nm of LS SiN.

The photoresist on both wafers was removed by oxygen plasma stripping in the **Branson 3000 Barrel Etcher** [42]. In the pre-heating step, which ran for 3 minutes, N₂ gas fills the chamber. The pressure reduces down to 1.4 Torr. In the second step, reactive atomic oxygen [O], formed by splitting molecular oxygen [O₂] using a low-pressure electrical discharge, converts an organic photoresist such as AZ1512 into a gaseous product that is pumped away. This step ran for 10 minutes, which is generally

enough time to remove 1-2 μm of resist.

4.4.6 KOH Wet Etch

Potassium hydroxide was used to wet etch the wafers, covered by an LS SiN mask. We used a solution of 32% KOH [961 ml of 45% KOH diluted with 569 ml of water], to which we added 150 ml of isopropyl alcohol [IPA] in the first round of fabrication. IPA reduces surface roughness, which would improve reflectance. In the second round of cell fabrication, we did not use IPA, and the surface appeared to have more bumps on the tens of nm scale.

During the etching process, a circular stir bar at the bottom of the bath stirred the solution at a rate of 60 RPM. The bath was heated to a temperature of 85°C , which took approximately 30 minutes to heat up from room temperature. A probe inserted into the bath monitored the temperature. The first vapor cell wafer was etched $726 \mu\text{m}$ deep, for a total of 7 hours, giving an etch rate of approximately $1.7 \mu\text{m}/\text{min}$. The second vapor cell wafer was etched for seven hours to a depth of $680 \mu\text{m}$. The shadow mask, which will be placed on top of the vapor cell during electron beam [e-beam] deposition, was etched all the way through, forming $525 \mu\text{m}$ deep through-holes. The shadow mask was left in the solution until the vapor cell wafer was taken out. After the etching process, the wafers were rinsed in DI water and then dried using a nitrogen spray gun. The result is shown in Fig. 4.9(c).

KOH etching is an anisotropic, or directional, process. It etches preferentially in the $\langle 100 \rangle$ plane compared to the $\langle 111 \rangle$ plane, with a selectivity [etch rate ratio] of $S = R_{\langle 100 \rangle} / R_{\langle 111 \rangle} = 400$ [42], where $R_{\langle abc \rangle}$ is the etch rate along the $\langle abc \rangle$ direction. This causes $\langle 111 \rangle$ planes to be oriented 54.7° relative to the $\langle 100 \rangle$ plane. Since we use $\langle 100 \rangle$ wafers, sidewalls are formed relative to the surface of the wafer, as shown in Fig. 4.9. To determine the final feature size of the final etch for a $\langle 100 \rangle$ wafer, we can use the following formula

$$w = A + 2d \cot 54.7^\circ, \quad (4.5)$$

where A is the final [desired] feature size of the etch, w is the size of the photomask pattern, and d is the etch depth. The size of the hole on the shadow mask needs to

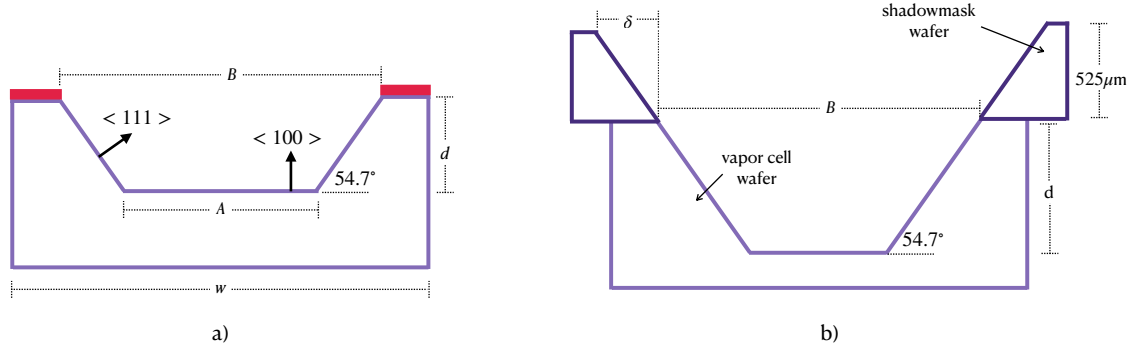


Figure 4.9: KOH etching on a $\langle 100 \rangle$ Si wafer produces sidewalls oriented at 54.7° relative to the surface. (a) KOH etching is highly selective: parts that are not protected by a mask [pink] are etched away. (b) The shadow mask wafer is etched all the way through, while the vapor cell wafer is etched partly through, to a depth of $X \mu\text{m}$. The bottom width of the shadow mask pattern needs to be the same size as the opening of the chamber, so the pattern was designed to be $2\delta = 2 \times 525\mu\text{m} \times \cot 54.7^\circ$ wider than B .

match the opening of the vapor cell cavities. The shadow mask square pattern was designed to be $2 \times \delta = 2 \times 525\mu\text{m} \times \cot 54.7^\circ$ wider than B , the opening of the vapor cell chamber, as shown in Fig. 4.9(b).

Wet etching is highly selective; with two materials present, one is etched at a much faster rate than the other. In our case, we have LPCVD SiN and Si. The selectivity of our KOH solution is $S = R_{\text{Si}}/R_{\text{SiN}} = 49000$. SiN is etched very slowly compared to Si. Note that high selectivity does not imply that the etching process is anisotropic.

4.4.7 Electron-Beam Deposition of Thin Films

Electron-Beam Evaporation

A bell-jar electron-beam [e-beam] evaporation system [nicknamed “Gomez”] from **Kurt J. Lesker** deposited a 100 nm thick layer of aluminum onto the vapor cell wafer, forming the reflecting sidewalls. Aluminum was placed inside a crucible located underneath the wafer, as shown in Fig. 4.10(a), (c), and (d). E-beam evaporation

uses an electron beam to heat the material that is to be deposited. The electron beam source generates electrons, accelerates, and deflects them towards the crucible. The electron beam position was controlled by electric and magnetic fields. Under vacuum, this created sufficient vapor pressure, causing it to evaporate and deposit onto the substrate. During the evaporation step, the electron beam dithers [sweeps] across the crucible. The dither rate and beam position was controlled by adjusting the current that produces the fields. The beam position needs to be at the center of the material; if the beam hits the crucible, film purity is affected.

Located next to the wafer in Fig. 4.10(c) and (d) is a crystal thickness monitor [CTM]. The CTM monitors the deposition rate and helps to calculate the film thickness. It contains a quartz crystal, which mechanically oscillates due to the piezoelectric effect when an AC voltage is applied. The resonance frequency depends on the mass of the film deposited onto it. Therefore, the CTM program needs to account for the material density [2.700 g/cc for Al] and the Z-ratio [1.080 for Al]. The Z-ratio corrects the frequency-change-to-thickness transfer function for the effects of acoustic impedance mismatch between the crystal and the deposited material.

Between the substrate and the crucible is a shutter. The shutter can be rotated to the “closed” position such that it covers the wafer when the e-beam is on [Fig. 4.10(c)], to stop deposition. It can also be rotated to the “open” position where it does not block the wafer [Fig. 4.10(d)]. To begin, we loaded the substrate, closed the shutter, and pumped the system down, first to below 300 mTorr with a roughing [mechanical] pump, and then to less than 10^{-6} Torr with a cryopump. The pump-down process took about an hour.

Because aluminum tends to creep up along the crucible walls when heated, the emission current of the e-beam was slowly increased to 20 mA, to prevent aluminum from overflowing out of the crucible. Increasing the emission current increases the temperature, which increases the deposition rate. We then adjusted the current until we achieved our target deposition rate. If the Al overflows out of the crucible, the

emission current needs to be reduced, allowing Al to sink back into the crucible. Through a glass windowpane located on the bell jar, we monitored the position of the beam and crucible. The final emission current during the process was set at around 10 mA, which gave us a deposition rate of approximately 10 \AA/s [0.1 nm/s], typical for Al deposition on this system. Deposition commenced once the shutter was rotated to its open position and the CTM was reset to zero to start to timer and thickness counter. The shutter was closed once we achieved the desired thickness, which took about 20 minutes for 100 nm of Al.

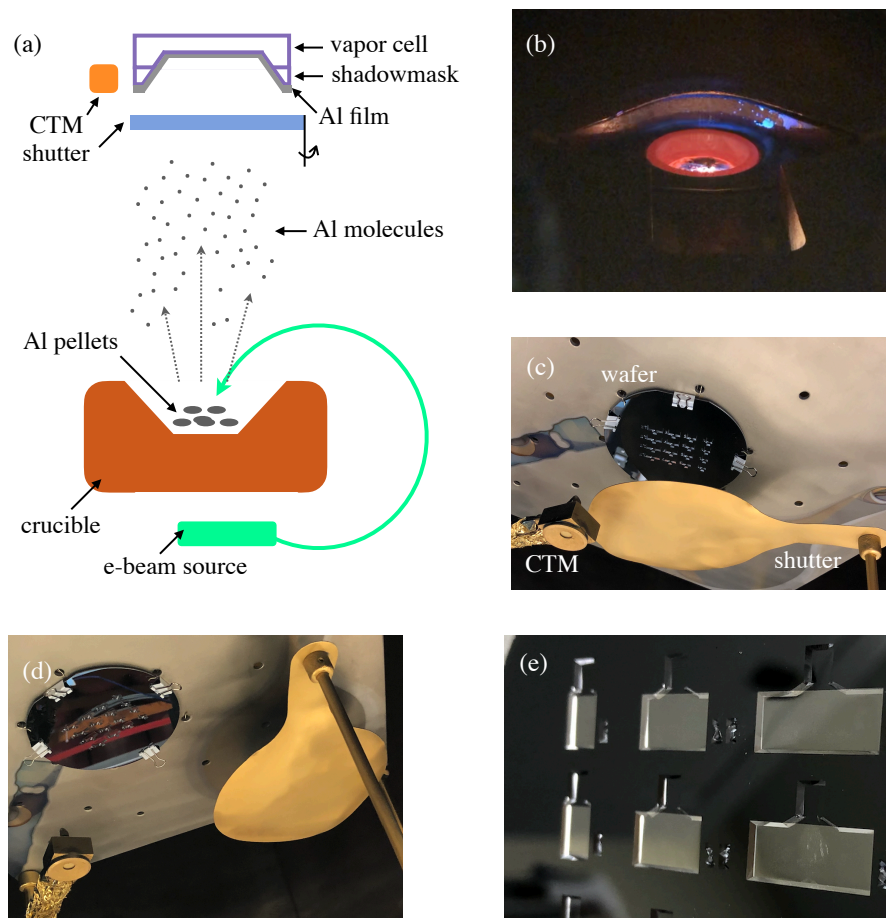


Figure 4.10: (a) Electron beam deposition schematic. A CTM measures the thickness of the film. (b) The electron beams scan across the crucible which contains the film material. (c) Closed position of the shutter to prevents unwanted deposition. (d) Open position of the shutter. The shinier part of the interrogation chamber is where the Al was deposited, which was not covered by the shadow mask. (e) vapor cell wafer after Al deposition.

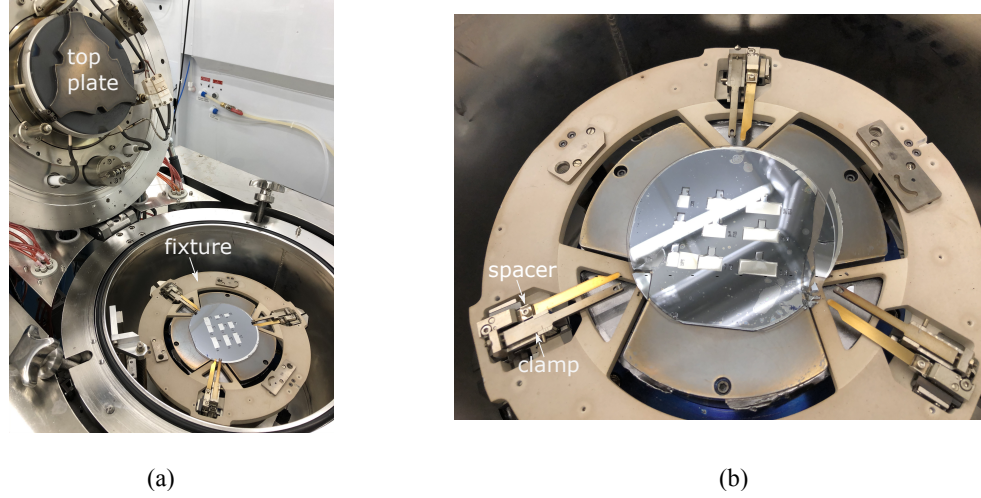


Figure 4.11: (a) The two wafers are fixed by a clamp on the fixture and placed on top of the bottom plate of the bonding system. The top plate is also the lid of the bonder and is the cathode. (b) Result of bonding. The wafer is noticeably cracked where the clamps/spacers were located.

At 780 nm, which corresponds to the D1 transition, $n = 2.50$, $k = 8.44$ for Al; these values can be calculated from the Lorenz-Drude model [45]. The reflectivity is obtained from the following equation,

$$R = \frac{[n(\omega) - 1]^2 + k^2(\omega)}{[n(\omega) + 1]^2 + k^2(\omega)}, \quad (4.6)$$

and is equal to 88% for aluminum.

4.4.8 Anodic Bonding

Anodic bonding, also known as field-assisted thermal bonding, is commonly used in MEMS fabrication to bond certain types of glass with conductive materials [8]. In our case, our substrate stack comprises a layer of glass and the Si wafer. Bonding involves pushing two substrates together using two heated plates that sandwich the layers. It occurs at high voltages, typically between 200-1000 V, and at high temperatures, 180-500°C, which necessitates using glass with a linear thermal expansion coefficient similar to that of the Si wafer. The linear thermal expansion coefficient is

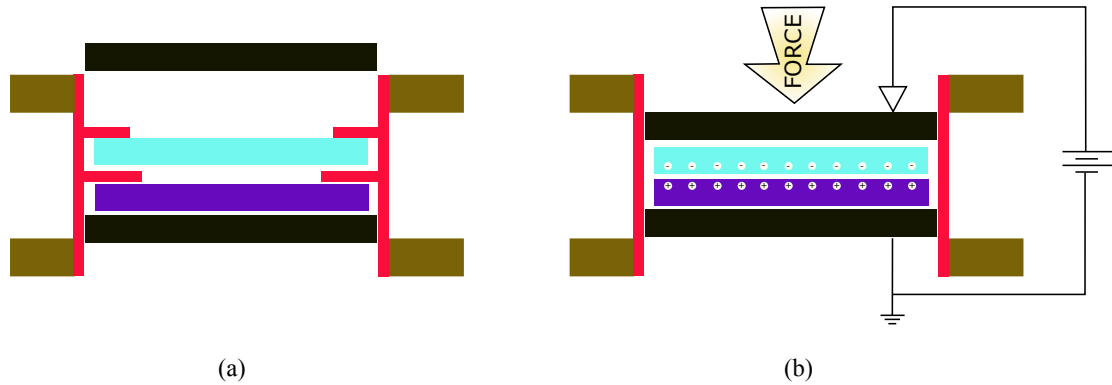


Figure 4.12: Schematic of anodic bonding. (a) The Si wafer [purple] is placed on the bottom of the fixture and the glass wafer [blue] on top. A spacer separates the two wafers. The sandwich is clamped and the fixture is placed on top of the bottom plate. (b) During anodic bonding, the spacer and clamps spring outwards, and a force is applied, pushing down the top plate. A cathode located on the top plate applies a voltage. The bottom plate kept electrically grounded, causing positive ions in the Si wafer to flow upwards towards the boundary and negative ions in the glass to flow downwards. Both plates are kept heated.

the fractional change in length of a material per degree change in temperature [linear expansion means a change in one dimension, as opposed to area expansion, two dimensions, and volumetric expansion, three dimensions]. During bonding, both wafers remain rigid. We used 100 mm diameter round Borofloat® glass wafers, which are borosilicate [silica and boron trioxide] based glass wafers manufactured by **Schott**. **Pyrex 7740** glass wafers, **Corning**'s trademark borosilicate glass that contains approximately 3-5% sodium, can also be used for anodic bonding in our vapor cells but was unavailable for purchase at the time. Borosilicate [silica and boron trioxide] glass has a low thermal expansion coefficient, meaning that it is more resistant to thermal shock. At temperatures between 0-300°C, the average thermal expansion coefficient of Pyrex is $3.25 \times 10^{-6}/^{\circ}\text{C}$; for silicon at 300 K, it is $2.62 \times 10^{-6}/^{\circ}\text{C}$. The thermal expansion of the bonding substrates should be similar to avoid thermal stresses.

Bonding was done on the **SUSS Microtech CB6L Substrate Bonder** [Fig. 4.11(a)], which can bond 100 mm and 150 mm wafers. A transport fixture mechanically clamps

Total Steps (15)	1	2	3	4	5	6	7	8	9	10	11	12	13	14	15
Top Temp. (°C)	200	200	350	350	350	350	350	350	350	350	350	350	200	200	200
Bottom Temp. (°C)	200	200	350	350	350	350	350	350	350	350	350	350	200	200	200
Chamber Press. (Torr)	Purge	2E-3	2E-3	2E-3	2E-3	2E-3	2E-3	2E-3	2E-3	2E-3	2E-3	2E-3	2E-3	Purge	Purge
Tool Press. (Torr)	0	0	0	0	0	0	0	0	263	263	263	263	263	0	0
Voltage (V)	0	0	0	0	0	0	0	0	0	0	-1000	-1000	0	0	0
Action					 CLAMPS OFF	 SPACERS OUT		 DOWN		1 2 					 UP

Figure 4.13: Anodic bonding steps. The actions in the cell editor are as follows: in step 5 the clamps are removed; in 6, the spacers are removed; in 8, the universal bonding tool is moved down; in 10, two electrodes are set; in 15 the universal bonding tool [a combination of the pressure and the bond head] is moved up.

the substrate stack. The stack is secured at the center of the fixture by three clamps [spaced at 120° intervals], with three spacers between the wafers to separate them before the bonding process. We put three dispensers into three separate cavities.

To form the bond, a voltage is applied, polarizing the sandwich. The bottom surface of the silicon wafer is electrically grounded while the top surface of the glass is placed into contact with a point electrode cathode, as illustrated in Fig. 4.12, keeping it at constant negative bias with respect to the grounded Si wafer. Since the top plate is the electrode, the glass must be placed on top of the fixture. The **SUSS Microtech CB6L** contains two electrodes on the top plate. In the preliminary steps 1-2 [Fig. 4.13], both plates are heated to 200°C, then to 350°C. At temperatures above 450°C, the thermal properties of the materials begin to deviate; therefore, bonding should be kept below 450°C.

The exact mechanism of anodic bonding is unclear, but electrochemical, electrostatic, and thermal mechanisms have been used to explain bond formation. At high

temperatures, glass becomes a solid conducting electrolyte and the sodium in the glass migrates towards the cathode, creating a sodium depletion layer at the glass-silicon interface, forming a capacitor. The applied voltage drops at this boundary, resulting in an attractive electrostatic force that pulls the wafers towards each other [46]. The wafers are held together by Van der Waals forces [46]. As the capacitor charges, the electric field is high enough that the oxygen in the glass drifts towards the positive silicon electrode to forming siloxane [Si-O] covalent bonds [which involves the sharing of electron pairs between atoms] at the glass-silicon interface.

To ensure that any vapor released by the pill is pumped out of the system, the bonding process is done under vacuum, down to 2.0×10^{-3} Torr. We modified the standard anodic bonding recipe; the steps are shown in Fig. 4.13. The entire process ran for approximately 2 hours. Bonding occurs during step 10 when the electrodes turn on. The process caused cracks on our first wafer sandwich near the clamps/spacers, as shown in Fig. 4.11(b). The cracks may have been caused by the spacers not retracting before applying the pressure. The cracks did not affect the cavities containing the dispensers. For the second set of cells, there were no issues with bonding.

4.4.9 Laser Activation

The dispensers were activated using a linearly polarized continuous wave (CW) Ytterbium laser from **IPG Photonics**, model **YLR-10-RP**, which can emit wavelengths between 1.03-1.07 μm with a maximum power output of 10 W.

Linearly polarized light exits through a fiber output and passes through a Faraday isolator, to prevent the beam from back-reflecting into the laser. It functions by rotating the polarization axis of the field with the help of a static magnetic field in the middle of the isolator and two beam-splitters on either end. Any light that is reflected into the isolator will have a different polarization axis angle. If the isolator is aligned such that maximal light is transmitted through one direction [away from the

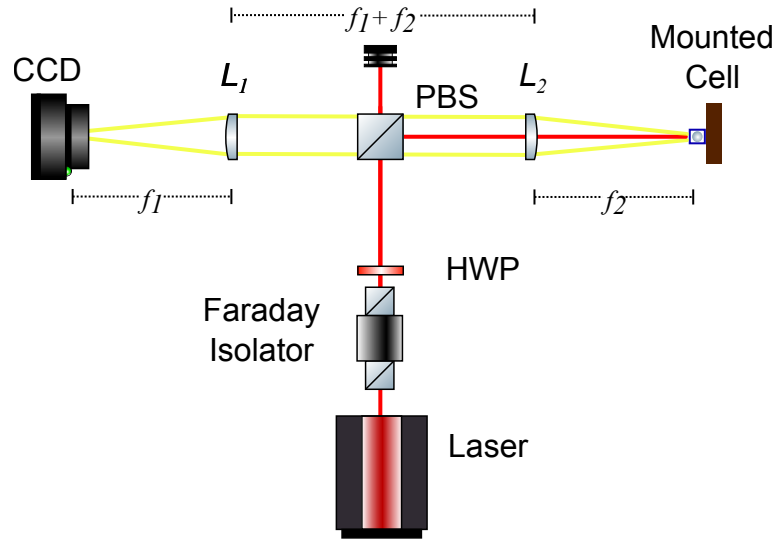


Figure 4.14: Imaging and dispenser activation setup. $f_1 = f_2 = f = 150$ mm.

laser], then in the opposite direction [towards the laser], minimum light is transmitted.

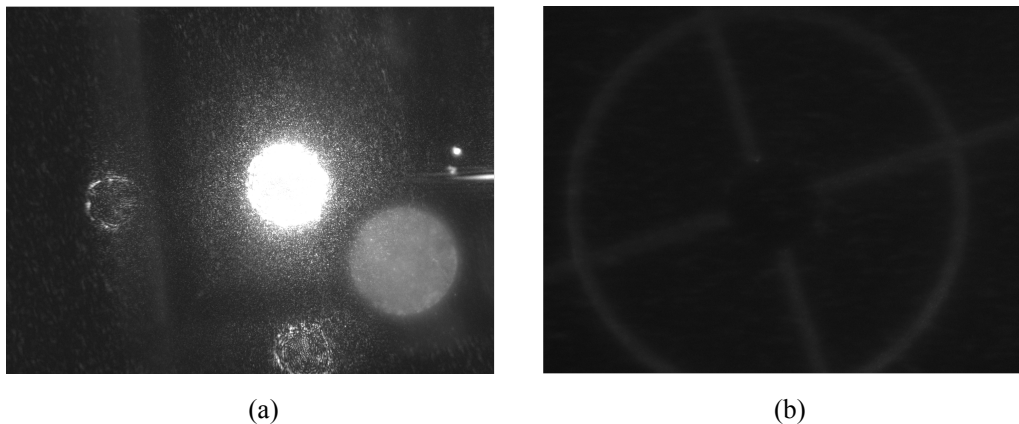


Figure 4.15: Image of (a) the 1064 laser beam [bright circle] and dispenser [grey circle] and (b) a target with a 0.5 mm diameter hole.

The entire wafer stack was clipped onto a sample holder. The beam is directed towards the vapor cell by reflecting it through a polarizing beam-splitter [PBS], which split the horizontally and vertically polarized components of the laser beam into different ports. A half-wave plate [HWP], which when rotated, changes the polarization angle of the linearly polarized field, is placed before the PBS to control the power out-

put through each port. We aligned the HWP such that minimal power is transmitted through the PBS. Any excess power goes into the beam blocker. An f - $2f$ - f imaging system was set up for aligning the beam with the dispenser. We used the **Blackfly S BFS-U3-16S2M** monochrome 1.6 MP camera with a progressive scan CMOS sensor from **Flir Systems Inc.**, capturing live, continuous images. The CCD is placed one focal length $f_1 = 150$ mm away from a plano-convex lens [L1]. Another plano-convex lens, L_2 , is placed $f_2 = 150$ mm away from the mounted cell. The distance between L_1 and L_2 is $f_1 + f_2 = 300$ mm. An image of the beam and the dispenser is shown in Fig. 4.15(a). Because the system was enclosed in a black box and the camera was unable to capture images in total darkness, we used an LED flashlight to illuminate the sample when capturing images. Using this setup, we were able to image a hole that was approximately 0.5 mm in diameter. [Fig. 4.15(b)].

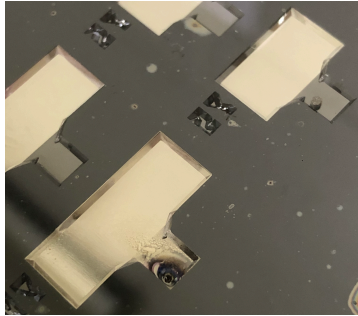


Figure 4.16: Activated Rb dispenser [bottom left] and inactivated dispenser [top right].

The dispenser was activated at the 1064 nm wavelength and 6.2 W power for 10 minutes. After 10 minutes, the power of the beam was decreased in increments of 30 s to avoid large temperature changes; from 6.2 W, to 5 W, to 3.7 W, to 2.5 W, to 1.2 W, to 0.1 W to 0 W. Due to the high heating of the laser beam, the dispenser cracked [Fig. 4.16], which was an issue in [47].

4.5 Rubidium Spectroscopy

4.5.1 Optical Setup

We used a **Moglabs CEL 780 nm** external chamber diode laser to measure the D2 absorption spectra of the released Rb in our cell. The optical setup is borrowed from the Hybrid Quantum Systems project and is described in [48]. The ECDL was connected to an external diode laser controller (EDLC) from **Moglabs**. The output channel A on the EDLC is used for monitoring the output. We connected channel A to channel 2 on an oscilloscope to simultaneously monitor the scan range of the laser while taking absorption data. The beam output is split by a beamsplitter [BS]. One of the ports is directed towards a photodetector [PD1] to measure the beam output, while output from the other BS port is reflected off the vapor cell. The reflected light is collected by another photodetector [PD2]. PD1 and PD2 are connected to channels 4 and 3, respectively, on our oscilloscope, which was triggered on rising edge by the signal from channel 1. Monitoring the signal of the beam on PD1 allows us to ensure that the data collected from PD2 is signal due to the rubidium in the cell and not the modulation due to the laser setup. Acquiring a good signal required adjusting the power of the beam, the sensitivity of the photodetector, the frequency span, and the diode current on the EDLC [which controls the laser frequency]. All collected signals were AC coupled on the oscilloscope, which removes the DC signal. For all measurements, the laser was unlocked and set to scan over a large frequency range that covers the absorption spectra of ^{85}Rb and ^{87}Rb .

4.5.2 Reflectance

We estimated the reflectance of the coated and uncoated parts of an empty cell by taking the ratio of the input and reflected power of the laser beam. For the part of the cell coated by the Al film, the measured reflectance was 87%, which is close to our estimated value of 88% from the Lorenz-Drudee model for an Al surface not covered

by glass. For the cell with the Si surface, the reflectance is 21%. The Al coating was unevenly distributed for parts of the cell, so the measurement was done on areas where the surface appeared to be smoother.

4.5.3 Absorption Measurements

Initially, we checked for the presence of rubidium by looking for fluorescence in the cell. The laser output was coupled to an aspherical pig-tailed collimator and reflected off the sidewalls. We used an IR viewer and turned off the lights in the room to reduce background light. However, the reflection of the laser is strong. Also, because the cell is small, we could not see any noticeable fluorescence because the reflected light dominated. Usually, by scanning the laser, the fluorescence from the atoms will flicker.

An alternative was to perform absorption measurements. To eliminate background noise, we turned off the lights in the room. As parts of the beam scattered off of the sidewalls, we did not use the reflecting sidewalls. Instead, the laser was reflected at an angle off of the back panel of the wafer. This allowed us to use a beam with a larger diameter, allowing more atoms to interact with the beam. We estimate the optical path length of the beam to be at least $l = 2 \times \text{cell depth} = 1452 \mu\text{m}$. The power into the cell was $1.35 \mu\text{W}$ and the reflected beam power was $0.64 \mu\text{W}$. The sensitivity on both photodetectors was +70 dB. To acquire a good signal, we heated the cell by hot air flow with a heat gun directed towards the glass surface. The cell temperature was measured by attaching a thermocouple to the Si side of the wafer. When the temperature reading was above 35°C , we were able to see the Doppler broadened peaks corresponding to the D2 transitions $F = 2 \rightarrow F'$ of ^{87}Rb , as well as the transitions from $F = 3 \rightarrow F'$ and $F = 2 \rightarrow F'$ of ^{85}Rb in the absorption spectra. The laser scan was unable to cover the $F = 1 \rightarrow F'$ transition ^{87}Rb . Figure 4.17 shows absorption spectra of the cell at room and warmer temperatures, with the reference laser scan. When the temperature increases, the dips become deeper, meaning that

there is more absorption because the atomic density increases.

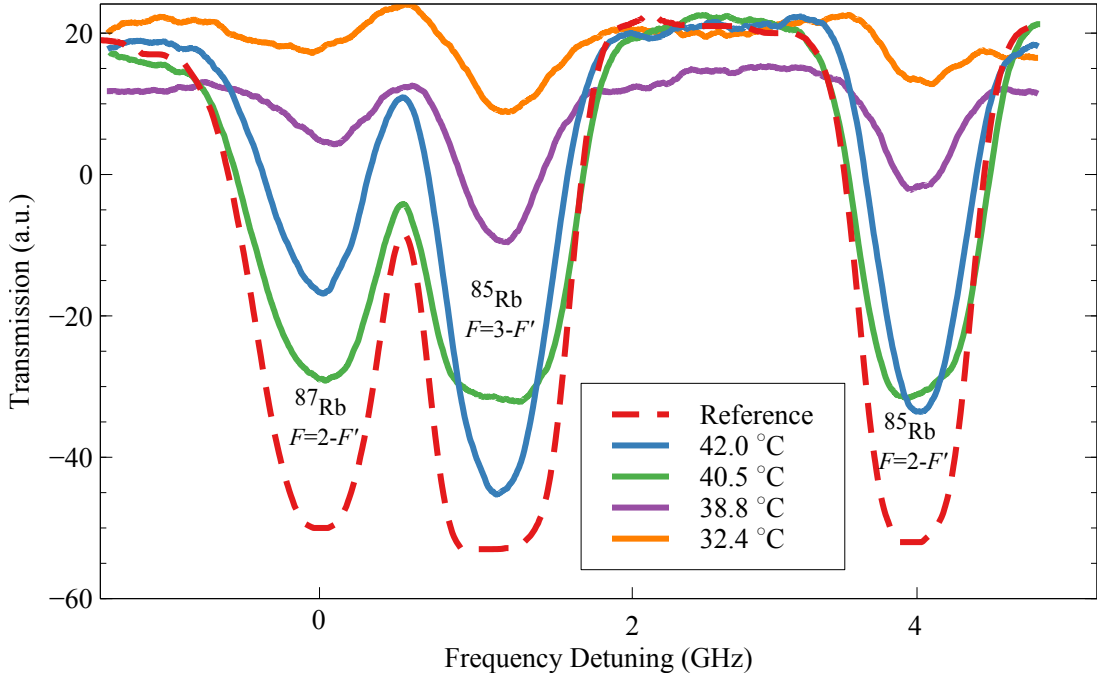


Figure 4.17: Doppler broadened spectra of rubidium at various cell temperatures [solid lines] give four peaks. The dotted red dotted line shows the reference signal from the EDCL. The transmission amplitudes were shifted in such a way that the maximum amplitudes were equal to the maximum amplitude of the reference signal. Because the reference signal, which was used to trigger the signal on the oscilloscope, shifted along the frequency axis between measurements, and because we show only one reference signal from one temperature measurement, the data points were shifted along the frequency axis so that the dips are located at the proper frequency detunings. All of the data were convoluted with a box of unit magnitude of size 100 to smooth out the digital noise from the oscilloscope. The laser scan was unable to cover the full range of the absorption spectrum of ^{87}Rb .

The atomic density n of rubidium atoms can be estimated by comparing the transmitted intensity A_1 and A_2 of any two peaks:

$$n = \frac{\ln(A_1/A_2)}{(\sigma_2 - \sigma_1)l}, \quad (4.7)$$

where

$$\sigma(\omega, \omega_o) = \sum_{F, \text{iso}} \sigma_{F \rightarrow F'}(\omega, \omega_o) f_{\text{iso}} n_{F'} \quad (4.8)$$

is the total optical absorption cross-sections over all dipole allowed transitions in both isotopes, weighted by $n_{F'}$ the fraction of the sample in the absorbing state [49]. This

fraction is given by

$$n_F = \frac{(2F + 1) \exp(E_F/k_B T)}{\sum_F (2F + 1) \exp(E_F/k_B T)}, \quad (4.9)$$

where $E(F)$ is the energy of the hyperfine ground state level F , and f_{iso} is the natural abundance of a particular isotope. For a given transition $|J, F\rangle \rightarrow |J', F'\rangle$, the absorption cross section is

$$\sigma_{F \rightarrow F'}(\omega, \omega_o) = \frac{\lambda^2}{8\pi} \frac{2J' + 1}{2J + 1} g_D(\omega, \omega_o) \Gamma S_{F \rightarrow F'}, \quad (4.10)$$

where Γ is the excited state decay rate, $S_{F \rightarrow F'}$ is the transition strength and ω_o is the resonance frequency of the transition $F \rightarrow F'$. The Maxwell-Boltzmann distribution g_D is

$$g_D(\omega, \omega_o) = \sqrt{\frac{m_{\text{iso}}}{2\pi k_B T}} \frac{c}{\omega_o} \exp\left(-\left(c \frac{\omega - \omega_o}{\omega_o}\right)^2 \frac{m_{\text{iso}}}{k_B T}\right), \quad (4.11)$$

where m_{iso} is the mass of the isotope, k_B is Boltzmann's constant, T is the temperature, c is the speed of light. Plotted in Fig. 4.18 is the absorption cross-section for ^{87}Rb $F = 2$ and the ^{85}Rb $F = 3$ transitions at $T = 315$ K [42°C]. For the ^{85}Rb peak, $\sigma_2 = 9.5 \times 10^{-15}$, and for ^{87}Rb , $\sigma_2 = 5 \times 10^{-15}$. We estimate the light path to be $l = 1.5$ mm, and from the graph in Fig. 4.17, $A_2 = -47$, $A_1 = -17$, giving us a total atomic number density of $n = 1.5 \times 10^{17}$ molecules \cdot m $^{-3}$. Since the fractional abundance of ^{87}Rb is 27%, the number of moles per unit volume of ^{87}Rb contained in the cell is about $n_{\text{mol}} = 6.7 \times 10^{-7}$ mol \cdot m $^{-3}$. From this result, we can use the ideal gas law $P = n_{\text{mol}}RT$ to find the vapor pressure P in the cell, where R is the ideal gas constant. We estimate the vapor pressure to be $P = 1.3 \times 10^{-6}$ Torr. Comparing this value to the one obtained from the vapor-pressure model given in [17], which is meant only to serve as a rough guide, at 42°C, we expect a vapor pressure of ^{87}Rb to be about 2×10^{-6} Torr. Therefore, the calculated values are reasonable. We note, however, that the temperature inside the chamber may be higher than the silicon back surface where we placed the thermocoupler, so our pressure calculation may be an underestimate. The hot air was directed from the glass front surface of the cell and so does not directly heat back surface; the heat would have to flow through the

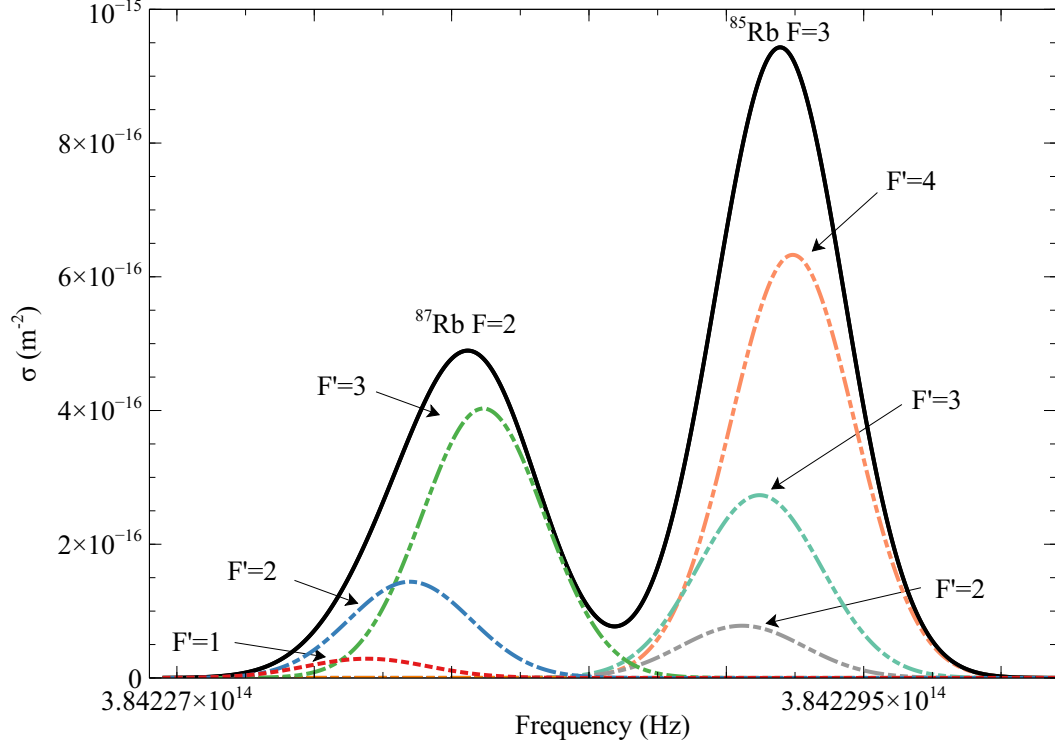


Figure 4.18: Absorption cross-section for the $^{87}\text{Rb } F = 2$ and the $^{85}\text{Rb } F = 3$ transitions at $T = 315$ K. Dotted colored lines show the individual absorption cross sections for a given transition $|J, F\rangle \rightarrow |J', F'\rangle$ [4.9], and the solid black line show the total absorption cross section [Eq. 4.8]. Only two peaks are shown because these transitions will be used to estimate the number density n .

chamber to warm up the silicon wafer. A better method to measure temperature inside the cell may be to use infrared cameras.

As a side note, if we wanted to resolve the hyperfine levels in the excited state, we can do so using saturated absorption spectroscopy, also known as Doppler-free spectroscopy, where two beams, a pump, and a probe, propagating in different directions, are used to address atoms in the velocity class $v = 0$. These atoms see both beams as being on resonance.

4.6 Future Directions

4.6.1 Optimizing Rb Vapor Release

Further investigation could be done on activating the dispenser without causing cracks. This could be done by adjusting the laser heating parameters, such as slowly increasing the laser power or by heating it at a slightly lower laser power for longer times.

4.6.2 Through-Hole Cells

We have since purchased 1 mm thick double-sided polished Si wafers. We plan to fabricate vapor cells with through-holes, which would allow more flexibility in the optical setup as we do not have to adjust the angle when reflecting off the back panel of the wafer. Through-hole chambers can be done by deep reactive ion etching [DRIE], which creates vertical sidewalls. SiN cannot be used as a mask as it etches easily in the SF₆-based etch chemistry used in DRIE. The selectivity of Si to photoresist and SiO₂ is 100:1 and 300:1, respectively. Typically, the SiO₂ is first etched via RIE [as was done for LPCVD SiN in step 6 in Fig. 4.5] to create the mask pattern. To provide more masking, the photoresist is kept for the subsequent deep-reactive ion etching of the Si wafer, instead of removed as in step 7. DRIE etching would also be beneficial to create micron-sized features that are needed for channels between the interrogation and the dispenser chamber. Our approach using KOH etching caused over-etching and widened channels.

4.6.3 Extending Polarization Lifetimes

Miniaturized quantum-based sensing devices have a lower sensitivity due to increased collisions of the atoms with the walls, leading to reduced atomic polarization lifetimes. An approach to remedy this issue is to introduce buffer gases. Another method is to use anti-relaxation wall-coatings.

Buffer Gas

Buffer gases such as H_2 , He, Ne, N_2 , Kr, and Ar are used to slow down the diffusion of the atoms in the cell, increasing the time taken to collide with the chamber walls, which reduces decoherence. However, the interaction between buffer gases and rubidium atoms causes a shift in the hyperfine frequency [50]. The shift depends on the temperature and the buffer gas density. For lighter atoms such as H_2 , He, Ne, and N_2 , the shift is positive, while for heavier atoms such as Kr and Ar, the shift is negative. The hyperfine frequency shift can be used to estimate the partial pressure of the buffer gas[es] in a cell. Depending on the purpose of the vapor cell, such as for SERF magnetometry, we may wish to include them. Buffer gases can be introduced during the anodic bonding step when the cell is sealed under the partial pressure of the gas instead of under vacuum. The **SUSS Microtech CB6L Substrate Bonder** only allows sealing under vacuum or N_2 gas. Previous studies have shown that Zr in the pill traps the N_2 and is therefore not compatible with the micro-pill method of Rb introduction [51]. However, we could try to bond under a higher partial pressure of N_2 to see if there would be an excess of N_2 not trapped by Zr.

Another way to introduce Rb vapor and a buffer gas into the cell is to use rubidium azide RbN_3 , which decomposes into Rb vapor and N_2 gas under several days of UV light exposure [52]. However, this method restricts the ratio of buffer gas to Rb atoms.

Anti-Relaxation Coatings

Compared to buffer gases, anti-relaxation coatings are advantageous because they require less laser power to get an optical signal [53]. There are three main groups of coatings with good anti-relaxation properties for alkali metals: alkenes, alkanes, and organosilanes. Alkenes are the most efficient, allowing more than 10^6 wall collisions before depolarization, but their melting temperature is around 30°C . Most working temperatures of vapor cells are above 50°C , as in our case with the microwave cavity setup. Alkanes have higher melting temperatures of $70 - 90^\circ\text{C}$ but allow fewer wall

collisions, 10^4 before depolarization. Organosilanes have the highest working temperatures. They degrade irreversibly at temperatures above 170°C in the presence of Rb but allow only up to 2000 wall collisions. The melting temperatures of anti-relaxation coatings are all lower than the elevated temperature required for anodic bonding. A low-temperature thin-film indium thermo-compression bonding technique was introduced in [54] and used in [55] to microfabricate a rubidium vapor cell coated with octadecyl trichlorosilane, an organosilane. This method avoids anodically bonding glass to the wafer in the presence of the coating, by first bonding the glass to the Si wafer, applying the coating, and then sealing from Si sides of the two stacks together at 140°C with the help of an indium ring.

4.6.4 Cell Lifetime

Rubidium metal consumption, attributed to the reaction of rubidium with contaminants on the cell surface or in the chamber and the reduction of silicon oxide/dioxide in the glass by rubidium, is a failure mode of alkali vapor cells [51]. When used as part of a commercial device, the alkali vapor present needs to be maintained over the device's lifetime. The initial amount of atoms present has to compensate for any consumption that may occur. Oxidic materials have been used as passivation layers against alkali vapor [52, 56]. To be suitable as a passivation layer, the Gibbs free energy [a measure of the spontaneity of the creation of the compound] of the oxide must be greater than the Gibbs free energy of the alkali metal oxide. It was reported in [56] that a 20 nm aluminum oxide [Al_2O_3] coating did not affect transmittance of the cell and improved the lifetime of a cesium cell by a factor of approximately 100, because of the extremely slow reduction of Al_2O_3 by Cs. Al_2O_3 can be deposited onto the glass wafers before anodic bonding by atomic layer deposition [ALD] or by molecular vapor deposition [MVD]. The latter improves the density, smoothness, and stability of the film, compared to standard liquid or vapor-deposited coatings [51].

Chapter 5

Conclusion and Future Prospects

In the first part of this thesis, we suggested a technique for vector magnetometry using microwave-assisted optical pumping [32]. In microwave-assisted optical pumping, a microwave field resonant to the ground state hyperfine transition of ^{87}Rb redistributes atoms in the $F = 1$ sublevels, which are split in the presence of a static magnetic field, while an optical field resonant with the $F = 1 \rightarrow F' = 0$ transition probed the population of the atoms in the ground state. This method allows us to resolve each of the nine transitions magnetic dipole transitions occurring at seven different microwave frequencies. We measured the Larmor precession frequency by measuring the frequency difference between neighboring DR peaks, providing a method for scalar magnetometry. To do vector magnetometry - where we find the direction of the field in space - we can look at the amplitude ratio between σ_{\pm} and π transitions. The amplitudes depend on the parallel and perpendicular components of the microwave field with respect to the direction of the static magnetic field and excite π and σ_{\pm} transitions, respectively.

We did not acquire consistent data because of various problems, including fluctuating atomic densities due to leakage in the vacuum system, laser power instability, vibrations, and other unknown reasons. We have since replaced our setup with a sealed vapor cell enhanced with ^{87}Rb . However, the double-resonance signal from the new cell was weak, because the cavity quality factor was low. Further investigation is

needed to understand why the cavity appears to be incompatible with the new cell.

The microwave-assisted optical pumping method provides a rapid method for measuring DC magnetic field strengths because we can directly look at the frequency separation between peaks in the double-resonance spectrum to extract the Larmor frequency, without having to run a pump-probe sequence to measure the change in anisotropy of the system [as described in Section 3.1.1]. This setup does not rival other magnetometry techniques in terms of sensitivity and precision, and so would not be suitable for bio-magnetism or for geographical surveying. However, it would be worth re-taking the measurements in a zero-field environment with consistent atom number density and stable signals to gain a better idea of the limitations. It can provide a quick, in-situ measurement of the ambient magnetic field in microwave-cavity atomic physics setups.

The second part of the thesis presents the microfabrication process Rb vapor cells with a blind-hole design. We coated the silicon wafer with a 100 nm layer of aluminum to create a mirror finish with 87% reflectance. We etched the wafers in KOH to create angled sidewalls, hoping to utilize them to increase the optical path length. However, the sidewalls as is were difficult to work with. Instead, we reflected light off the back panel of the wafer. Rubidium atoms were introduced into the cell by heating a micro-dispenser pill containing a mixture of rubidium chromate, zirconium, and aluminum. The first step of this project was to test for the presence of rubidium atoms, which was successful. We were able to see Doppler-broadened peaks of the D1 transitions of both isotopes of rubidium. More research is needed to find optimal heating parameters for activating the dispenser. Furthermore, we need to design through-hole cells having the dispenser and the interrogation chambers connected by narrow filtration channels. These filtration channels should be sufficiently narrow, in the 10s of μm in width to prevent impurities from entering the interrogation chamber. We could also consider making several cells with the same dimensions and test for consistency in atomic density. Consistency between cells is important when manufacturing quantum sensing

devices. For example, in magnetic field gradiometers where we measure the difference signal between two identical magnetometers, one placed at the source of the magnetic field of interest and the other further away, cell consistency is necessary, because we want the response function of the two magnetometers to be the same.

Chip-scale cells are important for portable quantum technologies. Traditional atomic physics experiments reside on a large optical bench that can take up more than two meters of space, making the technology nearly impossible to move out to real-world environments. However, there is much progress in microwave atom tools. Microwave technologies are important in telecommunications and have potential in microwave medical imaging [3, 13]. Atom-microwave couplings experiments have been realized in microwave-to-optical transduction [5], and Rydberg-based receivers [4], to name a few. Immediate future directions could focus on marrying chip-scale vapor cells and microwave fields sources. While there are difficulties when the dimension of the interaction region is smaller than the wavelength of the microwave field, miniature microwave cavities or micro-strip line circuits have been designed and shown to work in atomic clocks. In addition, RF pulses are also important in the cooling process of ultracold atoms, and these have applications in quantum memories and quantum repeaters. With an appropriate vapor cell design, microwave circuit, and integrated optics to enhance laser-atom and microwave-atom interactions, we may be able to create on-chip laser-cooled atoms, and design portable ultracold atom chips for photonic quantum memory applications [0].

As explained above, there are many avenues we could explore once we have a good working prototype. The convenience of silicon micro-machining tools and techniques makes it easy to modify our process flow to suit our application needs.

Bibliography

- [1] C. L. Degen, F Reinhard, and P. Cappellaro, “Quantum sensing,” *Reviews of Modern Physics*, vol. 89, no. 3, p. 035 002, 2017.
- [2] A. Hinton, M Perea-Ortiz, J Winch, J Briggs, S Freer, D Moustoukas, S Powell-Gill, C Squire, A Lamb, C Rammeloo, *et al.*, “A portable magneto-optical trap with prospects for atom interferometry in civil engineering,” *Philosophical Transactions of the Royal Society A: Mathematical, Physical and Engineering Sciences*, vol. 375, no. 2099, p. 20 160 238, 2017.
- [3] N. K. Nikolova, “Microwave imaging for breast cancer,” *IEEE Microwave Magazine*, vol. 12, no. 7, pp. 78–94, 2011.
- [4] D. H. Meyer, P. D. Kunz, and K. C. Cox, “Waveguide-coupled rydberg spectrum analyzer from 0 to 20 Ghz,” *Physical Review Applied*, vol. 15, no. 1, p. 014 053, 2021.
- [5] A Tretiakov, C. Potts, T. Lee, M. Thiessen, J. Davis, and L. LeBlanc, “Atomic microwave-to-optical signal transduction via magnetic-field coupling in a resonant microwave cavity,” *Applied Physics Letters*, vol. 116, no. 16, p. 164 101, 2020.
- [6] J. C. Camparo, “The rubidium atomic clock and basic research,” Aerospace Corp El Segundo CA Physical Sciences Labs, Tech. Rep., 2007.
- [7] *Optical frequency combs*, [Online] Available: <https://www.nist.gov/topics/physics/optical-frequency-combs>. [Accessed July 24, 2021], NIST.
- [8] J. Kitching, “Chip-scale atomic devices,” *Applied Physics Reviews*, vol. 5, no. 3, p. 031 302, 2018.
- [9] M Violetti, C Afforderbach, F Merli, G Mileti, and A. Skrivervik, “Microwave resonator, quantum sensor, and atomic clock,” *European Patent Application No*, vol. 12155696, 2012.
- [10] A. Braun, T. Davis, M. Kwakernaak, J. Michalchuk, A Ulmer, W. Chan, J. Abeles, Z. Shellenbarger, Y. Jau, W Happer, *et al.*, “Rf-interrogated end-state chip-scale atomic clock,” in *Proceedings of the 39th Annual Precise Time and Time Interval Meeting*, 2007, pp. 233–248.

- [11] E. Boto, N. Holmes, J. Leggett, G. Roberts, V. Shah, S. S. Meyer, L. D. Muñoz, K. J. Mullinger, T. M. Tierney, S. Bestmann, *et al.*, “Moving magnetoencephalography towards real-world applications with a wearable system,” *Nature*, vol. 555, no. 7698, pp. 657–661, 2018.
- [12] E. C. Fear, S. C. Hagness, P. M. Meaney, M. Okoniewski, and M. A. Stuchly, “Enhancing breast tumor detection with near-field imaging,” *IEEE Microwave magazine*, vol. 3, no. 1, pp. 48–56, 2002.
- [13] A. Horsley and P. Treutlein, “Frequency-tunable microwave field detection in an atomic vapor cell,” *Applied Physics Letters*, vol. 108, no. 21, p. 211102, 2016.
- [14] M. Auzinsh, D. Budker, and S. Rochester, “Optically polarized atoms: Understanding light-atom interactions,” in. Oxford University Press, 2010.
- [15] C. Cohen-Tannoudji, B. Diu, and F. Laloë, “Quantum mechanics volume ii: Angular momentum, spin, and approximation methods,” in. Weinheim: Wiley VCH Verlag GmbH & Co., 2020, vol. 2.
- [16] C. J. Foot *et al.*, “Atomic physics,” in. Oxford University Press, 2005, vol. 7.
- [17] D. A. Steck, *Rubidium 87 d line data*, 2001.
- [18] I. D. Leroux, *Manipulation of ultra-cold atoms using radio-frequency and microwave radiation*, B.Sc. Thesis, Apr. 2005.
- [19] P. W. Milonni, “An introduction to quantum optics and quantum fluctuations,” in. Oxford University Press, 2019.
- [20] D. Suter, “The physics of laser-atom interactions,” in. Cambridge University Press, 1997.
- [21] F. Kärtner, *Chapter 6 interaction of light and matter*, Lecture Notes, 2006.
- [22] S. Rochester, *AtomicDensityMatrix*, [Mathematica Package, Online] Available: <http://rochesterscientific.com/ADM> [Accessed June 1, 2021], v20.04.27.
- [23] S. J. Seltzer, “Developments in alkali-metal atomic magnetometry,” PhD thesis, Princeton University, 2008.
- [24] R. Li, F. N. Baynes, A. N. Luiten, and C. Perrella, “Continuous high-sensitivity and high-bandwidth atomic magnetometer,” *Physical Review Applied*, vol. 14, no. 6, p. 064067, 2020.
- [25] W. Gawlik and S. Pustelny, “Nonlinear Faraday effect and its applications,” *Horizons in World Physics: New Trends in Quantum Coherence and Nonlinear Optics*, vol. 263, pp. 45–82, 2009.
- [26] A. Kastler, “The Hanle effect and its use for the measurements of very small magnetic fields,” *Nuclear instruments and methods*, vol. 110, pp. 259–265, 1973.
- [27] C. Cohen-Tannoudji, J. Dupont-Roc, S. Haroche, and F. Laloë, “Diverses résonances de croisement de niveaux sur des atomes pompés optiquement en champ nul. i. théorie,” *Revue de Physique Appliquée*, vol. 5, no. 1, pp. 95–101, 1970.

- [28] I. Sulai, Z. DeLand, M. Bulatowicz, C. Wahl, R. Wakai, and T. Walker, “Characterizing atomic magnetic gradiometers for fetal magnetocardiography,” *Review of Scientific Instruments*, vol. 90, no. 8, p. 085 003, 2019.
- [29] C. N. Johnson, P. Schwindt, and M. Weisend, “Multi-sensor magnetoencephalography with atomic magnetometers,” *Physics in Medicine & Biology*, vol. 58, no. 17, p. 6065, 2013.
- [30] J. Li, W. Quan, B. Zhou, Z. Wang, J. Lu, Z. Hu, G. Liu, and J. Fang, “SERF atomic magnetometer—recent advances and applications: A review,” *IEEE Sensors Journal*, vol. 18, no. 20, pp. 8198–8207, 2018.
- [31] T. Sander, J. Preusser, R. Mhaskar, J. Kitching, L. Trahms, and S. Knappe, “Magnetoencephalography with a chip-scale atomic magnetometer,” *Biomedical Optics Express*, vol. 3, no. 5, pp. 981–990, 2012.
- [32] A. Tretiakov, “Manipulating optical properties of 87rb vapors with microwave magnetic fields,” PhD thesis, University of Alberta, 2021.
- [33] M. J. Reagor, “Superconducting cavities for circuit quantum electrodynamics,” PhD thesis, Yale University, 2015.
- [34] D. M. Pozar, “Microwave engineering,” in. John Wiley & Sons, 2011.
- [35] W. Demtröder, “Laser spectroscopy: Basic concepts and instrumentation,” in. Springer Science & Business Media, 2013.
- [36] J. Vanier and C. Audoin, “The quantum physics of atomic frequency standards,” in. CRC Press, 1989.
- [37] J. Vanier and C. Tamescu, “The quantum physics of atomic frequency standards: Recent developments,” in. CRC Press, 2015.
- [38] *Safety data sheet rb/amax*, BSDS111621/2, Ver. 2, SAES Group, 2018.
- [39] L. Nieradko, C. Gorecki, A. Douahi, V. Giordano, J.-C. Beugnot, J. A. Dziuban, and M. Moraja, “New approach of fabrication and dispensing of micromachined cesium vapor cell,” *Journal of Micro/Nanolithography, MEMS, and MOEMS*, vol. 7, no. 3, p. 033 013, 2008.
- [40] *Silicon wafer production and specifications*, Application notes. [Online] Available: https://www.microchemicals.com/technical_information/silicon_wafer_production_specification.pdf [Accessed February 20, 2021], MicroChemicals.
- [41] A. Hyrciw, *Raith_gdsii matlab toolbox user guide*, The Raith_GDSII MATLAB toolbox was developed at the National Institute for Nanotechnology and is maintained at the University of Alberta nanoFAB Centre. [Online] Available: https://www.github.com/nrc-cnrc/Raith_GDSII, University of Alberta.
- [42] M. J. Madou, “Fundamentals of microfabrication and nanotechnology, three-volume set,” in. CRC Press, 2018.
- [43] J. Daggett, S. Villareal, and R. Robbins, *HMDS process*, [Online] Available: <https://research.utdallas.edu/cleanroom/manuals/hmds-process> [Accessed January 6, 2021], February 21, 2003.

- [44] *Maskless lithography: Direct writing on the microscale*, [Online] Available: <https://heidelberg-instruments.com/en/features-technologies/key-features/maskless-lithography.html>. [Accessed January 6, 2021], Heidelberg Instruments.
- [45] A. D. Rakić, A. B. Djurišić, J. M. Elazar, and M. L. Majewski, “Optical properties of metallic films for vertical-cavity optoelectronic devices,” *Applied optics*, vol. 37, no. 22, pp. 5271–5283, 1998.
- [46] R. Chutani, “Design, technology and packaging of cesium vapor cells for mems atomic clocks,” PhD thesis, Université de Franche-Comté, Engineering Sciences [physics], 2011.
- [47] R. Han, Z. You, F. Zhang, H. Xue, and Y. Ruan, “Microfabricated vapor cells with reflective sidewalls for chip scale atomic sensors,” *Micromachines*, vol. 9, no. 4, p. 175, 2018.
- [48] M. A. Sullivan, “A cold atoms apparatus for a new hybrid quantum system,” Master’s thesis, University of Alberta, Department of Physics, 2020.
- [49] A. Tretiakov, “Microwave-to-optical conversion in 87Rb,” University of Alberta, Tech. Rep., 2021.
- [50] J Vanier, R Kunski, N Cyr, J. Savard, and M Têtu, “On hyperfine frequency shifts caused by buffer gases: Application to the optically pumped passive rubidium frequency standard,” *Journal of Applied Physics*, vol. 53, no. 8, pp. 5387–5391, 1982.
- [51] S. Karlen, “Fabrication and characterization of MEMS alkali vapor cells used in chip-scale atomic clocks and other atomic devices,” PhD thesis, Université de Neuchâtel, La Faculté des sciences, 2017.
- [52] S. Karlen, J. Gobet, T. Overstolz, J. Haesler, and S. Lecomte, “Lifetime assessment of RbN 3-filled MEMS atomic vapor cells with Al₂O₃ coating,” *Optics express*, vol. 25, no. 3, pp. 2187–2194, 2017.
- [53] Y. Ji, J. Shang, Q. Gan, and L. Wu, “Wafer-level micro alkali vapor cells with anti-relaxation coating compatible with mems packaging for chip-scale atomic magnetometers,” in *2017 IEEE 67th Electronic Components and Technology Conference (ECTC)*, IEEE, 2017, pp. 2116–2120.
- [54] R. Straessle, M Pellaton, C. Affolderbach, Y. Pétremand, D. Briand, G. Mileti, and N. F. de Rooij, “Low-temperature indium-bonded alkali vapor cell for chip-scale atomic clocks,” *Journal of Applied Physics*, vol. 113, no. 6, p. 064501, 2013.
- [55] R. Straessle, M. Pellaton, C. Affolderbach, Y. Pétremand, D. Briand, G. Mileti, and N. F. de Rooij, “Microfabricated alkali vapor cell with anti-relaxation wall coating,” *Applied Physics Letters*, vol. 105, no. 4, p. 043502, 2014.
- [56] S Woetzel, F Talkenberg, T Scholtes, R Ijsselsteijn, V Schultze, and H.-G. Meyer, “Lifetime improvement of micro-fabricated alkali vapor cells by atomic layer deposited wall coatings,” *Surface and Coatings Technology*, vol. 221, pp. 158–162, 2013.

- [0] E. Saglamyurek, T. Hrushevskyi, A. Rastogi, K. Heshami, and L. J. LeBlanc, “Coherent storage and manipulation of broadband photons via dynamically controlled autler–townes splitting,” *Nature Photonics*, vol. 12, no. 12, pp. 774–782, 2018.
- [57] R. W. Boyd, “Nonlinear optics,” in. Academic press, 2020.

Appendix A: Matrix Representation of State Vectors and Operators

A.1 Bra and Ket Vectors

An arbitrary state vector $|\Psi\rangle$ can be expressed as a linear combination of basis states $\{|\psi_n\rangle, n = 1, 2, 3 \dots\}$,

$$|\Psi\rangle = \sum_n |\psi_n\rangle \langle\psi_n|\Psi\rangle = \sum_n c_n |\psi_n\rangle, \quad (\text{A.1})$$

where $\langle\psi_n|\Psi\rangle = c_n$ are scalars, not all zeros, that give the weights of the linear combination. In vector notation, the ket $|\Psi\rangle$ is a column vector with respect to the set of basis states $\{|\psi_n\rangle, n = 1, 2, 3 \dots\}$,

$$|\Psi\rangle = \begin{pmatrix} c_1 \\ c_2 \\ c_3 \\ \vdots \end{pmatrix}, \quad (\text{A.2})$$

while the bra $\langle\Psi|$ is a row vector, with elements that are complex conjugates of the elements of $|\Psi\rangle$

$$\langle\Psi| = (c_1^* \quad c_2^* \quad c_3^* \dots). \quad (\text{A.3})$$

The basis states $\{|\psi_n\rangle, n = 1, 2, 3 \dots\}$ are orthogonal, satisfying

$$\langle\psi_m|\psi_n\rangle = \delta_{mn}, \quad (\text{A.4})$$

where δ_{mn} is the Delta-Dirac function. It follows that the basis states are column vectors of the form

$$|\psi_1\rangle = \begin{pmatrix} 1 \\ 0 \\ 0 \\ \vdots \end{pmatrix} \quad |\psi_2\rangle = \begin{pmatrix} 0 \\ 1 \\ 0 \\ \vdots \end{pmatrix} \quad |\psi_3\rangle = \begin{pmatrix} 0 \\ 0 \\ 1 \\ \vdots \end{pmatrix}. \quad (\text{A.5})$$

An inner product $\langle\chi|\Psi\rangle$ in terms of the basis states is defined as

$$\langle\chi|\Psi\rangle = \sum_n \langle\psi_n|\langle\chi|\psi_n\rangle|\psi_n\rangle\langle\psi_n|\Psi\rangle = \sum_n \langle\chi|\psi_n\rangle\langle\Psi|\psi_n\rangle. \quad (\text{A.6})$$

Defining $\langle\chi|\psi_n\rangle = b_n^*$, the inner product can be expressed as

$$\langle\chi|\Psi\rangle = \begin{pmatrix} b_1^* & b_2^* & b_3^* & \dots \end{pmatrix} \begin{pmatrix} c_1 \\ c_2 \\ c_3 \\ \vdots \end{pmatrix} = \sum_n b_n^* c_n. \quad (\text{A.7})$$

A.2 Operator Matrices

The operator equation

$$\hat{H}|\Psi\rangle = |\Phi\rangle \quad (\text{A.8})$$

can be expanded out as

$$|\Phi\rangle = \sum_n \hat{H}|\psi_n\rangle\langle\psi_n|\Psi\rangle. \quad (\text{A.9})$$

To find the element of the operators in terms of the basis states $\{|\psi_n\rangle, n = 1, 2, 3 \dots\}$, we take the inner product

$$\langle\psi_m|\Phi\rangle = \sum_n \langle\psi_m|\hat{H}|\psi_n\rangle\langle\psi_n|\Psi\rangle, \quad (\text{A.10})$$

which can be written as

$$a_m = \sum_n \langle\psi_m|\hat{H}|\psi_n\rangle c_n, \quad (\text{A.11})$$

where

$$a_m = \langle \psi_m | \Phi \rangle \quad (\text{A.12})$$

In matrix notation, the operator equation is

$$\begin{pmatrix} a_1 \\ a_2 \\ \vdots \end{pmatrix} = \begin{pmatrix} H_{11} & H_{12} & \cdots \\ H_{21} & H_{22} & \cdots \\ \vdots & \vdots & \ddots \end{pmatrix} \begin{pmatrix} c_1 \\ c_2 \\ \vdots \end{pmatrix}, \quad (\text{A.13})$$

where the operator \hat{H} is represented by a matrix

$$\hat{H} = \begin{pmatrix} H_{11} & H_{12} & \cdots \\ H_{21} & H_{22} & \cdots \\ \vdots & \vdots & \ddots \end{pmatrix}, \quad (\text{A.14})$$

with its matrix elements defined by

$$H_{mn} = \sum_n \langle \psi_m | \hat{H} | \psi_n \rangle. \quad (\text{A.15})$$

Appendix B: Linear Optics

B.1 Polarization and Susceptibility

The polarization \mathbf{P} , or dipole moment per unit volume of a medium with density n , is given by the product of the average quantum mechanical dipole moment $\langle \boldsymbol{\mu} \rangle$ and the density of the system

$$\mathbf{P} = n \langle \boldsymbol{\mu} \rangle. \quad (\text{B.1})$$

The polarization can also be expressed in terms of the complex susceptibility of the medium, $\chi = \chi' - i\chi''$, and the electromagnetic field, $\mathbf{E}(t) = \mathbf{E}_o \cos \omega t$, that induces the polarization. If the medium is isotropic, the polarization is parallel to the electric field of the incident wave

$$\mathbf{P} = \epsilon_o \chi \mathbf{E}_o \cos \omega t. \quad (\text{B.2})$$

If the medium is anisotropic, the relationship is described by a tensor and not by a scalar as in Eq. B.2, and the medium can exhibit birefringence, which can occur in a multi-level system where the ground states are unequally populated. Real systems are multi-leveled and interactions with external fields break two-level symmetry. However, if the system is weakly perturbed, it is isotropic and can be approximated with two energy levels, which we will work with here. Expanding the polarization in terms of the real and imaginary components of the complex susceptibility gives

$$\mathbf{P} = \epsilon_o \mathbf{E}_o (\chi' \cos \omega t + \chi'' \sin \omega t). \quad (\text{B.3})$$

We relate the susceptibility to the components of the Bloch vector first by re-writing the dipole moment in terms of the Bloch vector components. For a two-level atomic

system, the average dipole moment in the rotating frame is

$$\langle \boldsymbol{\mu} \rangle = \text{Tr} \left\{ \hat{\rho} \hat{\boldsymbol{\mu}} \right\} \quad (\text{B.4})$$

$$= \text{Tr} \left\{ \begin{pmatrix} 0 & \boldsymbol{\mu}_{12} \\ \boldsymbol{\mu}_{21} & 0 \end{pmatrix} \begin{pmatrix} \tilde{\rho}_{11} & \tilde{\rho}_{12} \\ \tilde{\rho}_{21} & \tilde{\rho}_{22} \end{pmatrix} \right\} \quad (\text{B.5})$$

$$= \boldsymbol{\mu}_{12} (\tilde{\rho}_{21} + \tilde{\rho}_{21}^*), \quad (\text{B.6})$$

where $\boldsymbol{\mu}_{12} = e \langle 2 | \hat{\mathbf{r}} | 1 \rangle$ is the dipole moment between states $|1\rangle$ and $|2\rangle$. In going to the last line, we have assumed that the dipole moment is real, i.e. $\boldsymbol{\mu}_{12} = \boldsymbol{\mu}_{21}^*$. Since from the transformation $\hat{\rho} = U^{-1} \hat{\rho} \hat{U}$,

$$\hat{\rho} = \begin{pmatrix} \rho_{11} & \rho_{12} e^{-i\omega t} \\ \rho_{21} e^{i\omega t} & \rho_{22} \end{pmatrix}, \quad (\text{B.7})$$

the average dipole moment in terms of the laboratory frame density matrix element is

$$\langle \boldsymbol{\mu} \rangle = \boldsymbol{\mu}_{12} [\rho_{21} e^{i\omega t} + (\rho_{21} e^{i\omega t})^*] \quad (\text{B.8})$$

$$= \boldsymbol{\mu}_{12} [(\rho_{12} + \rho_{21}) \cos \omega t - i(\rho_{12} - \rho_{21}) \sin \omega t] \quad (\text{B.9})$$

$$= \mu_{12} (R_x \cos \omega t + R_y \sin \omega t), \quad (\text{B.10})$$

where R_x and R_y are the x and y components of the Bloch vector, respectively. Thus

$$\mathbf{P} = n \boldsymbol{\mu}_{12} (R_x \cos \omega t + R_y \sin \omega t). \quad (\text{B.11})$$

A comparison of Eq. B.11 with Eq. B.3 shows that the real part of the complex susceptibility is given by R_x ,

$$\chi' = \frac{n \mu_{12}}{\epsilon_o E_o} R_x = \frac{n \mu_{12}^2}{\epsilon_o \hbar} \frac{\delta}{\frac{\Omega_R^2}{\Gamma_1 \Gamma_2} + \delta^2 + \Gamma_2^2}, \quad (\text{B.12})$$

while the imaginary part of the complex susceptibility is given by R_y ,

$$\chi'' = \frac{n \mu_{12}}{\epsilon_o E_o} R_y = \frac{n \mu_{12}^2}{\epsilon_o \hbar} \frac{\Gamma_2}{\frac{\Omega_R^2}{\Gamma_1 \Gamma_2} + \delta^2 + \Gamma_2^2}. \quad (\text{B.13})$$

B.2 Absorption

A linear medium supports the propagation of an electromagnetic field with complex wave vector $k = n\frac{\omega_l}{c} = k' - ik''$, where c is the speed of light, ω_l is the angular frequency of the field and n is the refractive index,

$$n = \sqrt{1 + \chi} \approx 1 + \frac{1}{2}(\chi' - i\chi''). \quad (\text{B.14})$$

The approximation in Eq. B.14 is valid when χ is less than unity, which occurs when the energy losses or the phase shifts by the medium on wavelengths distances are small, as in the case for a dilute gas. In this approximation, from the definition of k , the imaginary and real parts of the wave vector are given by

$$k'' = \frac{1}{2} \frac{\omega_l}{c} \chi'' \quad (\text{B.15a})$$

$$k' = 1 + \frac{1}{2} \frac{\omega_l}{c} \chi'. \quad (\text{B.15b})$$

A wave propagating along $+z$ in the linear medium can thus be written as

$$\mathbf{E}(z, t) = \text{Re}\{\mathbf{E}_o e^{i(kz - \omega t)}\} \quad (\text{B.16})$$

$$= e^{-k''z} \text{Re}\{\mathbf{E}_o e^{i(k'z - \omega t)}\}, \quad (\text{B.17})$$

which shows that the amplitude of the field decreases exponentially along the direction of the propagation when $k'' \neq 0$. We can see from Eq. B.16 that the imaginary part of the susceptibility is attributed to absorption, while the real part is related to the propagation of the wave. Since intensity is proportional to the square of the electric field, the change in intensity of a field propagating a distance z through an absorptive medium is given by the Beer-Lambert law,

$$I(z) = I(0)e^{-\kappa(\omega_l)z}, \quad (\text{B.18})$$

which can be measured experimentally. Here, $\kappa(\omega_l) = 2k''\omega_l/c$ is the absorption coefficient. Alternatively, in terms of the susceptibility,

$$\kappa(\omega_l) = \frac{\omega_l}{c} \chi''. \quad (\text{B.19})$$

B.2.1 Absorption Cross Section

It is common to define the absorption coefficient in terms of the absorption [or scattering] cross section,

$$\kappa(\omega) = N\sigma(\omega). \quad (\text{B.20})$$

In the weak intensity limit, the absorption cross section is equal to

$$\sigma(\omega) = \frac{\omega}{c} \frac{d_{ab}^2}{3\hbar\epsilon_o} \frac{\Gamma_2}{\delta^2 + \Gamma_2^2}. \quad (\text{B.21})$$

We can interpret the absorption cross section as the effective area of absorption of an atom. The value of the absorption cross section is maximized on resonance and when Γ_2 is minimized, which occurs when spontaneous emission is the only source of dephasing. From Eq. 2.72, this rate is equal to

$$\Gamma_2 = \frac{1}{2}\Gamma_1 = \frac{d_{ab}^2}{6\pi\epsilon_o\hbar} \frac{\omega^3}{c^3}. \quad (\text{B.22})$$

Substituting this into Eq. 2.79 and solving for $\sigma_o = \sigma(\omega = \omega_o)$ gives an expression for the resonant absorption cross section

$$\sigma_o = \frac{\omega}{3c} \frac{d_{ab}^2}{\hbar\epsilon_o} \frac{1}{\Gamma_2} = \frac{3\lambda^2}{2\pi}, \quad (\text{B.23})$$

where λ is the wave length of the transition. In arriving at this result, it was assumed that the ground state has angular momentum $J = 1$ [57]. More generally, for a system in thermal equilibrium with equal populations in the ground state, the resonant absorption cross section is [57]

$$\sigma_o = \frac{2J_b + 1}{2J_a + 1} \frac{\lambda}{2\pi}, \quad (\text{B.24})$$

where J_a and J_b are the total angular momentum for the lower and upper levels respectively. If the ground state population is unequally distributed, due to optical pumping effects for example, the expression for σ_o needs to be multiplied by a factor between 0 and 3. From Eq. B.20, the absorption coefficient may be rewritten as

$$\kappa(\omega) = \frac{N}{V} \sigma_o \left(\frac{\Gamma_2^2}{\delta^2 + \Gamma_2^2} \right). \quad (\text{B.25})$$

If buffer gases are present in an alkali vapour cell, then the absorption cross section would depend on the buffer gas pressure and temperature.

Appendix C: Broadening Mechanisms

C.0.1 Collision Broadening

Collision broadening is another type of lifetime broadening, with the lifetime of a state set by collision time interval. In atomic gases, atoms constantly collide with each other and with the wall. If the collision is inelastic, then there will be a change in states. This process also gives a Lorentzian line profile in the absorption spectrum. The effect of collision broadening adds a factor of γ_{col} to the decay rate Γ , so that

$$\Delta\omega \sim \frac{1}{\Delta t} = \Gamma + \gamma_{\text{col}}. \quad (\text{C.1})$$

Collision broadening depends on the atomic species present in the gas, pressure, and temperature. In general, the collision broadening effect is much greater than the natural linewidth effect. Decoherence due to collision broadening can be reduced by introducing buffer gases in an atomic vapor, or by applying anti-relaxation coatings on the vapor cell walls.

C.0.2 Doppler Broadening

Due to thermal motion, the atoms in a gas have a distribution of velocities, leading to the Doppler effect on the absorption of radiation [16], where only radiation resonant with the atoms are absorbed. To illustrate, consider an atom moving at velocity \mathbf{v} in the laboratory frame, in the presence of a laser beam with wave vector \mathbf{k} and frequency $f_L = c|\mathbf{k}|$. Due to the Doppler effect, in the frame moving at velocity \mathbf{v} ,

the frequency of the radiation seen by the atom is

$$f' = f_L - \mathbf{k} \cdot \mathbf{v}. \quad (\text{C.2})$$

If the atom is moving in the same direction as the electromagnetic field, then $\mathbf{k} \cdot \mathbf{v} > 0$ and the perceived frequency is less than the frequency in the lab frame and is said to be red-shifted. If however, the atom is moving in the opposite direction as the field, $\mathbf{k} \cdot \mathbf{v} < 0$ and the perceived frequency is greater than the frequency in the lab frame and is said to be blue-shifted. Absorption occurs only when the laser radiation frequency perceived by the atom, f' , is equal to an atomic transition frequency f_o [the resonance frequency when the atom is at rest with respect to the moving radiation], i.e. $f' = f_o$. This occurs only for the class of atoms with a velocity \mathbf{v} satisfying

$$f_L - f_o = \mathbf{k} \cdot \mathbf{v}. \quad (\text{C.3})$$

Maxwell's velocity distribution gives the fraction of atoms at temperature T with velocities between v and $v + dv$. This distribution has a Gaussian profile, and consequently, so does the absorption spectrum. The absorption probability of radiation with frequencies between f_L and $f_L + df_L$ is

$$g_D(f_L)df_L = \frac{c}{u\sqrt{\pi}} \frac{1}{f_o} \exp \left[-\frac{c^2}{u^2} \left(\frac{f_L - f_o}{f_o} \right)^2 \right] df_L, \quad (\text{C.4})$$

where the most probable speed for atoms of mass M at temperature T is $u = \sqrt{2k_B T/M}$. This Gaussian curve has full-width at half maximum of

$$\Delta f_{\text{dop}} = 2\sqrt{\ln 2} \frac{u}{c} f_o. \quad (\text{C.5})$$

For ^{87}Rb , which has an atomic mass of 86.91 amu [= $1.4415138 \times 10^{-25}$ kg], the Doppler width at 300 K for the D2 transition [780 nm] is $\Delta f_{\text{dop}} = 513$ MHz, which is much larger than the natural line width. Since the frequency spacing between the $^5P_{3/2}$ hyperfine energy levels are less than the Doppler width, these levels cannot be individually resolved. To see these transitions, the Doppler width needs to be

subtracted, which can be done using saturation absorption spectroscopy [16], where a second laser beam is used and atoms with velocity class $\mathbf{v} = 0$ are excited.

Doppler broadening is a type of inhomogeneous broadening mechanism where only certain classes of atoms are affected. For a low-pressure gas at high temperatures, Doppler broadening is the main source of line broadening of spectral lines. In contrast, broadening effects due to excited state lifetime and collision intervals homogeneous broadening because they affect all the atoms in the same manner. Many situations require us to consider all these broadening mechanisms, which combine to give the Voigt profile.